

P
2 mit

INVESTIGATION OF SCALING CHARACTERISTICS
FOR DEFINING DESIGN ENVIRONMENTS DUE TO TRANSIENT GROUND
WINDS AND NEAR-FIELD, NON-LINEAR ACOUSTIC FIELDS

NASA-CR-120101) INVESTIGATION OF SCALING
CHARACTERISTICS FOR DEFINING DESIGN
ENVIRONMENTS DUE TO TRANSIENT GROUND
WINDS AND NEAR-FIELD, (Alabama Univ.,
Huntsville.) 135 p HC \$8.75 CSCL 20D G3/12 15857
N74-12040
Unclas

186

Final Technical Report

This research work was supported by
the National Aeronautics and Space Administration
George C. Marshall Space Flight Center
Contract NAS8-28249

The University of Alabama in Huntsville
Division of Graduate Programs and Research

P. O. Box 1247
Huntsville, Alabama 35807

September 1973

**INVESTIGATION OF SCALING CHARACTERISTICS
FOR DEFINING DESIGN ENVIRONMENTS DUE TO TRANSIENT GROUND
WINDS AND NEAR-FIELD, NON-LINEAR ACOUSTIC FIELDS**

Final Technical Report

**This research work was supported by
the National Aeronautics and Space Administration
George C. Marshall Space Flight Center
Contract NAS8-28249**

**The University of Alabama in Huntsville
Division of Graduate Programs and Research**

**P. O. Box 1247
Huntsville, Alabama 35807**

September 1973

PREFACE

This final report presents results of the research effort supported by the Contract NAS8-28249 for the period from June 1, 1972 through August 31, 1973 consisting of three sections listed as follows:

- SECTION IA Non-Linear Pressure Wave Propagation in Pipes
- SECTION IB Attenuation Characteristics of Non-Linear Pressure Waves Propagating in Pipes
- SECTION II Experimental Investigation of the Unsteady Forces Imposed on a Submerged Circular Cylinder in Accelerating Flow

Under the Principal Investigator's technical direction, the effort involved in Sections IA and B were contributed mainly by C. C. Shih; Section II by David Morrow. To make the success of this study possible, valuable assistance was provided by the following staff members of the Fluid Dynamics Laboratory at the University of Alabama in Huntsville:

Ronald Scott	Dean Montgomery	Steve Hecht		
Manfred Loh	Ramesh Sanghvi	Ming Shih	Tom McMeans	Barbara Oedamer
David Walker	Cindy Conway	Steve K. Macey	Margaret Cuthill	

The Instrumentation Laboratory and the Machine Shop of the University of Alabama in Huntsville also provided useful assistance to the project. The principal investigator provided general directions to all phases of the research project.

Cornelius C. Shih
Principal Investigator

SECTION IA

NON-LINEAR PRESSURE WAVE PROPAGATION IN PIPES

SECTION IA

NON-LINEAR PRESSURE WAVE PROPAGATION IN PIPES

INTRODUCTION

Highly intense pressure waves in the near sound field are generated by launch vehicles. Characteristics of the propagating acoustical energy in the near sound field are highly nonlinear. The use of standard linear scaling techniques for determining environmental criteria such as overall sound pressures and power spectral densities, has resulted in considerable error. But, to the author's knowledge, there are no adequate scaling procedures available for use in the near sound field.

In order to establish a foundation of scaling laws for the highly nonlinear waves associated with the launch vehicle, the basic knowledge of the relationships among the parameters pertinent to the energy dissipation process associated with the propagation of nonlinear pressure waves in thermoviscous media is definitely required. Review of literature indicates that there are numerous studies in theoretical aspect by Burgers (Ref. 1), Hopf (Ref. 2), Cole (Ref. 3), Lighthill (Ref. 4), Rodin (Ref. 5), etc., on the Burgers' equation which is generally accepted for approximating one-dimensionally the above stated phenomena. However, wave propagation in pipes is a typical flow problem solvable by the Burgers' equation with a particular set of boundary conditions, if a coefficient of energy dissipation is given. There are several studies on the wave propagation in pipes by Blackstock (Ref. 6), Nakamura and Takeuchi (Ref. 7), Kantola (Ref. 8), Strunk (Ref. 9), Sawley and White (Ref. 10), Brown (Ref. 11), D'Souza and Oldenburger (Ref. 12), and Schuder and Binder (Ref. 13). These studies are either the treatment of small-amplitude waves, shock waves, plane waves of finite amplitude, or inviscid fluids. Some of them were verified experimentally, but none of them treats the propagation of nonlinear pressure waves of large amplitude through measuring velocity distributions throughout the pipe, in order to gain better understanding of the energy dissipation mechanism.

Specifically, the problem of interest for the present study is to experimentally investigate the temporal and spacial velocity profiles of fluid flow in a 3-inch open-end pipe of various lengths, produced by the propagation of nonlinear pressure waves for various diaphragm burst pressures of a pressure wave generator. As a result, temporal and spacial characteristics of wave propagation for a parametric set of nonlinear pressure waves in the pipe containing air under atmospheric conditions were determined.

Velocity measurements at five sections along the pipes of up to 210 ft. in length were made with hot-film anemometers for five pressure waves produced by a piston. The piston was driven with diaphragm burst pressures at 20, 40, 60, 80 and 100 psi in the driver chamber of the pressure wave generator. Experimental results are presented in graphical form and compared with theoretical results obtained by the method of characteristics with the isentropic assumption.

The Oretical Consideration

The physics of the phenomena considered in this study may be expressed by simplified equations of momentum, energy, continuity, and state by following limiting assumptions: (1) the flow is one-dimensional; (2) the gas process is isentropic; (3) the fluid is perfect.

$$\text{Momentum:} \quad \frac{\partial V}{\partial t} + V \frac{\partial V}{\partial x} = - \frac{1}{\rho} \frac{\partial P}{\partial x} \quad (1)$$

$$\text{Continuity:} \quad \frac{1}{\rho} \frac{d\rho}{dt} + \frac{\partial V}{\partial x} = 0 \quad (2)$$

$$\text{Sonic speed:} \quad a = \sqrt{\frac{\gamma P}{\rho}} \quad (3)$$

Proper rearranging of Eqs. (1), (2), and (3) yields the following characteristic equations for the method of characteristics:

$$\left[\frac{\partial}{\partial t} + (V + a) \frac{\partial}{\partial x} \right] \left(V + \frac{2a}{\gamma - 1} \right) = 0 \quad (4)$$

left-running
characteristics

$$\frac{dx}{dt} = V + a \quad (5)$$

$$\left[\frac{\partial}{\partial t} + (V - a) \frac{\partial}{\partial x} \right] \left(V - \frac{2a}{\gamma - 1} \right) = 0 \quad (6)$$

right-running
characteristics

$$\frac{dx}{dt} = V - a \quad (7)$$

where a denotes the sonic speed, x the axial coordinate along pipe, P the static pressure, t the time, γ the specific heat ratio, ρ the fluid density, V the velocity component along x .

A numerical program was written for temporal and spacial solutions of Eqs. (4), (5), (6), and (7). Results of numerical calculations of the flow field are presented later for qualitative comparison with the experimental results.

Description of Test Facility

Pressure wave generator

The pressure wave generator generates pressure waves in test pipes of 3 inches in diameter by accelerating an aluminum piston over an 11-inch distance within the beginning section of the test pipe. This generator consists of three major parts: Driver Section, 6.6 ft. long; Piston Section, 3.2 ft. long; Test Pipe of various lengths up to 210 ft.

Figure 1 shows the driver section and the piston section. The release of compressed air from the driver section by electro-thermally bursting the diaphragm provides the energy to rapidly move the piston and generate the pressure wave in the test pipe. Stopping of the piston was accomplished by a double-acting damping system and a heavy stopper block.

The test pipe, as shown in Figure 2, consisted basically of a seamless galvanized steel pipe of 3-inch diameter. A gap of approximately $1/32$ inch was provided between the aluminum piston and the test pipe. Diameters of the piston and the pipe where the piston moves through, are 3.07 and 3.1 inches in order to prevent air leaks backward against the piston movement. Five instrumentation ports were installed on the test pipe; they were spaced at intervals of 8 and 40 ft. on the upper side of the test pipe, respectively for 42 ft. and 210 ft. pipes.

A diaphragm bursting technique was developed for relatively low burst pressures. The diaphragm was made of mylar sheets. The steel wire attached to the diaphragm was electrically heated and bursted the diaphragm immediately. This method has proved to be reliable for the burst pressures ranging from 20 to 100 psi.

Instrumentation system

Five Hot-Film Sensors (Model 1212-20, Thermo-Systems, Inc.) with Constant Temperature Anemometers (Model 1033A) were used to measure velocities of the unsteady flow of air in the test pipe. The details of sensor installation are shown in Figure 4. The relative frequency response of the sensor selected is 40,000 cps; the nominal resistance 4-8 ohms. The sensors were installed at 8 and 40 ft. apart; the first sensor was located at 3 and 10 ft. from the pipe entrance; the fifth sensor was located at 5 and 40 ft. upstream of the pipe exit; respectively for 42 and 210 ft. pipes.

Five channels of voltage outputs from the anemometer system were recorded on an oscillograph (CEC Datagraph 5-133) at a writing speed of 160 in/sec. The sensor calibration curves were established for all sensors, using a sensor calibrator (Thermo-Systems Model 1125) along with a precision manometer and a thermometer.

Test procedure

During and after the calibration, the anemometer outputs were connected without any alteration to the oscillograph set at the desired recording speed. The driver section with a mylar diaphragm was then pressurized to a desired pressure (20, 40, 60, 80 or 100 psi), while the piston section was carefully checked for its smooth movement within the test pipe and its initial position. As the exact pressure measured by a precision pressure gage was reached in the driver section, the diaphragm was bursted by electrically heating a circled wire attached to the diaphragm. Approximately two seconds before the diaphragm bursting, operation of the oscillograph was started. Recording of the voltage outputs from the anemometers was then accomplished.

Presentation and Discussion of Experimental Data

The experimental data collected from a series of tests for five burst pressures, 20, 40, 60, 80 and 100 psi, are presented in graphical form. Sufficient number of repetitions, say more than three, was made on each test to ensure the repeatability and consistency of the data.

Figure 3 shows Sensor Positions A, B, C, D, and E across a pipe section. Figure 4 presents a typical oscillograph recording of voltage outputs from the five sensors located at five sections along the test pipe.

Temporal velocity profiles at Sensor Position A in five pipe sections for burst pressures at 100 and 40 psi for 42 ft. pipe are plotted in Figure 6. Comparison of the two sets of profiles indicates that decay of the pressure wave is more notable for the case of 40 psi after Section 3. The case of 100 psi seems to indicate that the wave propagation in this length of pipe yields less decay. The acceleration of the propagated wave recorded at Section 5 for both pressures was caused by the expansion wave reflected negatively from the pipe exit. With the propagation speed of approximately 1100 ft/sec, the pressure wave took about 10 milliseconds to reflect back from the pipe exit to Section 5, causing the flow to accelerate. A slight irregularity of the profile at Section 3 has been determined to be strictly instrumental by comparative tests with other sensors installed at the same section.

The steep bends occurred on the velocity profile at Section 5 is considered to be primarily caused by the wave reflection at the pipe exit. In order to ascertain this, an identical test was performed for a 21-ft. pipe of the same diameter. Test results of velocity profiles from the 21-ft. pipe are presented in Figure 7 for comparison with data from the 42-ft. pipe under the same test conditions. The velocity profile at Section 3 which is closest to the exit of the 21-ft. pipe is shown to be characteristically similar to the velocity profile of Section 5 near the exit of the 42-ft. pipe. This comparison of data from two different pipe lengths evidently illustrates the cause of peculiarity of the velocity profile at the section near the pipe exit.

Figures 7, 8, and 9 depict temporal velocity profiles for Sensor Position A at each of five sections respectively, for burst pressures of 40, 60, and 80 psi for 210-ft. pipe. The existence of these phenomena was ascertained by repeated measurements under the same test conditions.

Calculated results of temporal velocity profiles using the method of characteristics, (Eqs. 4-11), with measured boundary conditions from the piston movement were compared with the experimental data for burst pressures of 40 and 80 psi. The calculations were carried out with the use of UNIVAC 1108 electronic computer. The piston movement was recorded and analyzed with a Fastex high speed movie camera at the rate of approximately 4500 frames per second. Since the mathematical model was established based on isentropic assumptions, the experiment clearly demonstrated that the flow process associated with the wave propagation was not isentropic, observing a significant effect of frictional resistance against the flow which is subsonic throughout the pipe. As the energy dissipation takes place along the pipe, the static pressure tends to decrease along the pipe while the velocity decreases rather significantly at a fixed position comparing with the isentropic case. These phenomena can be illustrated qualitatively by the following equation modified from Equation (1) for unsteady one-dimensional flow in a pipe with friction:

$$\frac{\partial V}{\partial t} = -\frac{1}{\rho} \frac{\partial P}{\partial x} + \frac{1}{\rho} \frac{\partial \tau_w}{\partial x} - V \frac{\partial V}{\partial x} \quad (8)$$

where $\tau_w = \tau_1 \approx f \rho \frac{V^2}{2}$: shearing stress along the pipe wall. While the convective acceleration, $V \frac{\partial V}{\partial x}$ is experimentally known to be reasonably small in this case, and a minor positive contribution to $\frac{\partial V}{\partial t}$ is made by the increase in negative pressure gradient, a predominant negative contribution to the temporal acceleration, $\frac{\partial V}{\partial t}$ is made by the shearing stress term as demonstrated in both Figures 7 and 9. It is noteworthy that a greater deviation of the experimental velocity profile from the calculated isentropic data was observed for the case of 40 psi burst pressure, agreeing with the theoretical consideration based on Equation (8). Also, it is significant to note that the wave fronts of both cases propagated nearly isentropically as evidenced by the close agreement shown in both Figures 7 and 9.

Figures (10) and (11) present a comparison of numerical calculations with and without friction at burst pressures of 40 and 80 psi. The calculations considering friction were made with a friction coefficient of $f = 0.2$. The rate of acceleration is found to be subject to the influence of friction. This influence is small in the pipe section near the piston; but the effect of friction is growingly pronounced in the direction of propagation of the pressure wave.

Figure 10 also demonstrates in a different form these peculiar phenomena of velocity distributions across Section 1 and 2 for two time frames respectively, at 100 and 20 psi burst pressures. Having determined through sensor calibrations that all hot-film sensors were functioning with a reasonable accuracy, say less than 15% in error,

the investigators have determined that the peculiar phenomena may be due to the energy dissipation caused by frictional resistance along the wall. The effect of friction has been considered predominant to the phenomena. However, further investigations and data analysis based on the consideration of energy balance and pressure distribution are required before making conclusive statements on these phenomena.

Figure 11 presents propagation speeds of the pressure waves varying along the pipe for five burst pressures. The propagation speed was noted to remain constant for most cases with the statistical mean of 1100 ft/sec and the variance of less than 25 (ft/sec)². No correlation among the axial pipe distance, the burst pressure and the propagation speed was obviously noted.

Average temperature and pressure of the test medium, air, were 75° F, and 29.56 in. Hg absolute under the static condition throughout the test.

This paper is intended for the presentation of experimental data with a limited analysis of the data because of its lack of supporting data, such as pressure distributions along and across the pipe. With some simplifying assumptions, further analysis of the data through dimensionless parameters may be conducted. However, the author has preferred to present the data in original dimensional form and retained the complete data analysis for a later publication.

References

1. Burgers, J., "A Mathematical Model Illustrating the Theory of Turbulence," *Advances in Applied Mechanics*, Academic Press, 1948.
2. Hopf, E., "The Partial Differential Equation $u_t + uu_x = \mu_{xx}$," *Communications on Pure and Applied Mathematics*, Vol. III, pp. 201-230, 1950.
3. Cole, J.D., "On a Quasi-Linear Parabolic Equation Occurring in Aerodynamics," *Quarterly of Applied Mathematics*, Vol. IX, No. 3, pp. 225-236, Oct. 1951.
4. Lighthill, M.J., "Surveys in Mechanics," edited by G. K. Batchelor and R.M. Davis, Cambridge University Press, pp. 250-351, 1956.
5. Rodin, E.Y., "Propagation of Waves of Finite Amplitude in Thermoviscous Media," Report WR66-37, Wyle Laboratories under Contract NAS8-11312, "Propagation of One and Two-Dimensional Waves of Finite Amplitude," Report WR67-18, Wyle Laboratories under Contract NAS8-21060.
6. Blackstock, D.T., "Propagation of Plane Sound Wave of Finite Amplitude in Nondissipative Fluids," *J. of Acoustical Society of America*, Vol. 34, No. 1, pp. 9-30, Jan. 1962.
7. Nakamura, A. and Takeuchi, R., "Propagation of Sound Pulses Through Pipes," *Acustica*, Vol. 22, pp. 88-95, 1969-70.
8. Kantola, R., "Transient Response of Fluid Lines Including Frequency Modulated Inputs," ASME Paper No. 70-WA/FIcs-1.
9. Strunk, R.D., "Transient Response of Fluid Lines Through Use of Infinite Products," ASME Paper No. 70-WA/FE-22.
10. Sawley, R.J. and White, P.H., "Energy Transmission in Piping Systems and Its Relation to Noise Control," ASME Paper No. 70-WA/Pet-3.
11. Brown, F.T., "The Transient Response of Fluid Lines," *J. of Basic Engineering*,

- Trans. ASME, Series D, Vol. 84, No. 3, p. 547, Dec. 1962.
12. D'Souza, A.F. and Oldenburger, R., "Dynamic Response of Fluid Lines," J. of Basic Engineering, Trans. ASME, Series D, Vol. 86, No. 2, pp. 589-598, Sept. 1964.
 13. Schuder, C.B. and Binder, R.C., "The Response of Pneumatic Transmission Lines to Step Inputs," J. of Basic Engineering, Trans. ASME, Series D, Vol. 81, No. 4, p. 578, Dec. 1959.

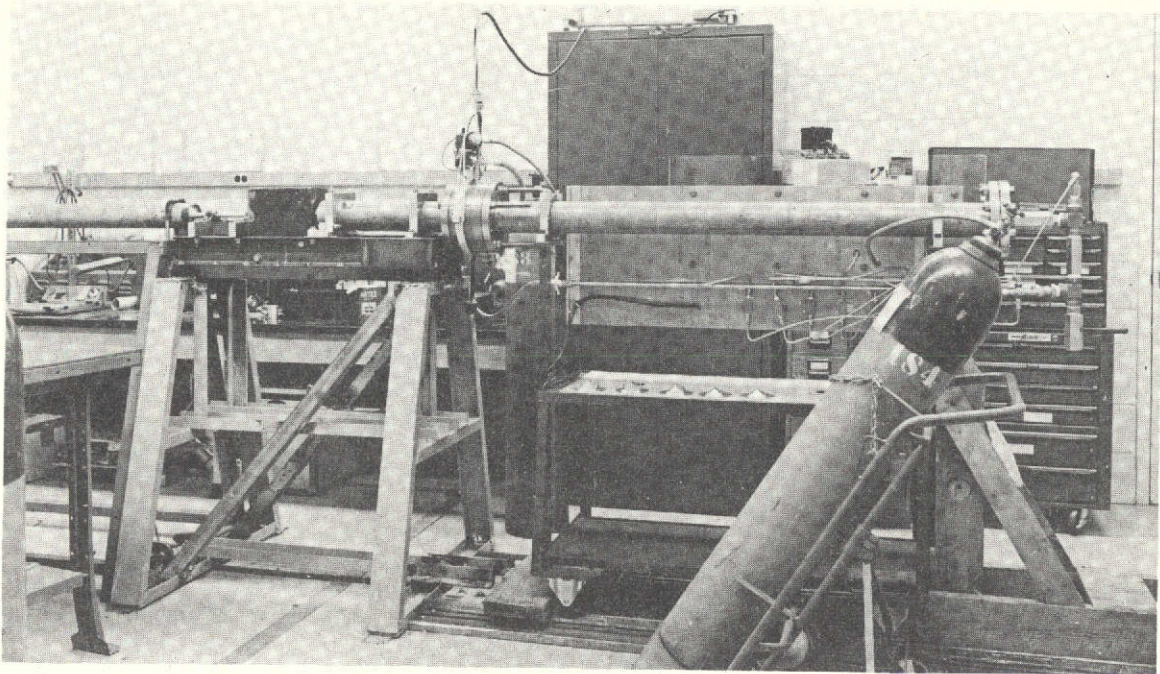


Fig. 1 General View of Driver Section (right), Piston Section and Test Pipe (left) of Pressure Wave Generator.

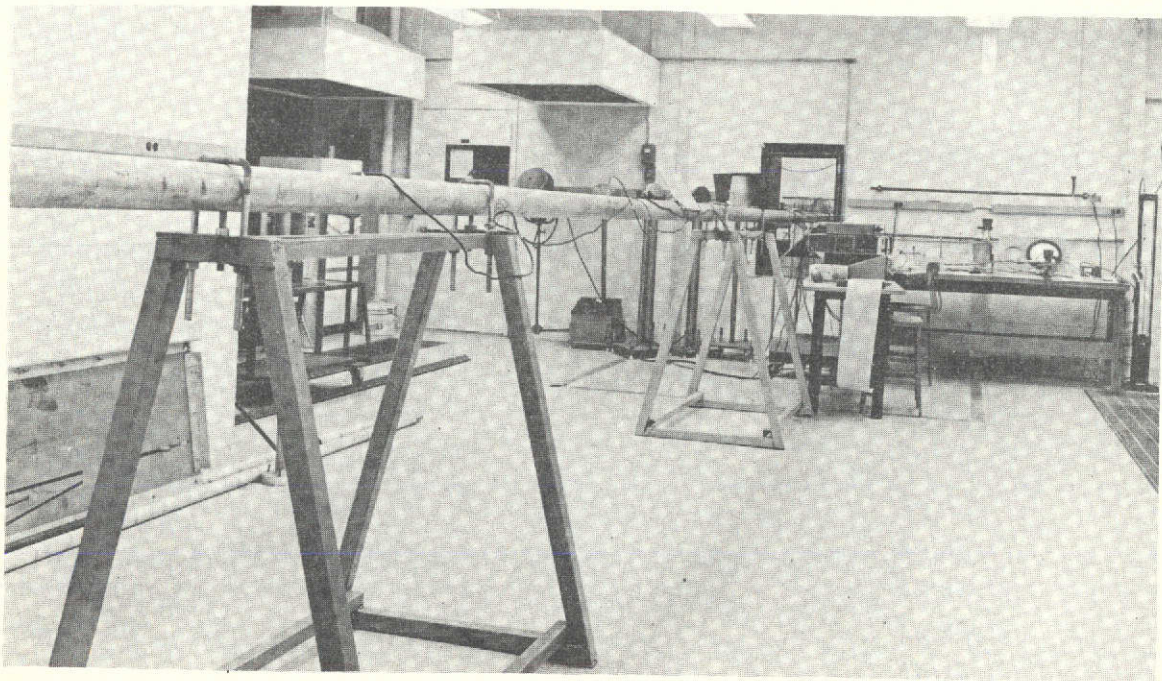


Fig. 2 General View of Test Pipe.

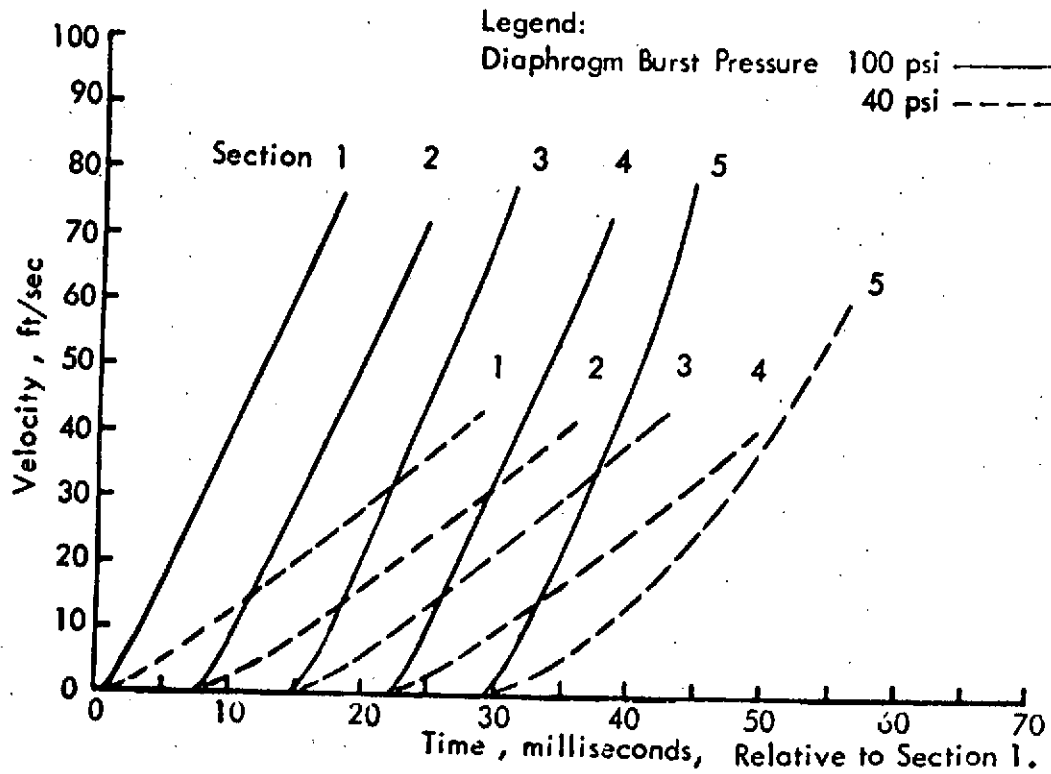


Fig. 5 Flow Velocity Versus Time at Sensor Position A in 5 Pipe Sections for Diaphragm Burst Pressures at 100 and 40 psi.

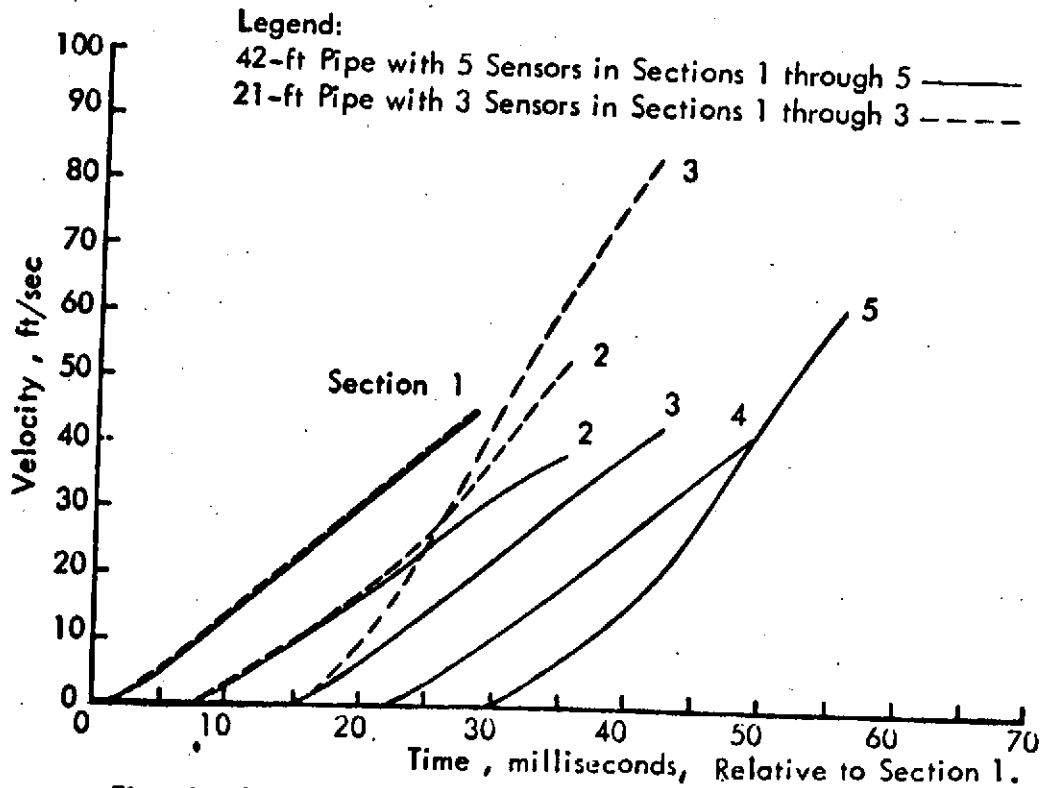


Fig. 6 Flow Velocity Versus Time for 2 Different Pipe Lengths at Diaphragm Burst Pressure of 40 psi.

Legend:
— Theoretical
○ ○ ○ Experimental

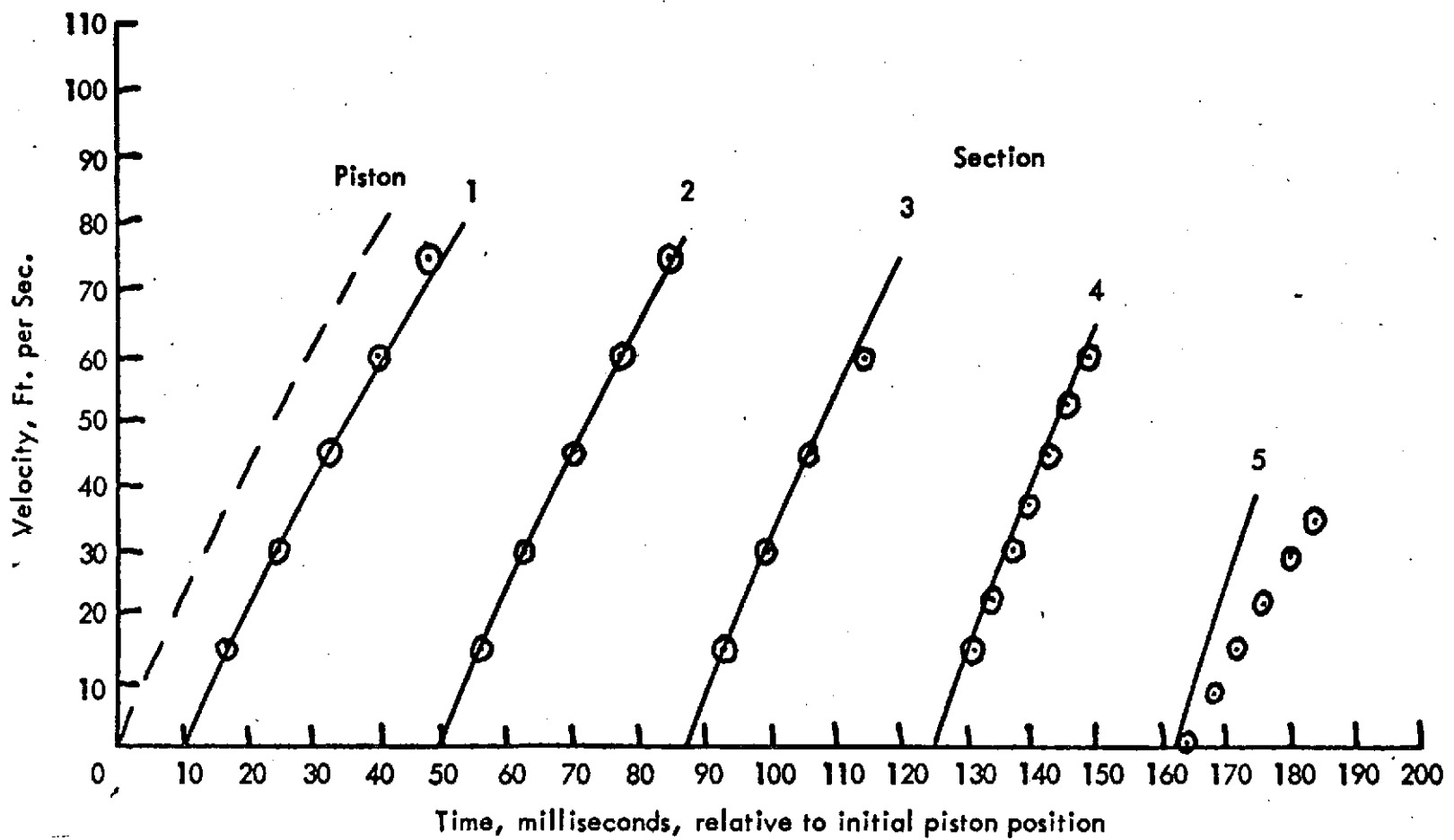


Fig. 7 Comparison of Numerical Calculations with Experimental Data. Burst Pressure 40 psi, Sensor Position

Legend:

— Theoretical

○ ○ ○ Experimental

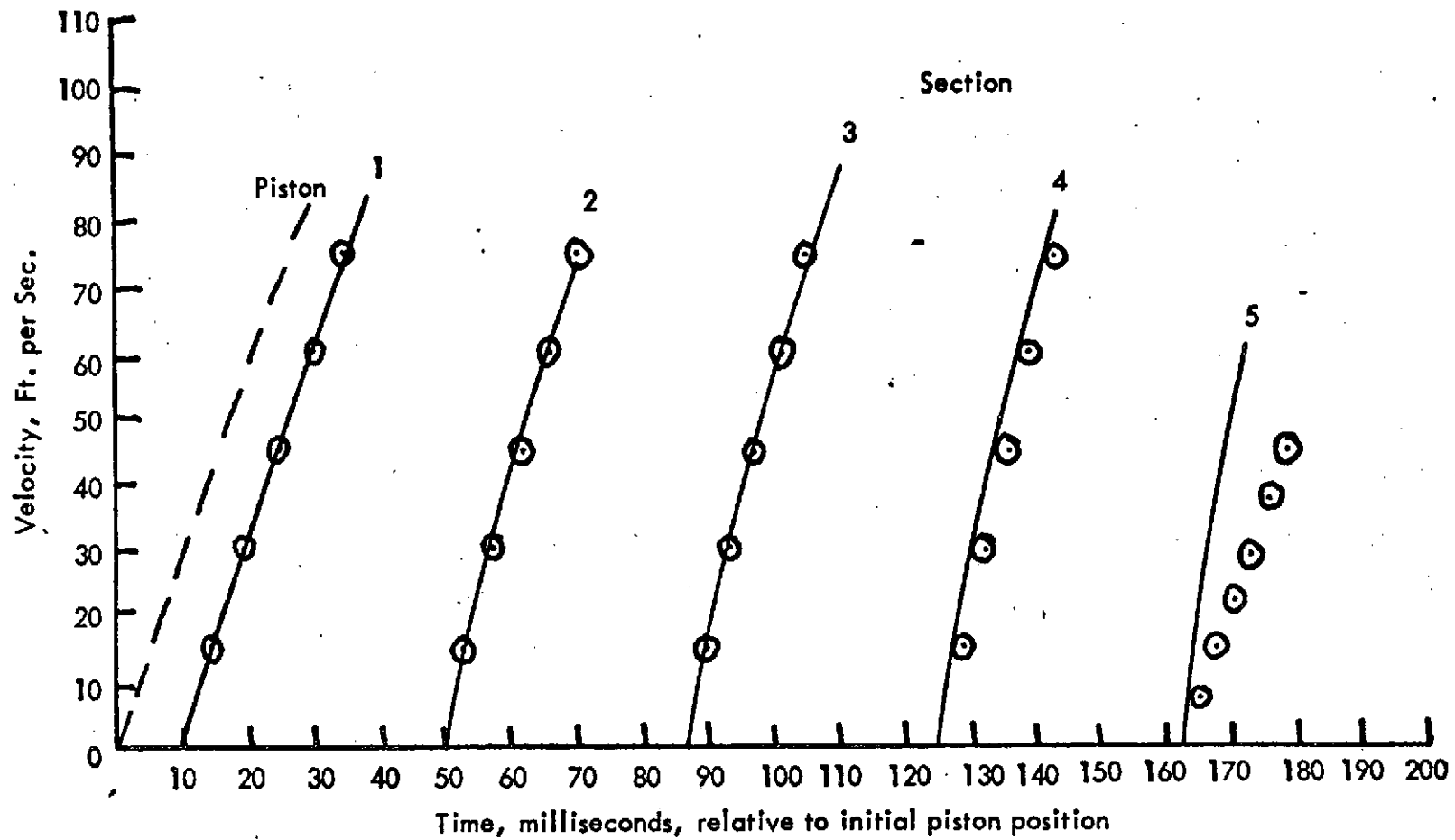


Fig. 8 Comparison of Numerical Calculations with Experimental Data. Burst Pressure 60 psi, Sensor Position A.

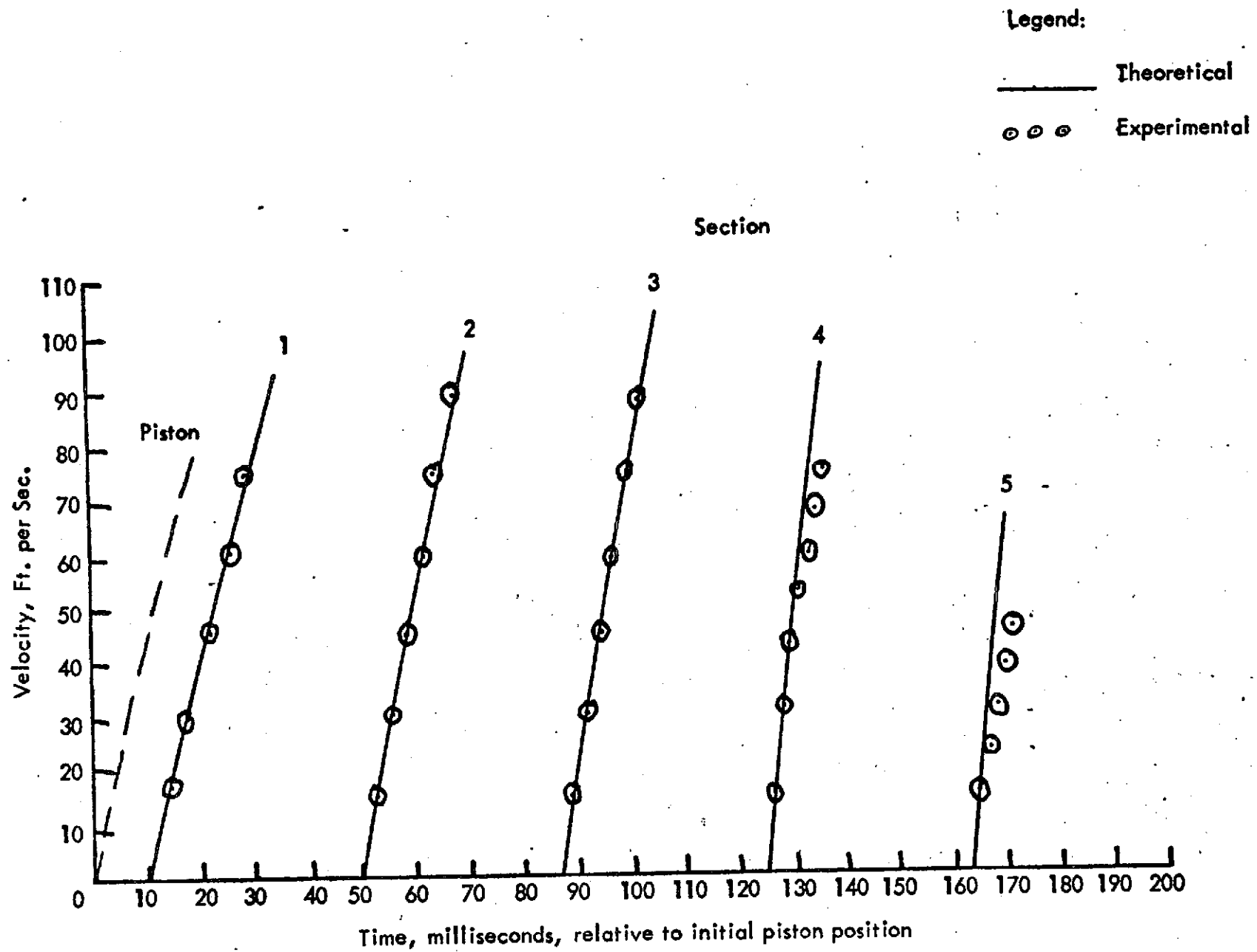


Fig. 9 Comparison of Numerical Calculations with Experimental Data. Burst Pressure 80 psi, Sensor Position A

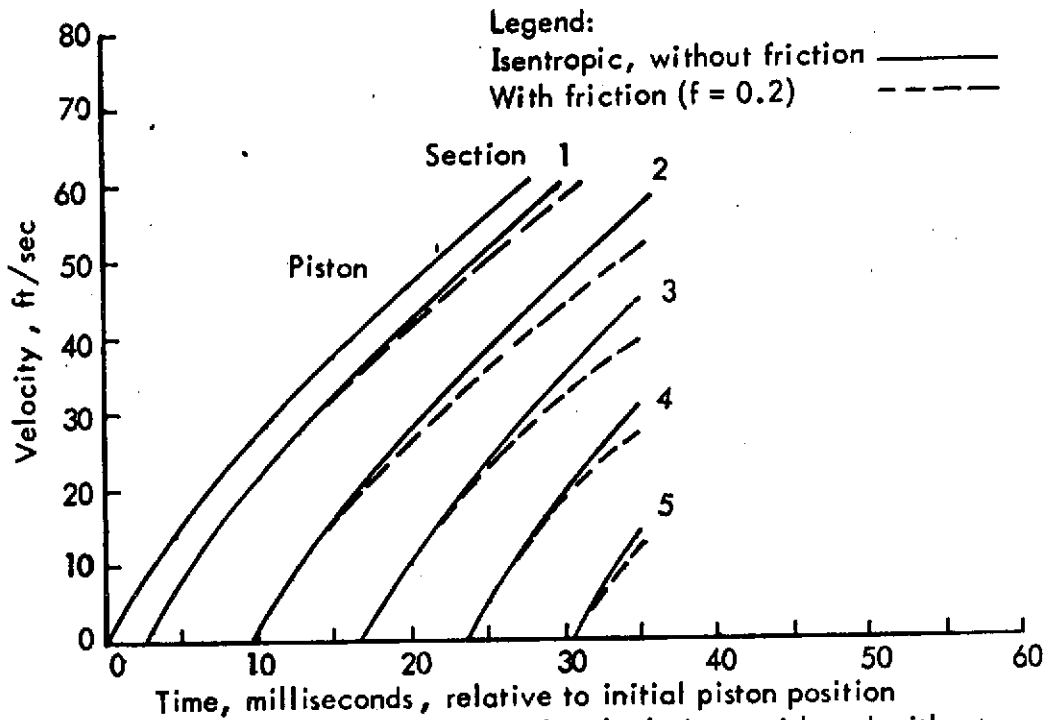


Fig. 10 Comparison of Numerical Calculations with and without Friction (f=0.2) at Burst Pressure 40 psi and Sensor Position A.

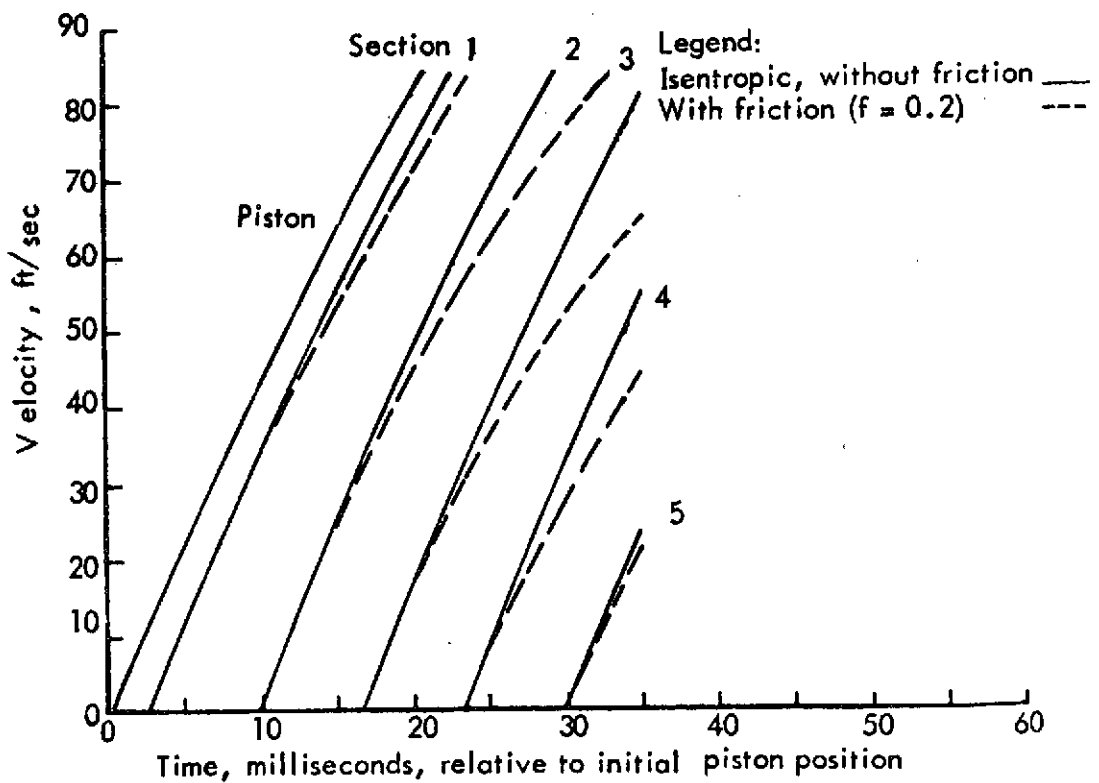


Fig. 11 Comparison of Numerical Calculations with and without Friction (f=0.2) at Burst Pressure 80 psi and Sensor Position A.

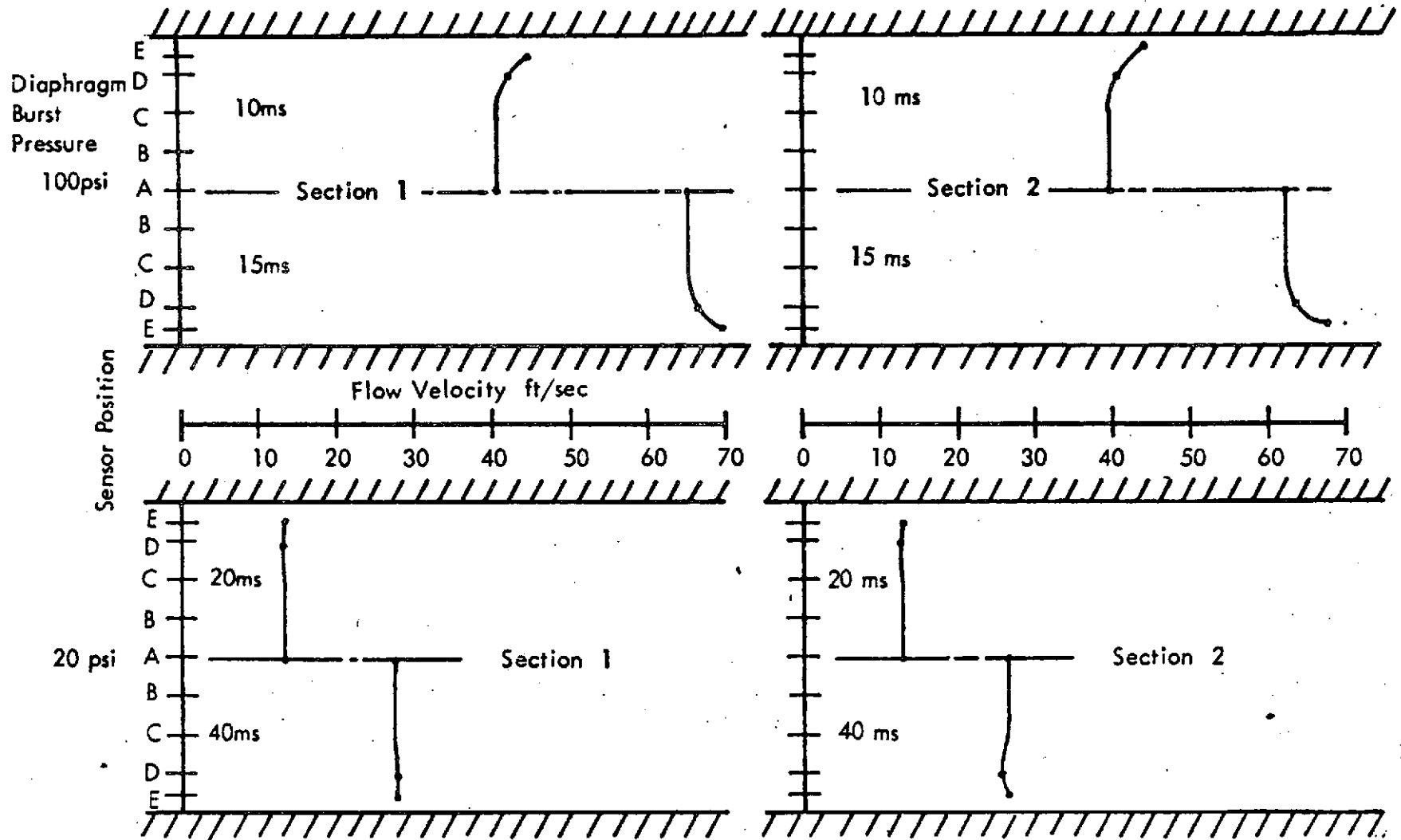


Fig. 12 Velocity Profiles at 2 Time Frames in 2 Pipe Sections for Diaphragm Burst Pressures of 100 psi and 20 psi.

Legend: Sensor Position A ● D △
 C ▽ E □

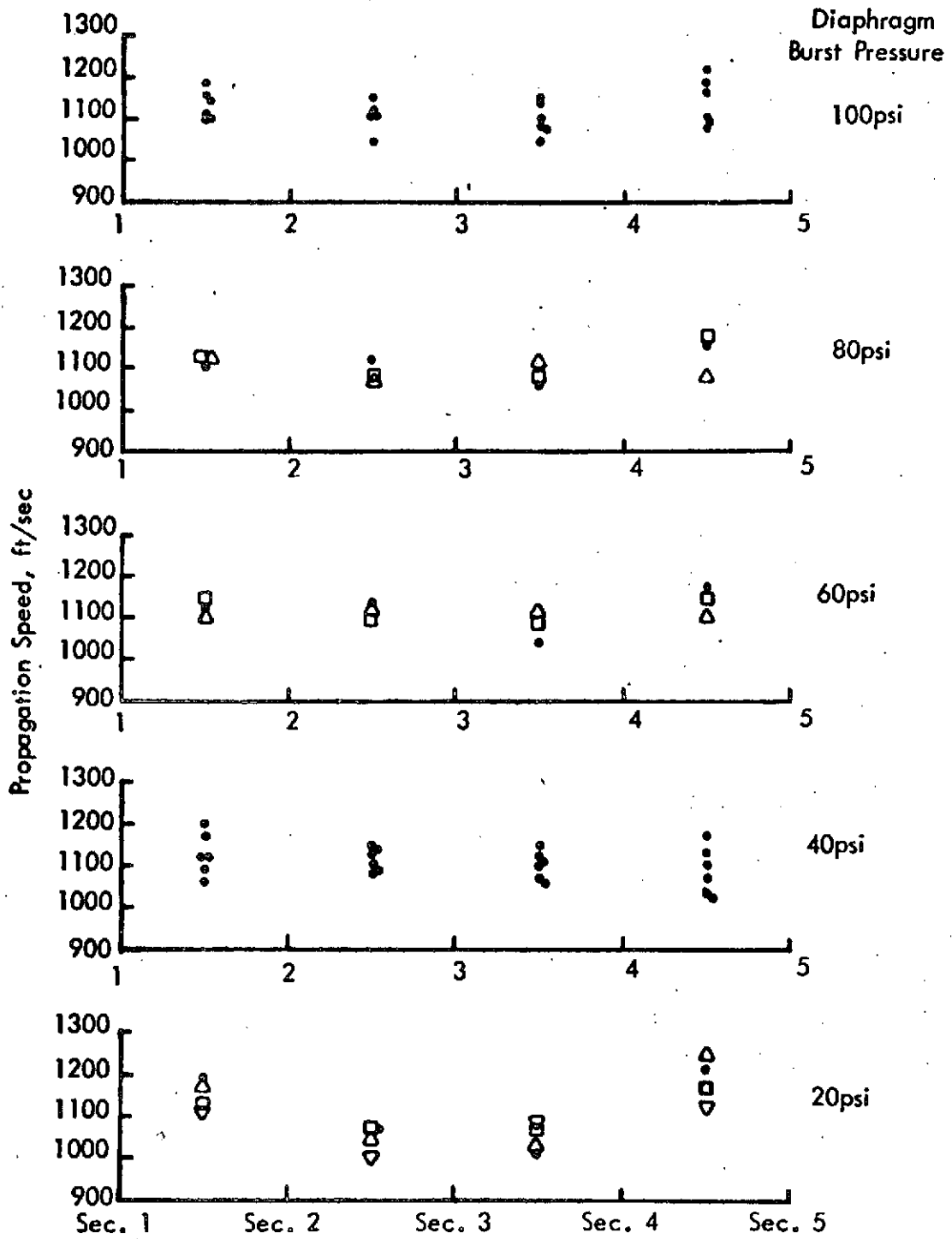


Fig. 13 Propagation Speed of Pressure Wave Versus Axial Distance along Pipe.

SECTION IB

**ATTENUATION CHARACTERISTICS OF NON-LINEAR PRESSURE
WAVES PROPAGATING IN PIPES**

SECTION IB

ATTENUATION CHARACTERISTICS OF NON-LINEAR PRESSURE WAVES PROPAGATING IN PIPES

INTRODUCTION

Phenomena of non-linear pressure waves of finite amplitude propagating in the near sound field have been of considerable interest in recent years because of their effects on the environment. There are numerous studies on the phenomena through the Burgers' equation based on one-dimensional approximation, as noted in the authors' recent paper [1]*. A typical application of these studies is the wave propagation in pipes. Recent studies on the wave propagation in pipes have been reported by Blackstock [2], Nakamura and Takeuchi [3], Kantola [4], Strunk [5], Sawley and White [6], Brown [7], D'Souza and Aldenburger [8], Schuder and Binder [9], and Uchida [10]. These studies are either the treatment of small-amplitude waves, shock waves, plane waves of finite amplitude, in inviscid or incompressible fluid. Some of them were verified experimentally, but none of them, to the authors' knowledge, treats the propagation of non-linear pressure waves of large amplitude in pipes by measuring velocity distributions or profiles throughout the pipe, in order to gain better understanding of the energy dissipation mechanism.

As a step forward in this endeavor, the author [1] reported an experimental investigation of temporal and spacial velocity profiles of fluid flow in a 3-inch openend pipe of various lengths, produced by the propagation of non-linear pressure waves at several magnitudes. Experimental results were presented in graphical form and compared with theoretical results obtained by the method of characteristics with the isentropic assumption.

This paper presents improved results of the continuing study of propagation phenomena of the pressure waves in the pipes and provides theoretical explanations of peculiar configurations of the velocity profiles for the unsteady flow caused by the wave propagation. Also, the attenuation characteristics of non-linear pressure waves propagating in the pipes were experimentally investigated and analyzed through comparison with two theoretical models, one without friction and one with friction. The analysis resulted in a functional relationship among the friction coefficient, flow and pipe parameters.

*Numbers in [] brackets refer to references.

THEORETICAL CONSIDERATION

a) Method of Characteristics for Wave Attenuation

Considering the physics of the phenomena involved in unsteady irreversible flow of compressive fluid in general yields the following equations of momentum, energy and continuity:

$$\frac{D V_i}{D t} + \frac{1}{\rho} \frac{\partial T_{ij}}{\partial x_j} = 0 \quad (1)$$

$$\frac{D E}{D t} = -\frac{1}{\rho} \tau_{ij} e_{ij} + \frac{1}{\rho} \frac{\partial}{\partial x_i} \left(k \frac{\partial T}{\partial x_i} \right) \quad (2)$$

$$\frac{\partial V_i}{\partial x_i} + \frac{1}{\rho} \frac{D \rho}{D t} = 0 \quad (3)$$

Where V_i denotes the velocity vector, T_{ij} the stress tensor, E the internal energy, e_{ij} the rate of strain tensor, T the temperature, ρ the density, and k the thermal conductivity.

Rearranging of Eqs. (1), (2), and (3) based on one-dimensional approximation with linearized diffusion yields a simplified expression as follows, for plane pressure waves of finite amplitude, according to Lighthill [11]:

$$\frac{\partial V}{\partial t} + V \frac{\partial V}{\partial x} + \frac{2a}{\gamma-1} \frac{\partial a}{\partial x} = \delta \frac{\partial^2 V}{\partial x^2} \quad (4)$$

$$\frac{\partial a}{\partial t} + V \frac{\partial a}{\partial x} + \frac{\gamma-1}{2} a \frac{\partial V}{\partial x} = 0 \quad (5)$$

Where δ denotes the diffusivity defined by Lighthill as

$$\delta = \nu \left[\frac{4}{3} + \frac{\mu_0}{\mu} + \frac{\gamma-1}{Pr} \right] \quad (6)$$

Where ν is the kinematic viscosity, μ_0 the dilatational viscosity, μ the dynamic viscosity, Pr the Prandtl number, γ the specific heat ratio, $V = V(x,t)$ the fluid particle velocity component along x axis which is coaxial with the pipe, a the speed of an isentropic infinitesimal sound wave at local pressure and density, $a = \sqrt{\gamma P / \rho}$.

The approximation applied to the theoretical model has made it possible to reduce the three fundamental equations to two relatively simple equations. However, some cautionary remarks are essential in regard to their applicability for the real fluid flows of interest in this paper.

The simplified model represented by Eqs. (4) and (5) is assumed to represent plane pressure waves of finite amplitude with linearized diffusion effects propagating in X-direction. The diffusion effects are linearized by neglecting non-linear terms of low order involved in the energy diffusion process due to viscosity and heat conduction as well as relaxation. The relaxation is referred to a process of departure from equilibrium distribution of energy in the internal degrees of molecular freedom of the fluid under the wave propagation. In this study, the attenuation of pressure waves is considered with the provision that the wave frequency is small compared with the reciprocals of the relaxation times of the internal degrees of molecular freedom.

It may be deduced that attenuation characteristics of the wave propagation are attributable to linearized terms of diffusion effects, namely the viscosity and heat conduction, as theorized by Lighthill for pressure waves of finite amplitude.

Examination of Eqs. (4) and (5) indicates that the left-hand sides of the equations are the exact forms of the equations of sound waves of finite amplitude under isentropic assumption and they constitute the classical theory of shock-wave formation due to the wave-form-steepening tendency of the convective terms in the equation of motion, while the right-hand sides are an approximation to the diffusion effects by linearization.

It should be noted that the approximation will yield a reasonably accurate analysis of the phenomena as long as the entropy change in the thermal system is sufficiently small, say in the order of $\gamma\omega/a^2$ at most. ω denotes the angular velocity in radians per second. For a specific application to the pipe flow, the right-hand side of Eq. (4) representing the diffusion effects as a cause of attenuation, may be modified, recognizing that frictional resistance developed along the pipe wall is the predominant diffusion effect contributing to attenuation characteristics. Since the frictional resistance due to wall shear has been expressed conventionally by $\tau_w \pi D \delta X$ where

τ_w denotes the wall shear, D the pipe diameter, δX the pipe length, and the inertial force is $A \rho \delta X \frac{dV}{dt}$, the right-hand side of Eq. (4) may be conveniently equated as,

$$\delta \frac{\partial^2 V}{\partial X^2} = - \frac{\tau_w \pi D}{\rho A} = - \frac{4 \tau_w}{\rho D} \quad (7)$$

Where $A = \frac{D^2 \eta}{4}$ denotes the pipe cross-sectional area.

For steady viscous flows, the wall shear along the pipe, τ_w has been well accepted as a function of Darcy-Weisbach's friction coefficient and other flow quantities.

For Eqs. (10) and (11) along the C^+ characteristics,

$$\begin{aligned} VR(n) - V(n-1) + \frac{2}{\gamma-1} [aR(n) - a(n-1)] \\ = -\frac{f\Delta t}{4D} [V(n-1)|V(n-1)| + VR(n)|VR(n)|] \end{aligned} \quad (14)$$

$$\frac{\Delta X_1}{\Delta t} = \frac{1}{2} [V(n-1) + VR(n) + a(n-1) + aR(n)] \quad (15)$$

For Eqs. (12) and (13) along the C^- characteristics,

$$\begin{aligned} VR(n) - V(n+1) - \frac{2}{\gamma-1} [aR(n) - a(n+1)] \\ = -\frac{f\Delta t}{4D} [V(n+1)|V(n+1)| + VR(n)|VR(n)|] \end{aligned} \quad (16)$$

$$\frac{\Delta X_2}{\Delta t} = \frac{1}{2} [V(n+1) + VR(n) + a(n+1) + aR(n)] \quad (17)$$

and

$$\Delta X = \Delta X_1 + \Delta X_2 \quad (18)$$

With proper values of $f, \Delta X$, and input conditions of the pressure waves specified, Eqs. (14), (15), (16) and (17) are solved simultaneously with a sufficient number of ΔX and respective time steps Δt which form a grid for numerical calculations of VR and aR in a continuous fashion at junctions of the C^+ and C^- characteristics. For completing the calculations, proper boundary conditions at both ends of the pipe are required. Since the numerical scheme is relatively elementary, details of the numerical procedure and computer program to be used with UNIVAC 1107 high-speed computer are omitted for the sake of brevity.

b) Approximate Theoretical Model of Velocity Profiles Across the Pipe Section

Although Eqs. (1), (2) and (3) are general enough to form a theoretical model of cross-sectional velocity profiles along the pipe for unsteady flow generated by the pressure wave of finite amplitude, but the exact solution of the model is extremely difficult to obtain because of the mathematical complexity and nonlinearity.

Review of literature has resulted in finding Uchidas' [10] work on the pulsating viscous flow superposed on the steady laminar motion of incompressible fluid in a circular pipe. His study is limited to one-dimensional laminar flow of incompressible fluid with superposition of pulsating flows expressed in Louriier series. However, for

the purpose of qualitative comparison with experimental results of the cross-sectional velocity profiles from the present study, his exact solution is presented below,

$$V = \frac{K_0}{4\gamma} (r_0^2 - r^2) - \sum_{s=1}^{\infty} \frac{i K_s}{S} \left[1 - \frac{J_0(\beta r i^{3/2})}{J_0(\beta r_0 i^{3/2})} \right] e^{ist} \quad (19)$$

Where K_0 and K_s are constants representing the amplitudes of elemental pulsation, r the radial coordinate in the pipe section, r_0 the pipe radius, $\beta = \sqrt{S/\gamma}$, and J_0 the first solution of Bessel function of zero order.

Analysis of Eq. (19) shows that calculated results of the velocity profiles exhibit a configuration with the maximum velocity near the wall. This finding confirms qualitatively the general configuration of measured velocity profiles in this study.

EXPERIMENTAL DATA PRESENTATION AND COMPARISON WITH THEORETICAL MODELS

Experimental apparatus including instrumentation systems used for collecting the data to be compared with the theory developed have been described in details by the author [1], [13], [14] previously. However, for the readers' convenience and continuity in understanding of the paper, a brief but pertinent information on the experiment is presented here. 7.62 cm open-end pipes of 15.85 m and 64.0 m in length respectively, were tested with hot-film and hot-wire anemometers for velocity profiles across the pipe section and along the pipe axis, or centerline of the pipe, of unsteady flows. The unsteady flows in the pipes were generated by the piston thrust into the pipe at various speeds which were regulated by the pressure wave generator in terms of diaphragm burst pressures at 14.05, 28.10, 42.15, 56.20, and 70.26 g/mm². The piston speeds were measured with a laser device and recorded as a function of time. The air temperature was measured at each test for determining the air viscosity. Reynolds numbers of the pipe flow ranged for each burst pressure are listed as follows:

Burst Pressure in g/mm ² (psi)	Reynolds number $N_R = \frac{\gamma D}{\mu}$
14.05 (20)	0 ~ 41,666
28.10 (40)	0 ~ 62,500
42.15 (60)	0 ~ 83,333
56.20 (80)	0 ~ 97,222
70.26 (100)	0 ~ 111,111

The preceding varying Reynolds numbers signifies that the unsteady flows generated by the propagating waves appear to shift the flow regime from laminar to turbulent. With this observation in mind, proper selection of the values of friction coefficients for the numerical calculations as well as their comparisons with the experimental results was made. Also it was concerned that, since the piston was physically displaced only 27.94 cm into the piston in all cases, boundary layer flow on the pipe wall seemed unable to develop fully into the pipe axis. But no measurement has been made to confirm the above concern in this continuing project of study. Each of all experimental data was obtained as a result of conducting a statistically sufficient number of tests to ensure its' repeatability.

Typical velocity profiles across the sections 1 and 2 which are 3.60 m and 16.62 m downstream from the inlet for burst pressures of 20 and 100 psi were measured and presented graphically in Fig. 2. Two half profiles at each section for each burst pressure are shown for two time frames (10 and 15 m sec for 100 psi; 20 and 40 m sec for 20 psi). All of the profiles show a significant rise in velocity near the wall. This phenomena is confirmed by the theoretical results represented by Eq. (19) and also plotted in Fig. 2 for selected parameters βr_0 . The values of βr_0 selected at 10 and 5 are found to be approximately equivalent to the cases of burst pressures 100 and 20 psi, respectively. It must be emphasized, however, that the comparison of the experimental and theoretical velocity profiles across the section is qualitative because the flow treated in the theoretical model is assumed to be entirely in the laminar flow regime and the fluid is considered incompressible.

Some typical velocity distributions along the pipe axis measured in the experiment for burst pressures of 28.10, 42.15, and 56.20 g/mm² are presented in Figs. 3, 4, and 5. These velocity distributions are time-dependent velocity curves at the center of each of five sections (1 through 5) distributed along the pipe at distances of 3.60, 16.62, 29.45, 42.44, 55.40 m respectively, from the pipe inlet. Included also in Figs. 3, 4, and 5 are time-dependent plots of the piston speeds, numerically calculated velocity distributions at corresponding locations for respective input conditions of the pressure waves. One of these curves in each of Figs. 3, 4, and 5 was calculated with the assumption that the entire flow regime in the pipe was fully developed into the laminar type where the friction coefficient of steady flow, $f = 64/N_R$ and

$\nu = 1.6723 \times 10^{-3} \text{ m}^2/\text{sec}$ were adopted for the sake of qualitative comparison for average air temperature of approximately 80°F during the test. Calculations of other velocity distributions are based on the assumptions of fully turbulent flow in the pipe with the friction coefficients, $f = 0.02, 0.08, \text{ and } 0.15$. The isentropic propagation without friction was also calculated and included in Figs. 3, 4, and 5.

Comparison of the experimental and theoretical curves of time-dependent velocity distribution at five sections along the pipe has resulted in the following observations rather than a verification of one by the other:

- a) While repeatability of the experimental curves has been assured through the possible best effort, numerical errors developed in theoretical curves was found to be less than 1% based on a preliminary error analysis [14].
- b) Good agreement between the theoretical and experimental curves is noted for all three pressures near the inlet region, particular Sections 1, 2, and 3, if the friction coefficient is assumed to be of laminar type or $f = 0.02$.
- c) The agreement seems to degradate as the waves propagate downstream. Disagreement is most pronounced at Section 5. However, the use of $f = 0.08$ in the theoretical curve seems to restore some of the agreement.
- d) A perfect agreement between the theory and the experiment is reached as far as the speed of wave toe or the front of the pressure waves propagating through the pipe, i.e. isentropic propagation.
- e) Theoretically, if all assumptions made are valid, the diffusion effects due to viscosity are shown to be compromising with the convective effects which steepen the wave form, in a rather linear trend for the laminar friction and in a non-linear trend for the turbulent friction, as far as the time-dependent velocity distributions are concerned. The non-linear trend is obviously most pronounced for the case of $f = 0.15$ as shown.
- f) Through the comparison, it may be deduced that the diffusion effects conveniently represented by the friction coefficient are a function of space, time and wave magnitude and frequency as well as the relative roughness of the pipe for the unsteady flow of interest.
- g) The theoretical model with laminar friction seems to achieve reasonable agreement with the experiment by using the kinematic viscosity of $0.0016723 \text{ m}^2/\text{sec}$.

Fig. 6 presents a comparison of calculated velocity distributions along 7.62 cm (3 in.) and 2.54 cm (1 in.) pipes of the same length at the burst pressure of 42.15 g/mm^2 (60 psi). It demonstrates theoretically the effect of pipe diameter on the attenuation characteristics under the assumption of $f = 0.02$. Obviously, the reduction in pipe diameter contributes to the non-linear trend of diffusion effects as effectively as the increase in the value of friction coefficient.

The experiment with a 1 in. pipe of the same length was conducted and its results are presented in Figures 7, 8, and 9 for comparison with the numerical calculation based on isentropic assumptions and with the friction coefficient, $f = .02$ for fully turbulent flow at the three burst pressures. In these 1 in pipe experiments the piston velocities were measured to be slightly higher in comparison with the corresponding burst pressures of the 3 in. pipe. However, the effects of diffusion as well as the pipe diameter were clearly demonstrated in the 1 in. pipe experiments as shown in the figures. It may be deduced at this juncture that the diffusion effects expressed in terms of the friction coefficient, f , are functions of space and time for the non-linear propagation of pressure waves in pipes. For the wrought iron pipes of 3 in. and 1 in. in diameter, the friction coefficient, f , may vary from .01 to .08 and the value of f seems to increase as the waves propagate down the pipe.

CONCLUSIONS AND RECOMMENDATIONS

The theoretical models with isentropic assumptions and with friction has been constructed and calculated with the use of the method of characteristics. The numerical calculations, based on the theoretical models, were compared with the experimental results and good agreement between the two was achieved. Through the comparison, the diffusion effects were determined to be a function of space and time and they seemed to increase as the waves propagate down the pipes. The theoretical models presented in appendices A and B are capable of predicting with reasonable accuracy the phenomena of wave propagation in a pipe of a given diameter if the friction coefficient can be defined as a function of space and time along the pipe.

However, the experiments performed so far can only provide a limited insight into the function of space and time for the friction coefficient. Obviously, a continuous effort must be provided to obtain a complete data for the analysis of

the function of space and time for the function coefficient, in order that these findings comparing the diffusion effects can be made useful for the engineering solution of non-linear wave propagations.

REFERENCES

1. Shih, C., "Non-Linear Pressure Wave Propagation in Pipes," Proceedings, Interagency Symposium of University Research in Transportation Noise, Sanford, Calif. USA. March, 1973, pp. 583-598.
2. Blackstock, D.T., "Propagation of Plane Sound Wave of Finite Amplitude in Nondissipative Fluids," J. of Acoustical Society of America, Vol. 34, No. 1, pp. 9-30, Jan. 1962.
3. Nakamura, A. and Takeuchi, R., "Propagation of Sound Pulses Through Pipes," Acustica, Vol. 22, pp. 88-95, 1969-70.
4. Kantola, R., "Transient Response of Fluid Lines Including Frequency Modulated Inputs," ASME Paper No. 70-WA/Flcs-1.
5. Strunk, R.D., "Transient Response of Fluid Lines Through Use of Infinite Products," ASME Paper No. 70-WA/FE-22.
6. Sawley, R.J. and White, P.H., "Energy Transmission in Piping Systems and Its Relation to Noise Control," ASME Paper No. 70-WA/Pet-3.
7. Brown, F.T., "The Transient Response of Fluid Lines," J. of Basic Engineering, Trans. ASME, Series D, Vol. 84, No. 3, p. 547, Dec. 1962.
8. D'Souza, A.F. and Oldenburger, R., "Dynamic Response of Fluid Lines," J. of Basic Engineering, Trans. ASME, Series D, Vol. 86, No. 2, pp. 589-598, Sept. 1964.
9. Schuder, C.B. and Binder, R.C., "The Response of Pneumatic Transmission Lines to Step Inputs," J. of Basic Engineering, Trans. ASME, Series D, Vol. 81, No. 4, p. 578, Dec. 1959.
10. Uchida, S., "The Pulsating Viscous Flow Superposed on the Steady Laminar Motion of Incompressible Fluid in a Circular Pipe," ZAMP Vo. VII, 1956 p. 403-421.
11. Lighthill, M.J., "Surveys in Mechanics," Edited by G.K. Batchelor and R.M. Davis, Cambridge University Press, pp. 250-351, 1956.
12. Streeter, V., "Water-Hammer Analysis of Pipelines," J. Hydraulics Div. ASCE, Vol. 90, No. HY4, pp. 151-172, July, 1964.
13. Shih, C., "Experimental Investigation of Pressure Wave Propagation in a Pipe," Proceedings, VIII International Shock Tube Symposium, London, England, July 1971 (with M. J. Loh).

REFERENCES (Continued)

14. Shih, C., "Investigation of Scaling Characteristics for Defining Design Environments Due to Transient Ground Winds and Near-Field, Non-Linear Acoustic Fields," Tech. Report (Contract NAS8-30159) MSFC/NASA-UAH May 1971.

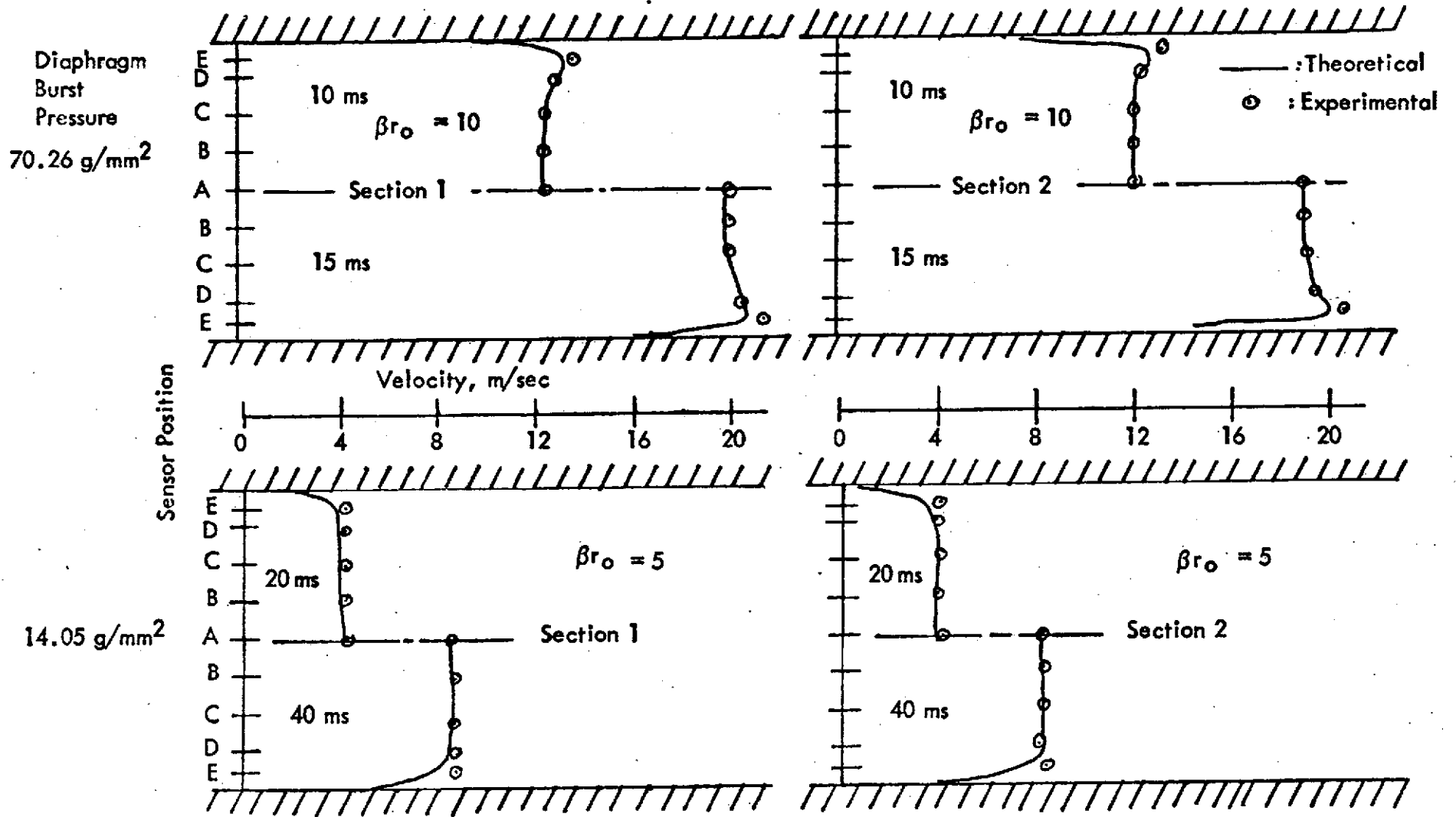


Fig. 2. Velocity Profiles at 2 Time Frames in 2 Pipe Sections for Diaphragm Burst Pressures of 70.26 g/mm² and 14.05 g/mm² compared with approximate Theoretical Models.

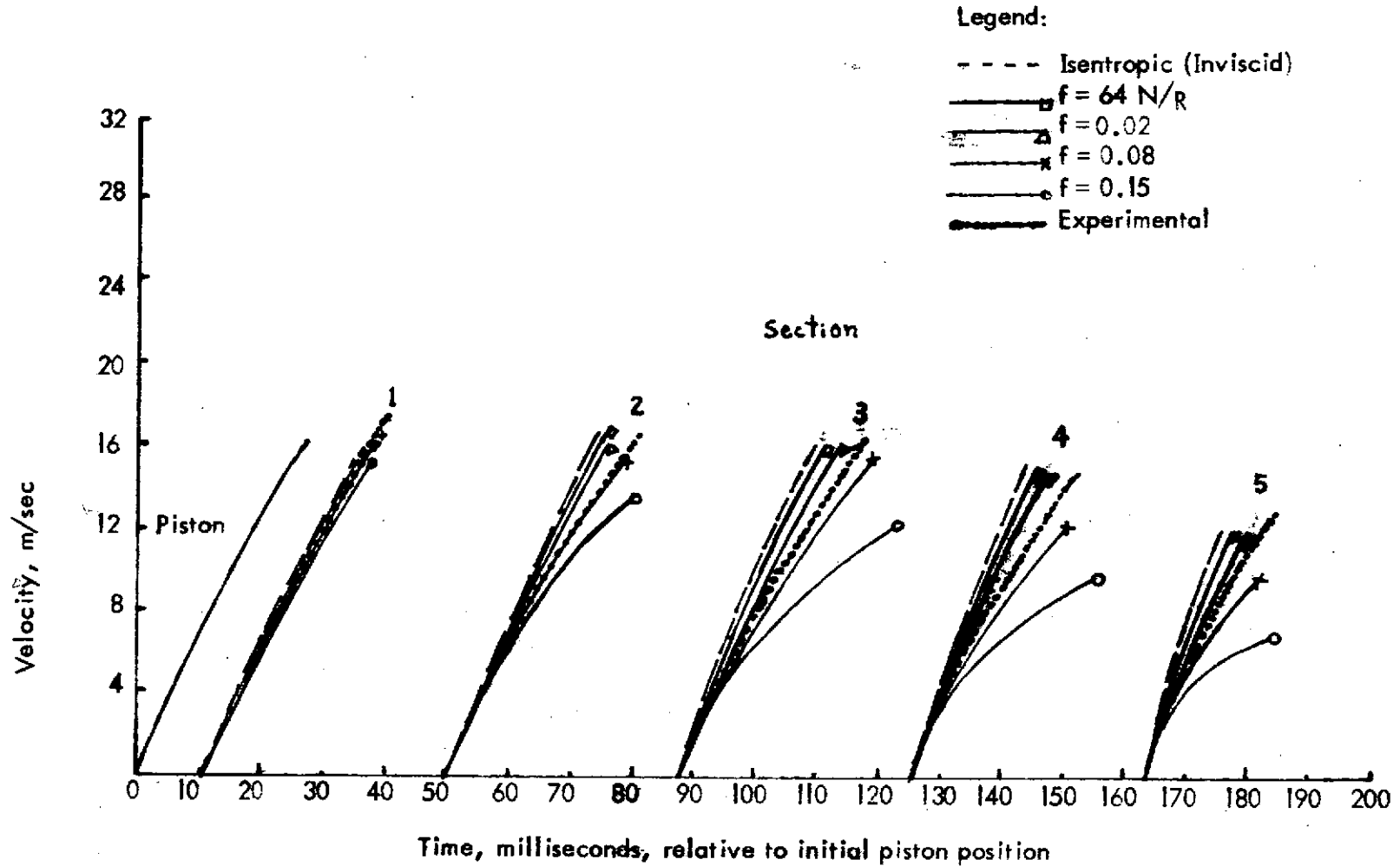


Fig 3 Comparison of Numerical Calculations with Experimental Data for Burst Pressure 28.10 g/mm² and Sensor Position A at Sections 1 through 5 in 7.62 cm pipe.

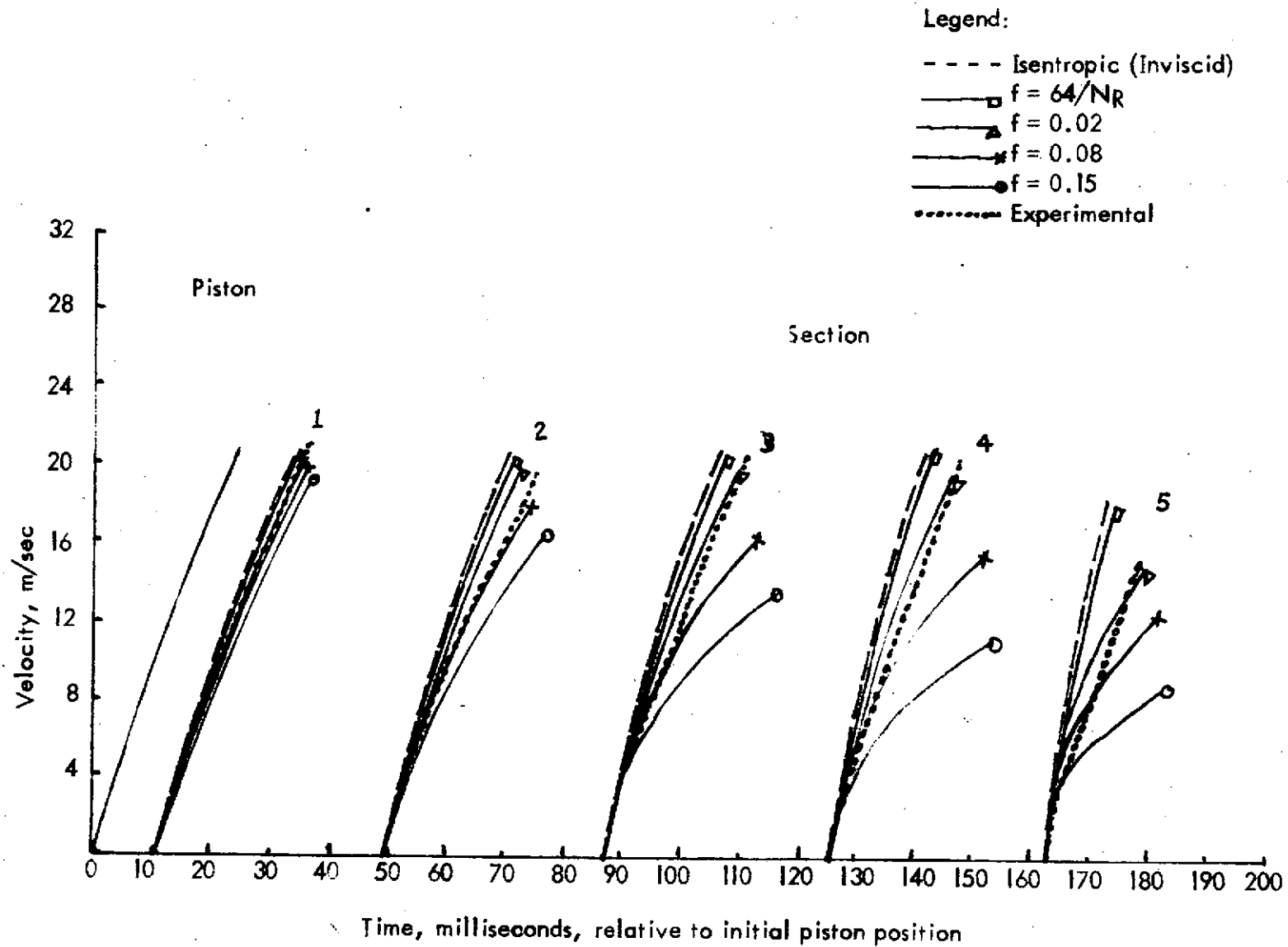


Fig. 4 Comparison of ~~Numerical~~ Calculations with Experimental Data for Burst Pressure 42.15 g/mm^2 and Sensor Position A at Sections 1 through 5 in 7.62 cm pipe.

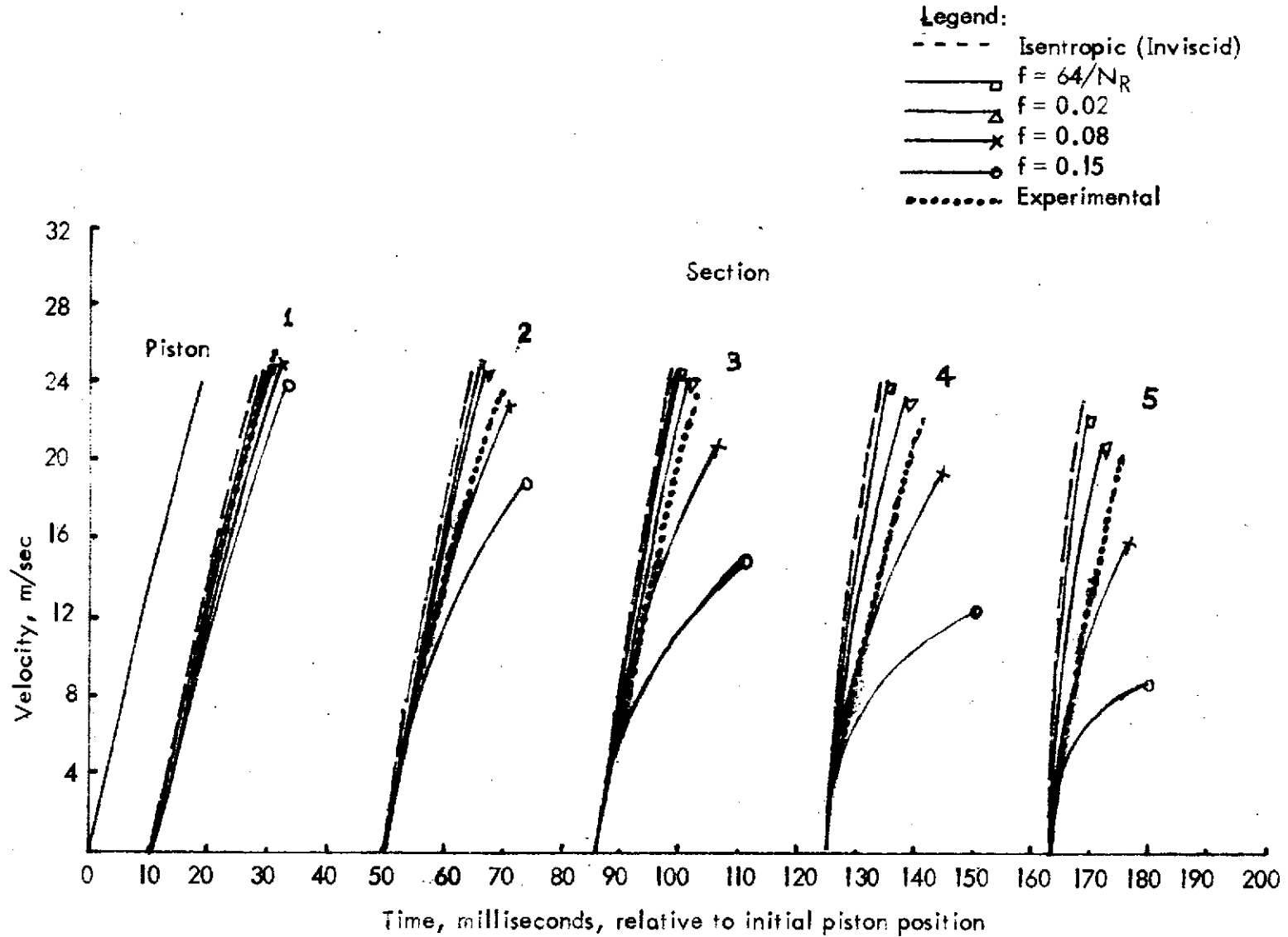


Fig. 5 Comparison of Numerical Calculations with Experimental Data for Burst Pressure 56.20 g/mm² and Sensor Position A at Sections 1 through 5 in 7.62 cm pipe.

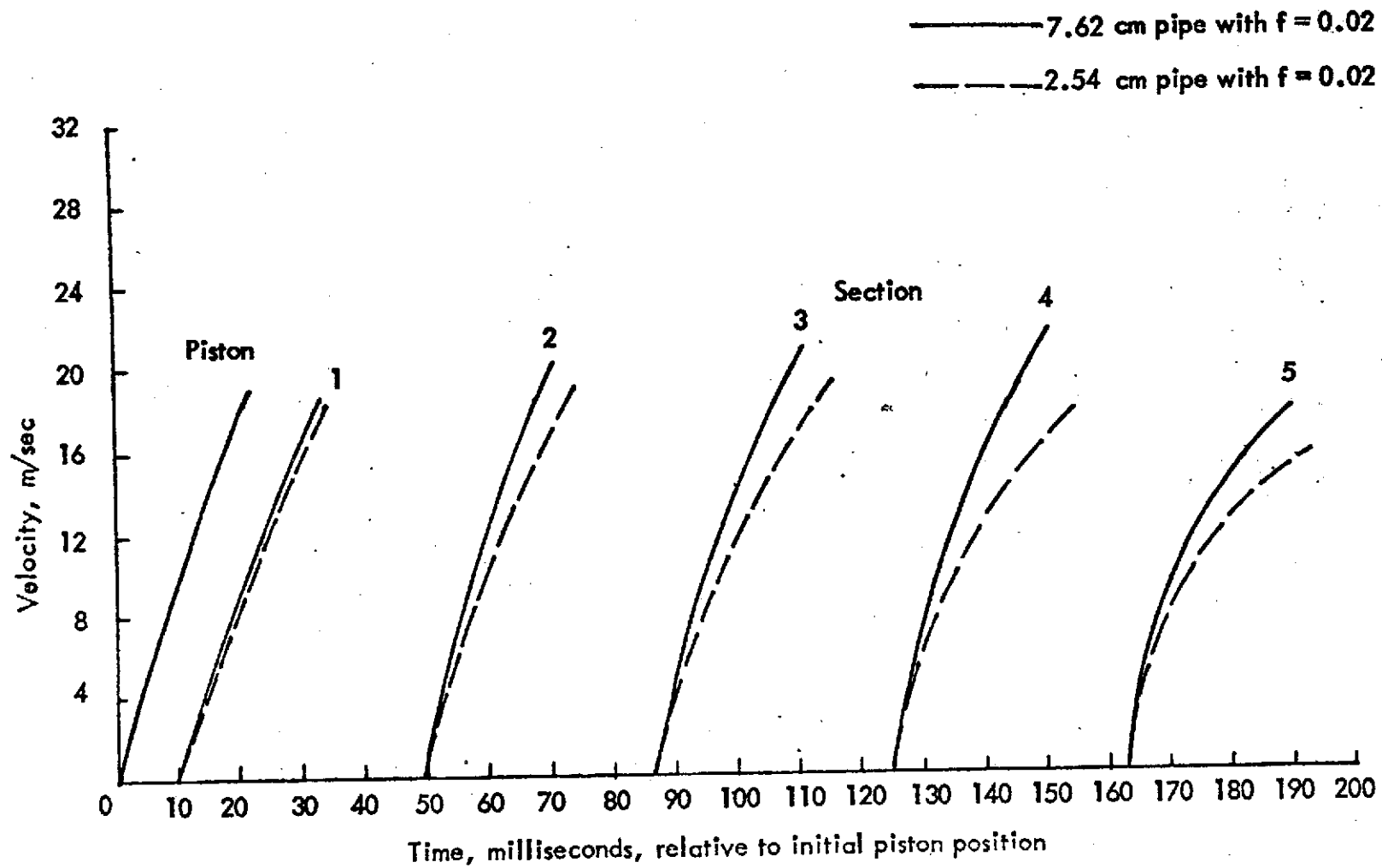


Fig. 6 Theoretical Comparison of Velocity Profiles Between 2.54 and 7.62 cm pipes with $f = 0.02$.

b1

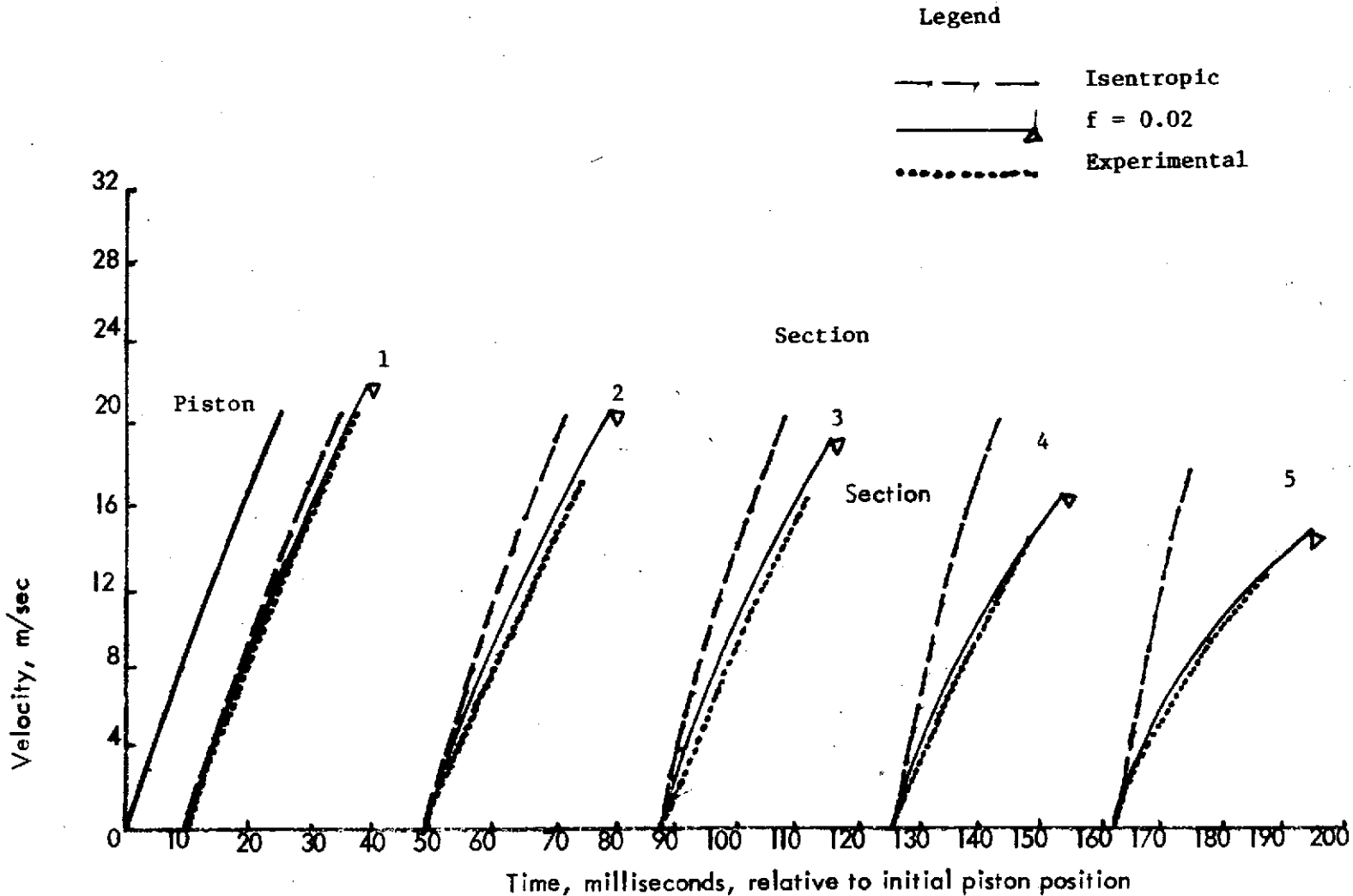


Fig.7 Comparison of Numerical Calculations with Experimental Data for Burst Pressure 28.10 g/mm² and Sensor Position A at Sections 1 through 5 in 2.54 cm pipe.

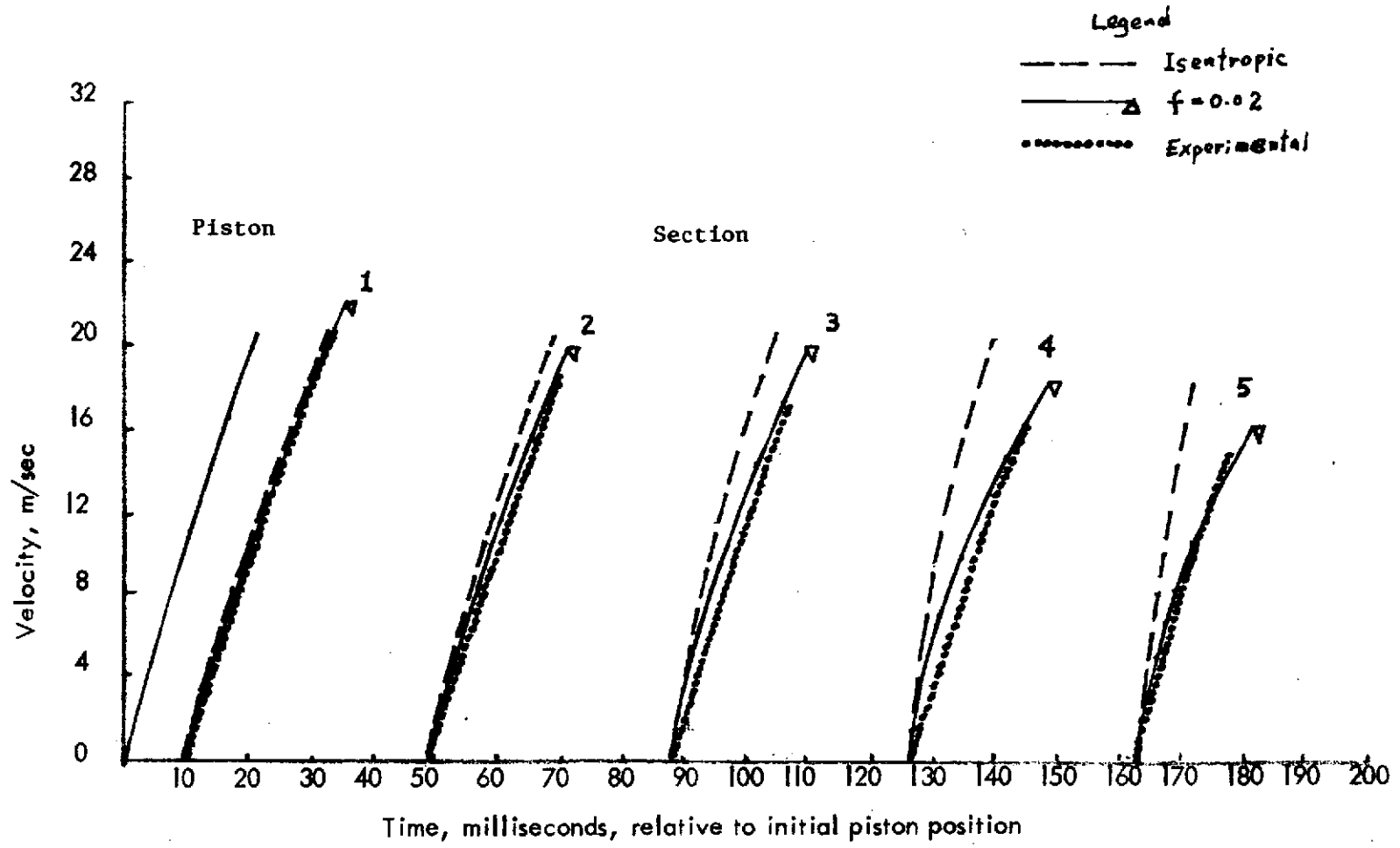


Fig. 8 Comparison of Numerical Calculations with Experimental Data for Burst Pressure 42.15 g/mm^2 and Sensor Position A at Sections 1 through 5 in 2.54 cm pipe.

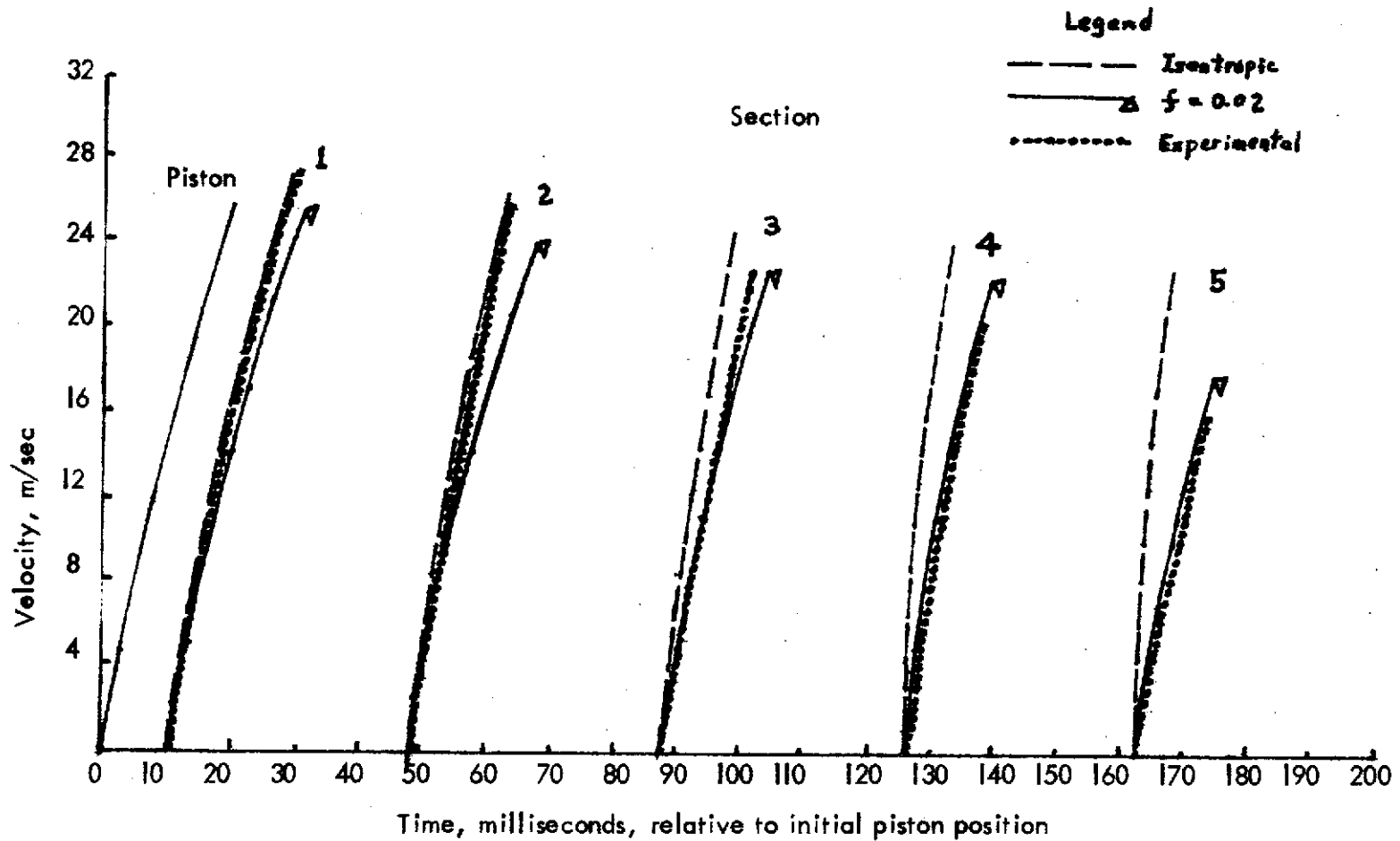


Fig. 9 Comparison of Numerical Calculations with Experimental Data for Burst Pressure 56.20 g/mm² and Sensor Position A at Sections 1 through 5 in 2.54 cm pipe.

APPENDIX A

```

DIMENSION V(101,101),A(101,101),VP(101),AP(101),X(101),T(101)
DT(101),TT(101,101),TP(101),XX(101,101)
READ(5,1000)GAMMA,P0,RH00,PL,ITMAX,N,C1,C2,C3,C4,C5,D1,D2,D3,D4,D5
C=P0/(RH00**GAMMA)
TEMP=SQRT(1.4*(RH00**0.4)*C)
N1=N+1
RN=N
DX=PL/RN
DT(2)=DX/TEMP
X(1)=0.0
T(1)=0.0
DO 10 K=1,ITMAX
DO 10 J=1,N1
V(J,K)=0.0
A(J,K)=TEMP
10 CONTINUE
DO 15 J=1,N1
VP(J)=0.0
TP(J)=0.0
AP(J)=TEMP
X(J)=(J-1)*DX
15 CONTINUE
K=1
RHO=RH00
WRITE(6,1005)K
WRITE(6,1010)T(1),RHO
WRITE(6,1015)(J,X(J),TP(J),VP(J),AP(J),J=1,N1)
CONST1=1.0/(GAMMA-1.0)
CONST2=(GAMMA-1.0)/4.0
DO 40 K=2,ITMAX
KM1=K-1
DO 20 J=1,N
XX(101,KM1)=X(101)
XX(J,KM1)=X(J)
TT(101,KM1)=TP(101)
TT(J,KM1)=TP(J)
V(J,KM1)=VP(J)
A(J,KM1)=AP(J)
20 CONTINUE
TF=T(K-1)+DT(2)
W=2.49*(TF*1000.)*0.922318
Y=0.2*(W-V(2,KM1))+A(2,KM1)
DDT=(X(1)-X(2))*2.0/(V(2,KM1)+W-A(2,KM1)-Y)
TS=T(K-1)+DDT
WW=2.49*(TS*1000.)*0.922318
YY=0.2*(WW-V(2,KM1))+A(2,KM1)
DDD=(X(1)-X(2))*2.0/(V(2,KM1)+WW-A(2,KM1)-YY)
T(K)=T(K-1)+DDD
VP(1)=2.49*(T(K)*1000.)*0.922318
AP(1)=0.2*(VP(1)-V(2,KM1))+A(2,KM1)
DO 30 JJ=2,N

```

```

JJM = JJ-1
JJP = JJ+1
CONST3=9.0*VISC*DT(JJ)/DIAM/DIAM
VISC=0.0
DIAM=0.08333
CONST4=2.0*CONST3+1.0
VP(JJ)=(0.5*(V(JJM,KM1)+V(JJP,KM1))+CONST1*(A(JJM,KM1)
+A(JJP,KM1)))/CONST4
AP(JJ)=CONST2*(V(JJM,KM1)-V(JJP,KM1)+
2.0*CONST1*(A(JJM,KM1)+A(JJP,KM1))) +
CONST2*CONST3*(V(JJP,KM1)-V(JJM,KM1))
Q=AP(JJ)*(TT(JJP,KM1)-TT(JJM,KM1))+2.0*(XX(JJP,KM1)-XX(JJM,KM1))
S=(TT(JJP,KM1)-TT(JJM,KM1))*(V(JJP,KM1)+VP(JJ)-A(JJP,KM1))
Z=2.0*AP(JJ)+(V(JJM,KM1)+V(JJP,KM1))*(A(JJM,KM1)+A(JJP,KM1))
DT(JJ)=(Q-S)/Z
TP(JJ)=TT(JJM,KM1)+DT(JJ)
DX=DT(JJ)*(V(JJM,KM1)+VP(JJ)+A(JJM,KM1)+AP(JJ))/2.0
X(JJ)=XX(JJM,KM1)+DX
TP(1)=T(K)
30 CONTINUE
TP(101)=TP(100)
WRITE(6,1005) K
WRITE(6,1010) T(K),RHO
WRITE(6,1006)
WRITE(6,1015) (J,X(J),TP(J),VP(J),AP(J),J=1,N1)
40 CONTINUE
1000 FORMAT(4F10.6,2I5/5E15.8/5E15.8)
1005 FORMAT(11FOR K =',I3/1H0,'T =',I9X,'RHO =')
1006 FORMAT(1H0,3X,'J',6X,'X(J)',10X,'TP(J)',10X,'VP(J)',10X,'AP(J)')
1010 FORMAT(1H+,4X,E15.8,9X,E15.8)
1015 FORMAT(1H ,14,4E15.8)
STOP
END

```

APPENDIX B

```

DIMENSION V(101,101),A(101,101),VP(101),AP(101),X(101),T(101)
,DT(101),TT(101,101),TP(101),XX(101,101)
READ(5,1000)GAMMA,PD,RHOO,PL,ITMAX,N,C1,C2,C3,C4,C5,D1,D2,D3,D4,D5
C=PD/(RHOO**GAMMA)
TEMP=SQRT(1.4*(RHOO**0.4)*C)
N1=N+1
RN=N
DX=PL/RN
DT(2)=DX/TEMP
X(1)=0.0
T(1)=0.0
DO 10 K=1,ITMAX
DO 10 J=1,N1
V(J,K) = 0.0
A(J,K) = TEMP
10 CONTINUE
DO 15 J=1,N1
VP(J) = 0.0
TP(J)=0.0
AP(J) = TEMP
X(J) = (J-1)*DX
15 CONTINUE
K=1
RHO = RHOO
WRITE (6,1005) K
WRITE (6,1010) T(1),RHO
WRITE (6,1015) (J,X(J),TP(J),VP(J),AP(J),J=1,N1)
CONST1 = 1.0/(GAMMA-1.0)
CONST2 = (GAMMA-1.0)/4.0
DO 40 K=2,ITMAX
KM1 = K-1
DO 20 J=1,N
XX(101,KM1)=X(101)
XX(J,KM1)=X(J)
TT(101,KM1)=TP(101)
TT(J,KM1)=TP(J)
V(J,KM1) = VP(J)
A(J,KM1) = AP(J)
20 CONTINUE
TF=T(K-1)+DT(2)
W=4.13*(TF*1000.)*0.87096774
Y=0.2*(W-V(2,KM1))+A(2,KM1)
DDT=(X(1)-X(2))*2.0/(V(2,KM1)+W-A(2,KM1)-Y)
TS=T(K-1)+DDT
WW=4.13*(TS*1000.)*0.87096774
YY=0.2*(WW-V(2,KM1))+A(2,KM1)
DDD=(X(1)-X(2))*2.0/(V(2,KM1)+WW-A(2,KM1)-YY)
T(K)=T(K-1)+DDD
VP(1)=4.13*(T(K)*1000.)*0.87096774
AP(1)=0.2*(VP(1)-V(2,KM1))+A(2,KM1)

```

```

DO 30 JJ=2,N
JJM = JJ-1
JJP = JJ+1
CONST3=FRIC*DT(JJ)/4.0/DIAM
FRIC=0.02
DIAM=0.25
CONST4=CONST3*(GAMMA-1.0)/2.0
VP(JJ)=0.5*(V(JJM,KM1)+V(JJP,KM1))+CONST1*(A(JJM,KM1)
.-A(JJP,KM1))
.-CONST3*(V(JJM,KM1)*ABS(V(JJM,KM1))+V(JJP,KM1)*ABS(V(JJP,KM1)))
AP(JJ)=CONST2*(V(JJM,KM1)-V(JJP,KM1)+
.2.0*CONST1*(A(JJM,KM1)+A(JJP,KM1))) +
.CONST4*(V(JJP,KM1)*ABS(V(JJP,KM1))-V(JJM,KM1)*ABS(V(JJM,KM1)))
Q=AP(JJ)*(TT(JJP,KM1)-TT(JJM,KM1))+2.0*(XX(JJP,KM1)*XX(JJM,KM1))
S=(TT(JJP,KM1)-TT(JJM,KM1))*(V(JJP,KM1)+VP(JJ)-A(JJP,KM1))
Z=2.0*AP(JJ)+(V(JJM,KM1)-V(JJP,KM1))*(A(JJM,KM1)+A(JJP,KM1))
DT(JJ)=(Q-S)/Z
TP(JJ)=TT(JJM,KM1)+DT(JJ)
DX=DT(JJ)*(V(JJM,KM1)+VP(JJ)+A(JJM,KM1)+AP(JJ))/2.0
X(JJ)=XX(JJM,KM1)+DX
TP(I)=T(K)
30 CONTINUE
TP(101)=TP(100)
WRITE(6,1005) K
WRITE(6,1010) T(K),RHO
WRITE(6,1006)
WRITE(6,1015) (J,X(J),TP(J),VP(J),AP(J),J=1,N1)
40 CONTINUE
1000 FORMAT(4F10.6,2I5/5E15.8/5E15.8)
1005 FORMAT('1FOR K =',I3/1H0,'T =',19X,'RHO =')
1006 FORMAT(1H0,3X,'J',6X,'X(J)',10X,'TP(J)',10X,'VP(J)',10X,'AP(J)')
1010 FORMAT(1H+,4X,E15.8,9X,E15.8)
1015 FORMAT(1H ,14.4E15.8)
STOP
END

```

SECTION II

EXPERIMENTAL INVESTIGATION OF THE UNSTEADY FORCES IMPOSED ON A SUBMERGED CIRCULAR CYLINDER IN ACCELERATING FLOW

TABLE OF CONTENTS

	Page
CHAPTER I. INTRODUCTION	1
A. Primary Objective	8
B. Specific Accomplishments	10
CHAPTER II. FORCE MEASUREMENT SYSTEM DESIGN	11
A. Balance Analytical Design	12
B. Mechanical Design of Balance and Model	17
C. Strain Gage Selection and Installation	20
D. Method of Force Determination	24
CHAPTER III. FLOW VISUALIZATION SYSTEM	27
CHAPTER IV. DATA REDUCTION SYSTEM.	32
A. System Components	32
B. Method of Filtering	35
CHAPTER V. EXPERIMENTAL RESULTS	40
A. Flow Parameters	41
B. Force Data	46
C. Comparison with Steady Flow Data	59
D. Flow Visualization Data	62
E. Discussion of Results	65

TABLE OF CONTENTS - Concluded

	Page
CHAPTER VI. CONCLUSIONS AND RECOMMENDATIONS	73
A. Conclusions	73
B. Recommendations	74
REFERENCES	76
APPENDIX A. THEORETICAL HYDRODYNAMIC MODEL	80
APPENDIX B. ENGINEERING DRAWINGS OF MODEL, BALANCE, AND MODEL ASSEMBLY	90
APPENDIX C. CALIBRATION PROCEDURE AND RESULTS	97
APPENDIX D. DATA REDUCTION SYSTEM COMPONENT DESCRIPTION	116
BIBLIOGRAPHY.	121

LIST OF ILLUSTRATIONS

Figure	Title	Page
I-1	Flow Field Surrounding Aerospace Vehicle Launch Complex	3
I-2	Overall View of Hydrodynamic Flow Facility	6
I-3	Dimensions of Hydrodynamic Flow Facility .	7
II-1	Amplification Factor and Phase Angle of Forced Second-Order System as a Function of Frequency Ratios and Damping Ratios . .	14
II-2	Model and Balance Installation	19
II-3	Schematic Diagrams for Wiring Wheatstone Bridges -- Four-Arm Active, Two-Moment System	21
II-4	Location of Strain Gages, Typical of All Surfaces of Balance Section	22
II-5	Photograph of Finished Strain Gage Balance .	23
II-6	Cantilevered Beam with Two Strain Gage Bridges	24
III-1	Schematic Diagram of Improved Flow Visualization System	31
IV-1	Schematic Diagram of Data Reduction System	34
IV-2	Frequency Response of Fast Fourier Transform Simulated Low Pass Filter, FC = 20 Hertz	36

LIST OF ILLUSTRATIONS - Continued

Figure	Title	Page
IV-3	Unfiltered and Filtered Lift Channel Output .	37
IV-4	Unfiltered and Filtered Drag Channel Output .	38
V-1	Typical Flow Parameters for an Area Ratio 1.0 Test	44
V-2	Fluid Acceleration and Fluid Velocity as a Function of Time for a Typical Area Ratio 1.4 Test	45
V-3	Flow Parameters for a Typical Area Ratio 1.4 Test	47
V-4	Total Lift Force as a Function of Nondimen- sional Fluid Displacement, S/D, for a Typical Area Ratio 1.0 Test	48
V-5	Total Drag Force as a Function of Nondimen- sional Fluid Displacement, S/D, for a Typical Area Ratio 1.0 Test	49
V-6	Lift and Drag Coefficients as a Function of Time for a Typical Area Ratio 1.0 Test . .	51
V-7	Lift and Drag Coefficients as a Function of Nondimensional Fluid Displacement, S/D, for a Typical Area Ratio 1.0 Test	52
V-8	Plot of Lift and Drag Coefficients as a Function of Instantaneous Reynolds Number for Typical Area Ratio 1.0 Tests	53
V-9	Total Lift Force as a Function of Nondimen- sional Fluid Displacement, S/D, for a Typical Area Ratio 1.4 Test	55
V-10	Total Drag Force as a Function of Nondimen- sional Fluid Displacement, S/D, for an Area Ratio 1.4 Test	56

LIST OF ILLUSTRATIONS - Continued

Figure	Title	Page
V-11	Plot of Lift and Drag Coefficients as a Function of Instantaneous Reynolds Number for Area Ratio 1.4 Tests	57
V-12	Effects of Low Pass Filter Cutoff Frequency on Drag Coefficient for an Area 1.0 Test	58
V-13	Comparison of the Effects of Nondimensionalizing Factors on Drag Coefficient for an Area 1.0 Test	60
V-14	Comparison of Sectional Drag Coefficients Obtained for Time-Dependent and Steady Flows	61
V-15	Photographs of Flow Fields Surrounding a Right-Circular Cylinder Submerged in a 1-g Accelerating Flow	63
V-16	Photographs of Flow Fields Surrounding a Right-Circular Cylinder During a Typical Area Ratio 8.35 Test Run	64
A-1	Coordinate Systems for Theoretical Hydrodynamic Model	89
B-1	Engineering Drawing of Model Assembly	91
B-2	Engineering Drawing of Balance Section	92
B-3	Engineering Drawing of Model Section Number One	93
B-4	Engineering Drawing of Model Section Number Two	94
B-5	Engineering Drawing of Model Section Number Three	95
B-6	Engineering Drawing of Support Balance Receptacle	96

LIST OF ILLUSTRATIONS - Concluded

Figure	Title	Page
C-1	Cantilevered Beam with Two Strain Gage Bridges (A and F)	98
C-2	System Output as a Function of Dead Weight Load	101
C-3	Unit System Output as a Function of Load Station	102
C-4	Unit System Output as a Function of Load Station -- Drag Plane	104
C-5	Unit System Output as a Function of Load Station -- Lift Plane	105
C-6	Drag Plane Static Calibration Results	106
C-7	Lift Plane Static Calibration Results	110
C-8	Drag Plane Output for Static Calibration Loading in the Lift Plane	114
D-1	Schematic Diagram of Strain Gage Bridge Circuit	120

LIST OF SYMBOLS

A	Fluid acceleration
A_1	Test section cross-sectional area
A_2	Exit cross-sectional area
C	Dynamic system damping coefficient
C_c	Dynamic system critical damping coefficient
C_d	Instantaneous sectional drag coefficient
C_d'	Sectional drag coefficient, conventional nondimensionalizing
C_l	Instantaneous sectional lift coefficient
D	Model diameter
g	Gravitational acceleration
ΔH	Distance between adjacent static pressure pickups
L	Model length (exposed)
M_1	Bending moment at aft gage station
M_2	Bending moment at forward gage station
N	Normal force
P	Forcing function's frequency
P_N	Dynamic system natural frequency
ΔP	Static pressure differential

R_N	Reynolds number, $R_N = \frac{\rho_0 V D}{\mu}$
$R(t)$	Instantaneous Reynolds number, $R(t) = \frac{\rho_0 V(t) D}{\mu}$
S	Fluid displacement
S/D	Nondimensional fluid displacement
t	Time from flow initiation
V	Fluid velocity
X	Distance between bridge stations
ρ_0	Fluid density
μ	Fluid viscosity

CHAPTER I

INTRODUCTION

Rocket technology's rapid development in the decade following the launching of the earth's first artificial satellite brought several unsteady fluid flow¹ problems to the attention of the aerospace engineering community. One area which received attention was the prediction of the response of flexible, slender bodies to loads imposed by ground winds. This was not a new problem, but one with which civil engineers had grappled for years in the design of smoke stacks, suspension bridges, and tall masts. The aerospace engineer found this problem to be somewhat more complex than the civil engineer had determined it. The civil engineer usually could make allowances for the uncertainty of his design loads by increasing the strength of the structure. The same procedure, when followed by the aerospace engineer, usually resulted in space vehicles with less than the desired capability. Alternate solutions were either to design space vehicles with limited regard to the problem or to test aeroelastic

¹Unsteady fluid flow is defined as a flow in which the freestream velocity is time-dependent in an Eulerian reference frame.

models of the complex structures to obtain structural responses for particular space vehicles in question.

None of these solutions were entirely acceptable to the aerospace engineers, as indicated by the conferences (Refs. 1 through 3)² held on this subject. One such meeting sponsored by the National Aeronautics and Space Administration (NASA) in June 1966 focused attention on two aspects of this problem.

These aspects were: (1) the definition of the atmospheric environments surrounding the launch complex and (2) the relationship between the atmospheric environment and the pressures, forces, and moments imposed on the space vehicle. These two aspects together with a third, the determination of the response of the body once the forcing functions acting on the body are known, make up the ground winds problem. The second aspect is the one of interest to the fluid dynamicist. The flow field surrounding the launch complex and the structural loading conditions arising from low-level (altitude $\leq 2,000$ feet) atmospheric movements are illustrated in Figure I-1.

Both steady and oscillatory forces are induced on the space vehicle by the steady-state ground wind shown in profile. The steady force which acts in the direction of the steady wind is

²References are located at the end of the main text.

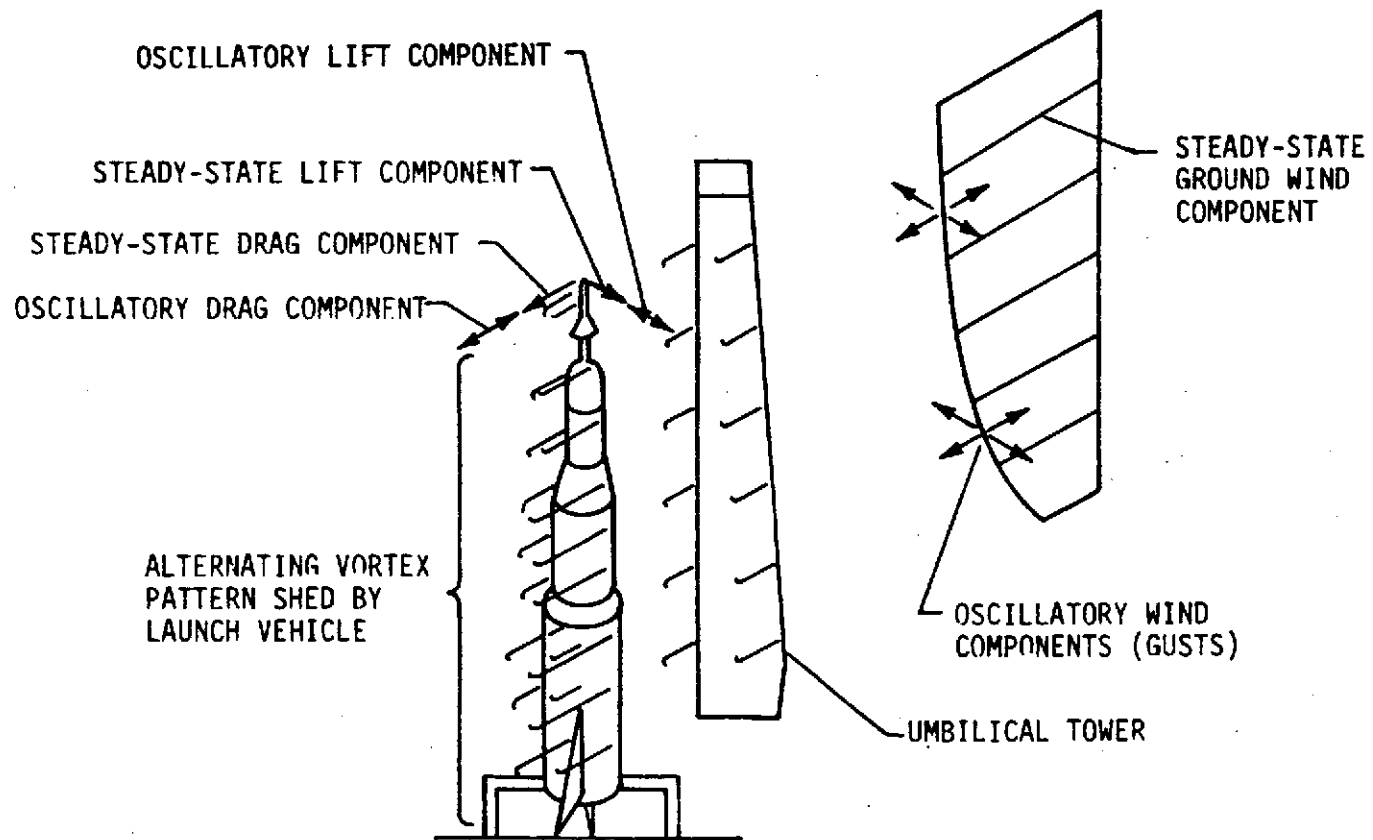


FIGURE I-1. FLOW FIELD SURROUNDING AEROSPACE VEHICLE LAUNCH COMPLEX

referred to as drag. A force perpendicular to the direction of the steady wind is referred to as lift. The oscillatory force, with components both in and perpendicular to the direction of the steady wind, results from a flow phenomenon which occurs over a wide range of Reynolds number for flow about a bluff body; i. e., the space vehicle. This flow phenomenon is the alternate shedding of vortices from the two sides of the space vehicle. This shedding creates an unequal pressure distribution over the vehicle and, hence, oscillatory loads are induced on the space vehicle as the alternate vortex shedding occurs. Flow deflection caused by the umbilical tower, impingement of its turbulent wake, or asymmetries on the vehicle can add a component to the oscillatory forces. Additional components may be induced by atmospheric turbulence or gusts.

The NASA-sponsored meeting (Ref. 1) recommended basic research into the unsteady flow phenomenon to establish theories for better predicting the time-dependent development of the flow field surrounding the launch complex. In response to this recommendation, the Fluid Dynamics Laboratory of the University of Alabama in Huntsville initiated a series of investigations into this complex flow phenomenon. The first research efforts were to establish the time-dependent flow field around a rigid, right-circular cylinder submerged in an unsteady flow.

Investigation revealed that for the velocities of interest ($V_{\infty} < 100$ ft/sec) the Mach number was low where compressibility effects are negligibly small and the dynamic similarity between the phenomenon with air and water would justify the use of water as the medium for the study. After this determination, the initial effort consisted of the design, construction, and calibration of an experimental hydrodynamic flow facility which could be used to achieve the desired unsteady flow.

The facility, shown in Figure I-2, consisted of a water tunnel equipped with a quick-start mechanism and instrumentation systems for the determination of pressure, both on the tunnel walls and on the model surface. The water tunnel is a vertically erected steel tank 21.13 feet long and 2.83 feet in diameter. Two walls running the entire tank length help to provide two-dimensional flow but, at the same time, reduce the useful test section width to 1.92 feet. Plexiglass windows set into the walls allow the model ends to be built in to reduce undesirable end effects. The flow visualization system also made use of these windows. Location of the test section, together with the dimensions of the various items, are illustrated in Figure I-3.

Quick start of the flow is achieved by thermally rupturing a mylar diaphragm located at the lower tank end. At the test section, water flows having acceleration levels of up to 32.17 ft/sec² can be

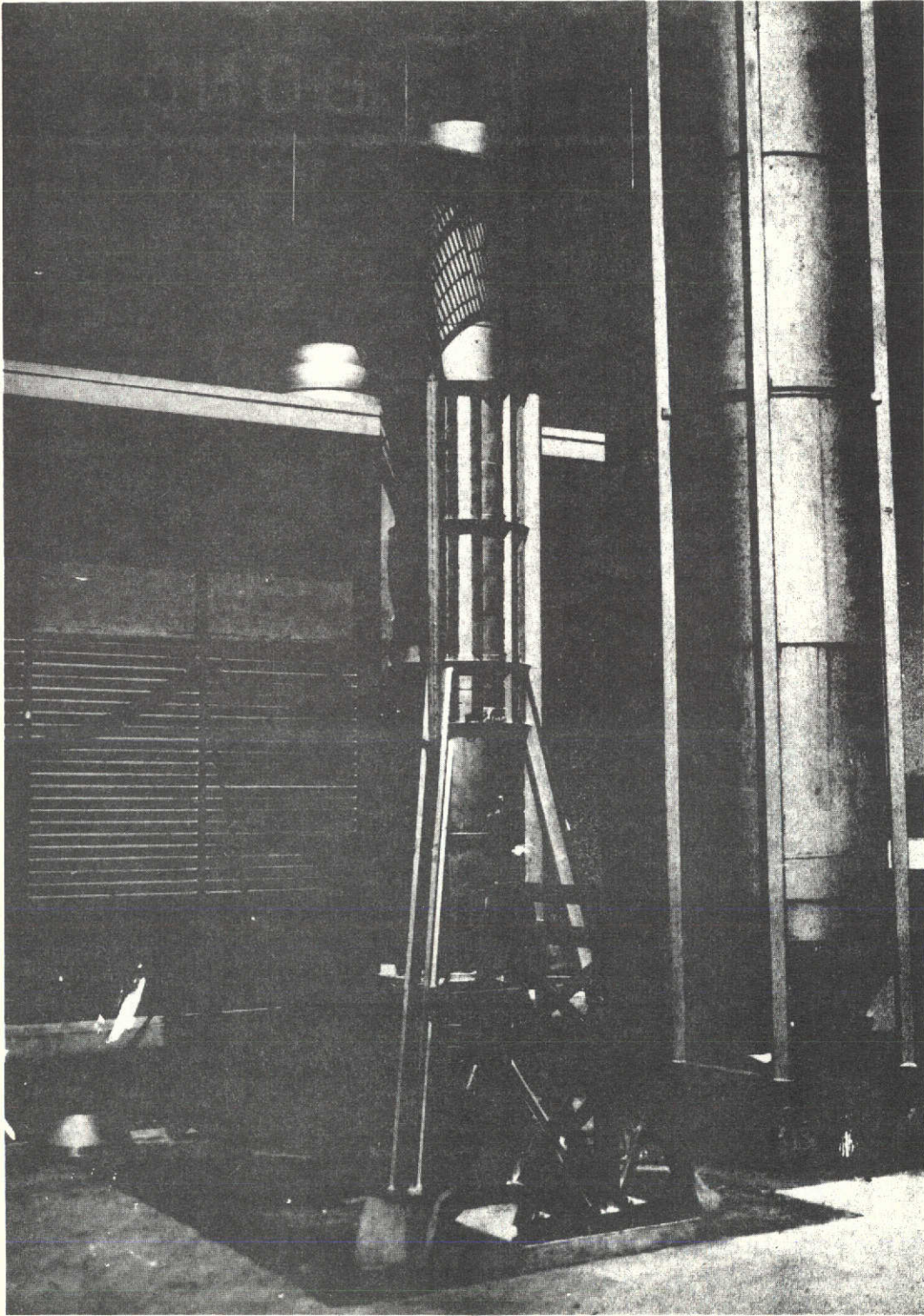


FIGURE I-2. OVERALL VIEW OF HYDRODYNAMIC FLOW FACILITY

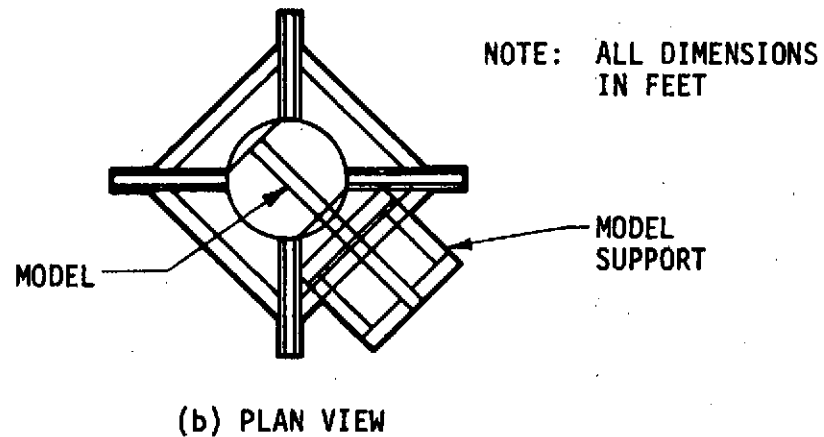
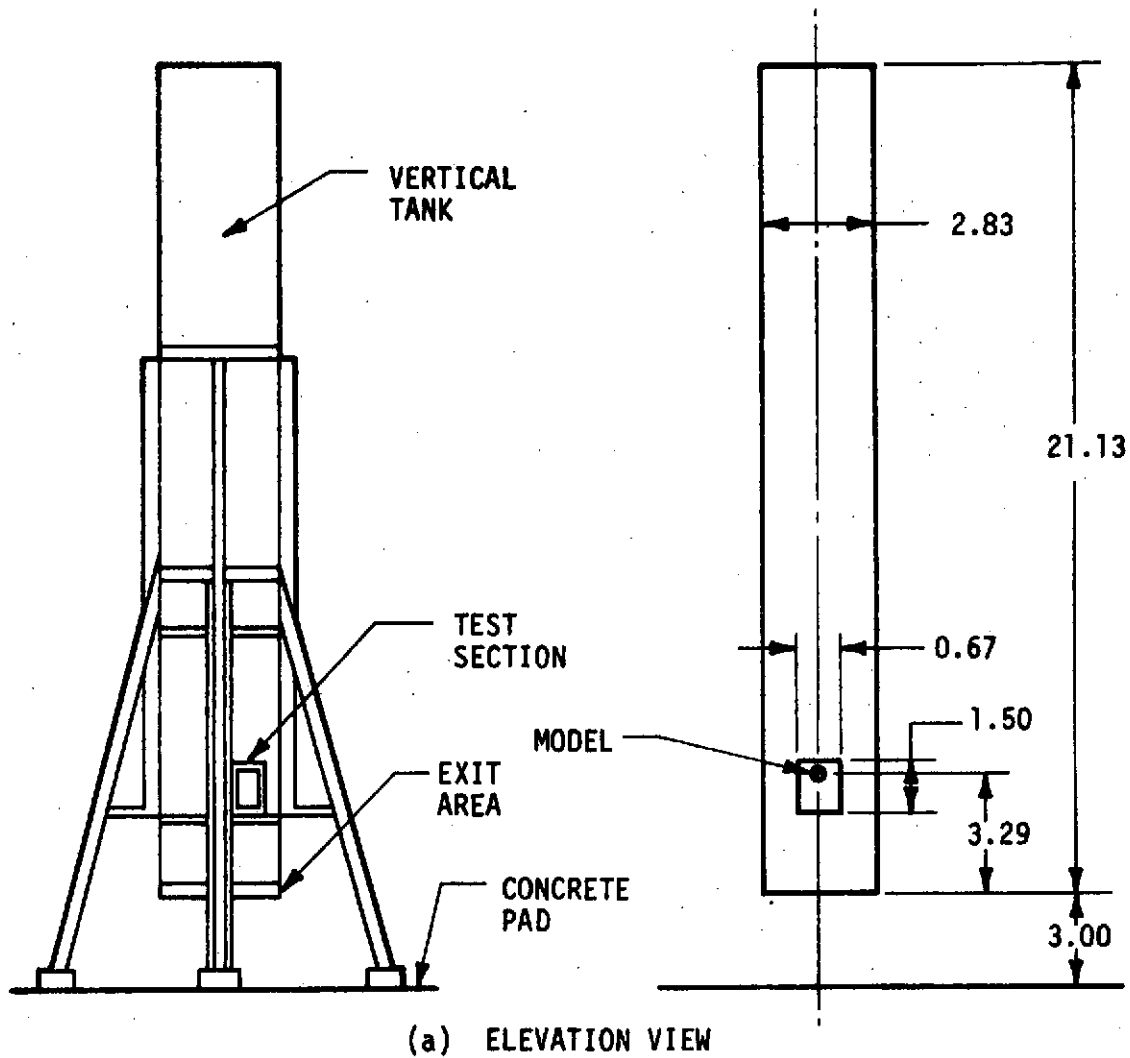


FIGURE I-3. DIMENSIONS OF HYDRODYNAMIC FLOW FACILITY

produced by varying the opening area of the mylar diaphragm. Operating characteristics of the facility, together with complete details of its development and operation, can be found in Reference 4.

The initial research conducted using this facility consisted of the measurement of the time-dependent pressure at various locations on the surface of a 3.0-inch diameter cylindrical model. High-speed photography was used in the study of the time-dependent flow field surrounding the model. A complete discussion of this initial research can be found in Schutzenhofer's thesis, Reference 4.

A. Primary Objective

The primary objective of this study was an experimental investigation of the unsteady forces imposed on a right-circular cylinder immersed in a time-dependent flow. To accomplish this objective, it was first necessary to design a system capable of measuring the unsteady forces.

The initial phase in the system design consisted of a survey of the available literature to determine the nature (i. e., the frequency and magnitude) of the unsteady forces. The results of this survey are presented in the Bibliography. The amount of experimental research previously conducted on the unsteady forces imposed on a cylindrical model immersed in a time-dependent flow was found to be somewhat limited. However, the works of

Schutzenhofer (Ref. 4), Sarpkaya (Ref. 5), Pearce (Ref. 6), Jones, et al (Ref. 7), Bishop and Hassen (Ref. 8), and Keefe (Ref. 9) were most helpful in understanding the phenomena of the unsteady forces associated with flows around bluff bodies.

The attempts to develop a mathematical model of the flow phenomena created by time-dependent flows about bluff bodies, of which the cylinder is the simplest, have been numerous. The classical mathematical approach to this problem was developed by von Karman (Ref. 10), and perhaps is still the most significant. Others who have formulated mathematical models include Sarpkaya (Ref. 11), Phillips (Ref. 12), and Gerrard (Ref. 13). However, because of the complex mathematics associated with this problem, a formulation which yields results acceptable for general engineering use has not been made available to the author's knowledge.

One important question remained unanswered after completion of the literature survey: To what degree of accuracy can the forces be predicted by two-dimensional inviscid theory? To answer this question, the author developed a two-dimensional inviscid mathematical model which includes the blockage effects. The derivation of this model is presented in Appendix A and results obtained from the model are discussed in Chapter V.

B. Specific Accomplishments

The specific accomplishments of this study are:

- (1) Experimental measurement of integrated unsteady forces acting on a rigid, right-circular cylinder submerged in an accelerating flow
- (2) The design of a simple system that can measure the unsteady forces
- (3) Development of a digital data reduction system
- (4) Improvement of the flow visualization system
- (5) Analysis of 16-millimeter movie films of the unsteady flow phenomena around a circular cylinder for various time-dependent flow conditions.

CHAPTER II

FORCE MEASUREMENT SYSTEM DESIGN

The limited experimental data regarding unsteady forces on bluff bodies in time-dependent flows left unresolved several important questions concerning the nature of the unsteady forces. These questions were:

- (1) Does the sudden decrease in cylinder drag coefficient which occurs at about a Reynolds number¹ of 5×10^5 in steady flow occur in time-dependent flows?
- (2) Is the magnitude of the unsteady forces a function of flow acceleration level as predicted by inviscid two-dimensional theory?
- (3) Is there a spanwise correlation associated with the formation of the vortices at the rear of the cylinder?

These questions led to the decision to design a system capable of measuring the total unsteady forces induced on a cylindrical model which spanned the entire width (1.92 feet) of the facility test section. This system would measure the integrated effects of the unsteady

¹Based on cylinder diameter, $R_N = \rho_0 VD/\mu$

forces acting on the total length of the model. These integrated forces could then be used to obtain a spatial average of the unsteady lift and drag forces as a function of time.

A. Balance Analytical Design

Several methods of achieving the objective of unsteady force measurement were investigated and found feasible. These varied from a simple system employing stiff beams in conjunction with either load cells or strain gages to a highly complex and expensive system utilizing an Inertially Compensated Balance² (ICB). From the standpoints of simplicity and cost, a system employing a two-component strain-gaged beam as the measuring element or balance is the most advantageous. The principal disadvantage with this type of system, however, is the amplification factor associated with the response of the physical system to a dynamic excitation. The amplification factor is defined as the ratio of system output to forcing function input.

Assumptions were made that for the range of the design forces³, the force measurement system could be designed to have a linear response with small displacements. The characteristics of

² For a discussion of the ICB, see References 7 and 14.

³ The design forces were: lift plane ± 100 pounds, drag plane +400 pounds.

highly complex systems with small displacements and linear responses may be approximated for analytical purposes by combinations of second-order linear differential equations with constant coefficients. Each of these differential equations is assumed to represent the equation of motion of a single degree-of-freedom system defined by a natural mode of vibration with a frequency, P_n . Details of this technique can be found in References 15 and 16. The employment of this analysis technique allows the system to be analyzed as separate combinations of independent single degree-of-freedom systems in both the lift and drag planes. The advantage in using this type of analysis is that the inertial forces for those modes whose natural frequency is well above the forcing frequency are assumed to be small and therefore can be neglected.

The amplification factor and the phase angle⁴ for single degree-of-freedom systems are functions of two ratios:

- (1) Ratio of the frequency of forcing function to the system's undamped natural frequency
- (2) Ratio of the damping present in the system to the critical damping value for the system.

An examination of Figure II-1 shows that for low frequency ratios ($P/P_n \leq 0.2$) and low damping ratios ($C/C_c \leq 0.05$) the amplification

⁴Phase angle is defined as the angle between the line of action of the forcing function and the system displacement.

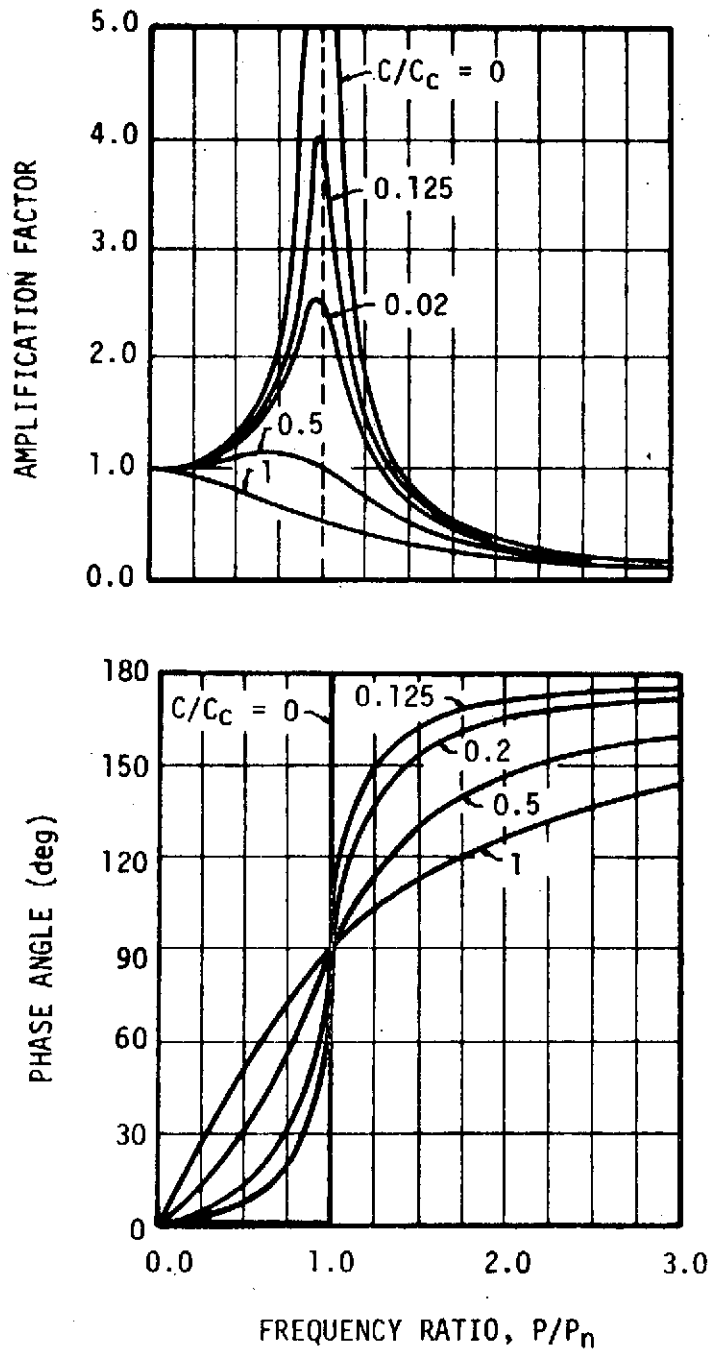


FIGURE II-1. AMPLIFICATION FACTOR AND PHASE ANGLE OF FORCED SECOND-ORDER SYSTEM AS A FUNCTION OF FREQUENCY RATIOS AND DAMPING RATIOS

factor and the phase angle are approximately 1.0 and 0 degrees, respectively. A system with these characteristics would follow the forcing function very closely.

It would appear that the best force measuring system would be the one with the highest natural frequency and the least system damping. This is not the case for a system employing a strain-gaged beam as the sensing element because the strain of the element is an inverse function of the system's natural frequency squared. For this reason, the problem of design becomes one of obtaining the highest system natural frequency while maintaining an acceptable strain for the minimum loads which the system is expected to measure. This particular design problem is further complicated by the fact that because the model is immersed in a time-dependent flow, there is an additional mass of fluid referred to as added mass acting with the model as though it were attached to the model. This added mass in theory is a function of the model diameter, the test section size, and the acceleration level of the fluid (see Appendix A). In determining the dynamic response to a physical system, this added mass must be combined with the mass of the system. This combined mass is usually referred to as the virtual mass of the system. It has been shown by Jones (Ref. 17) that the first few natural frequencies of a beam immersed in a fluid can be predicted numerically by conventional methods to within 10-percent accuracy if the virtual

mass is used in the analysis. Jones also noted that the mode shapes associated with these frequencies were not affected by either the density or viscosity of the fluid. Since the frequencies of the final design were to be determined experimentally, this degree of accuracy was considered sufficient for design purposes.

Because the magnitude of the added mass quantity is a function of acceleration level of the fluid, the force measurement system was designed considering the maximum acceleration level which the facility could provide; i. e., 32.17 ft/sec^2 .

The use of a 3-inch diameter model limited the cross-sectional area available for the balance section, thus limiting the stiffness of the balance section. This also had a pronounced effect on the frequency-strain relationship of the balance section. The method of force determination from the strain gage output which had been chosen (see Section D) depends upon having two strain gage bridges in each plane located several inches apart. With the area limitation, the distance between the gage locations became an important parameter in establishing the magnitude of the natural frequencies of the system.

The various parameters outlined so complicated the problem of designing the system that it was necessary to consider the balance and model as a combined cantilevered beam. The effects of variations in the kinds of materials, the balance section length, and the

distribution of cross-sectional area along the length of the combined cantilevered beam on the system's natural frequencies were evaluated using an existing digital computer program (Ref. 18). A conjugate beam analysis of the combined cantilevered beam using the maximum anticipated load distributed uniformly was performed to determine the ranges of bending stiffnesses required to limit the beam's free end static deflection to 0.05 inch. This range of stiffnesses was then used in determining the initial values of the computerized parametric analyses.

The results of the parametric analyses indicated that to achieve the high frequency desired (~ 200 hertz), it would be necessary to have a rigid support for the measurement system separate from the vertical tank. Additionally, these results indicated that a built-up beam of stainless steel and aluminum would give the desired frequency while keeping the free end deflection within the limits established.

B. Mechanical Design of Balance and Model

The final design of the balance consisted of a symmetric section of stainless steel with a constant cross-sectional area of 1.71 in^2 for a length of 3 inches. Matching tapered ends, prevented from twisting by two $1/4$ -inch-diameter pins and drawn together by a $3/8$ -inch-diameter bolt, were used to join the balance section to the support structure and to the model.

The model final design consisted of three constant cross-sectional area sections (two of stainless steel, one of aluminum), fastened together by four 1/4-inch-diameter dowel pins and a minimum of 1 inch of Number 32NF threads at each joint. Total weight of the model assembly was 10.80 pounds. Engineering drawings of each component and the model assembly are presented in Appendix B.

An installation drawing showing the methods of sealing around the model is presented in Figure II-2. The free end of the model was allowed to "float" inside a 3.12-inch-diameter cutout in the plexiglass window. The model extended 0.25 inch into the window with a clearance of 0.12 inch allowed between the end of the model and the window. At the fixed end of the model, one wrap of 1/2-inch-wide flexible cellophane tape was used to seal the gap between the end of the model and the adapter section fixed to the facility wall. This adapter section extended 0.47 inch from the wall so that a gap of 0.03 inch existed between the model and adapter section.

The effects of this method of sealing were investigated during calibration and no measurable difference between the sealed and unsealed cases could be determined for the static loading. Also, no effects of sealing were measurable when the frequency check was made.

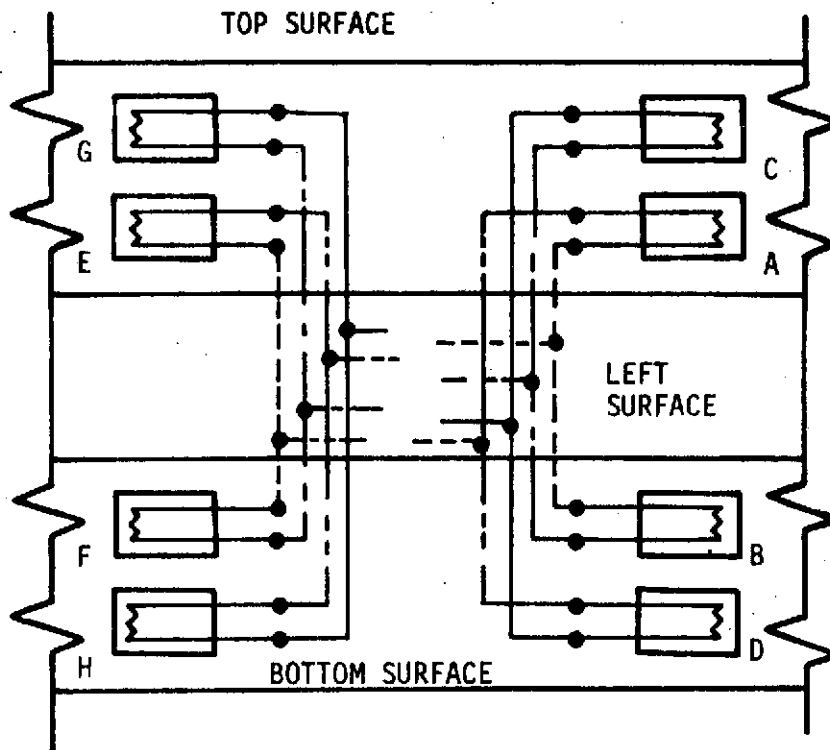
C. Strain Gage Selection and Installation

The final design of the balance section was based upon the use of the BLH Electronics Metal Foil Strain Gage, Number DLB-PT-12-2A, in a four-arm active Wheatstone Bridge. These gages, made of platinum alloy on a phenolic-glass carrier, were found to be most satisfactory considering four major factors:

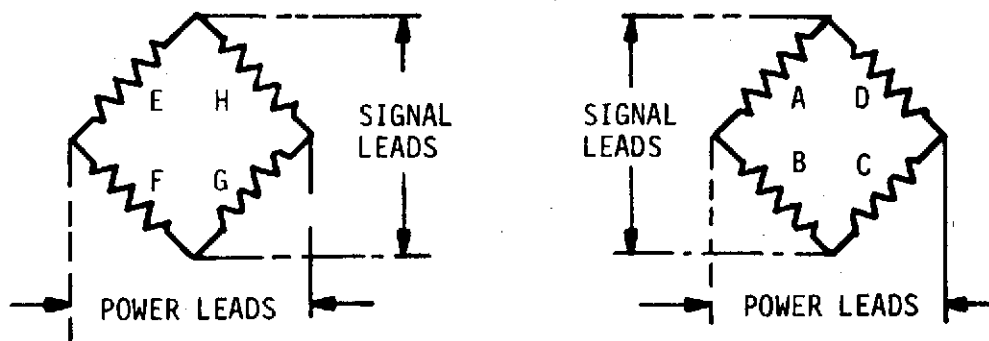
- (1) Gage factor
- (2) Cost
- (3) Suitability for dynamic strain measurement
- (4) Ease of installation

Installation of 16 of these gages wired in four (two lift, two drag) four-arm active Wheatstone Bridge circuits was accomplished according to Figures II-3 and II-4 using Micro-Measurements M-Bond 610 epoxy adhesive. Waterproofing of the gage installation was accomplished using BLH Barrier E Waterproofing. Figure II-5 is a photograph of the waterproof balance section after the attachment of a waterproof connector to the leads of the four Wheatstone Bridge circuits.

The four-arm active Wheatstone Bridge was selected because of its excellent temperature compensation effects and because it provided the maximum electrical output for the same strain level. In addition, the fully active bridge has greater accuracy and stability than other types of bridges (Ref. 18).



(a) DISTORTED (UNWRAPPED) VIEW, WIRING FOR SIDE-BY-SIDE GAGES



(b) SCHEMATIC CONNECTION DIAGRAMS

NOTE: WIRING DIAGRAMS FOR LEFT AND RIGHT SURFACES IDENTICAL TO THOSE FOR TOP AND BOTTOM SURFACES

FIGURE II-3. SCHEMATIC DIAGRAMS FOR WIRING WHEATSTONE BRIDGES -- FOUR-ARM ACTIVE, TWO-MOMENT SYSTEM

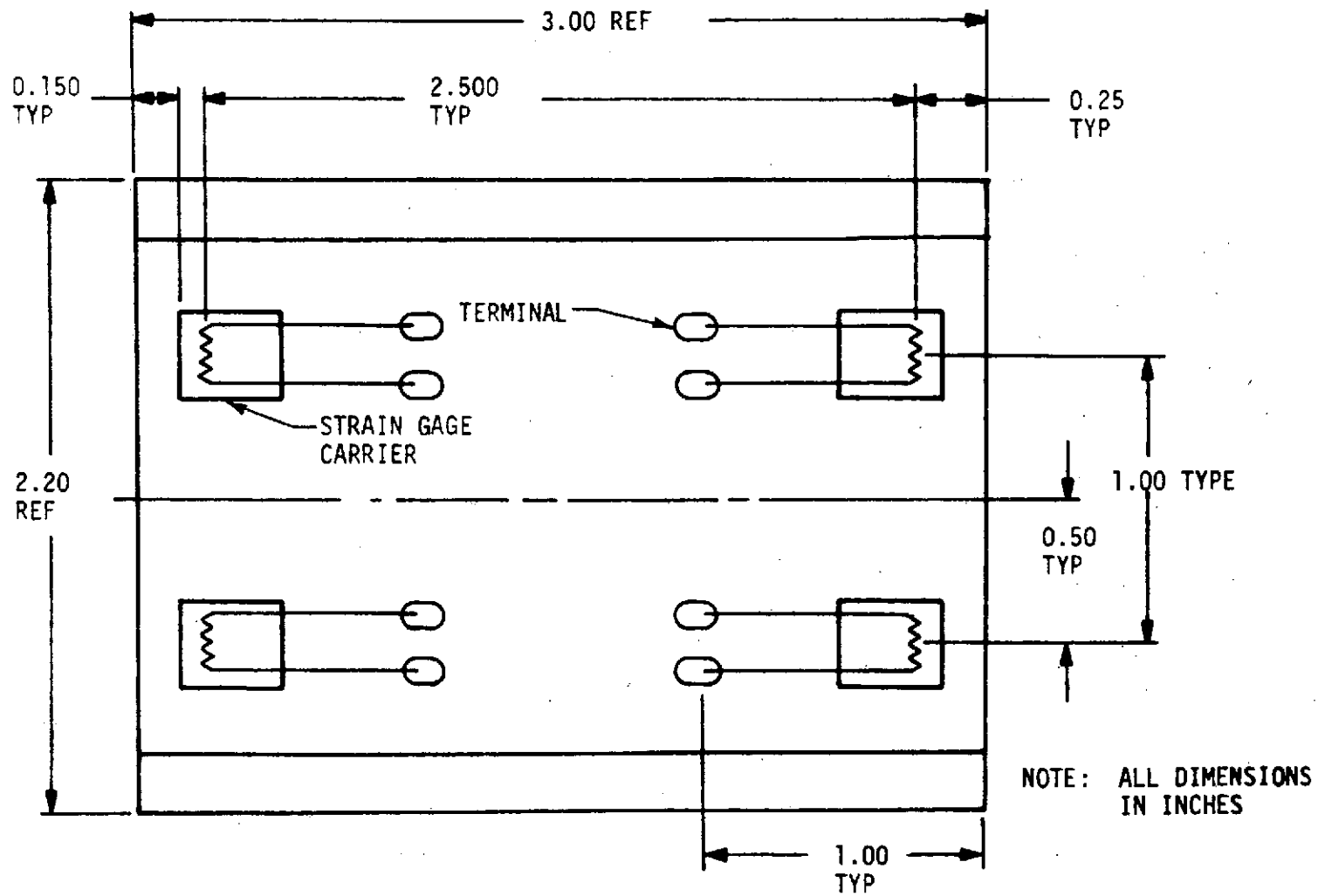


FIGURE II-4. LOCATION OF STRAIN GAGES, TYPICAL OF ALL SURFACES OF BALANCE SECTION



FIGURE II-5. PHOTOGRAPH OF FINISHED STRAIN GAGE BALANCE

D. Method of Force Determination

Three methods of force determination from Wheatstone

Bridge output were investigated. These are:

- (1) Basic two-moment system
- (2) Direct force determination
- (3) Composite bridge.

Each of these methods has its advantages; however, the basic two-moment method is more suited to high-speed, digital data processing.

A detailed discussion of the relative merits of each system may be found in Reference 19.

In the two-moment method, two strain gage bridges are located on a cantilevered beam some distance apart, as shown in Figure II-6.

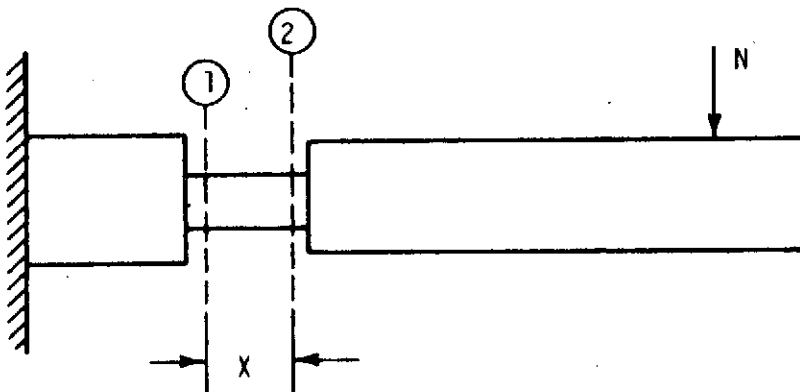


FIGURE II-6. CANTILEVERED BEAM WITH TWO STRAIN GAGE BRIDGES

These bridges determine the beam bending moment at their relative locations. It is apparent that the normal force, N, is given by

$$N = \frac{M1 - M2}{X}$$

where

- M1 - beam bending moment at location 1
- M2 - beam bending moment at location 2
- X - distance between bridge locations.

Thus, if calibration constants can be determined which convert the electrical output of the Wheatstone Bridges into bending moments and the distance between bridges is known, the amount of force acting on the beam can be determined. The outlined procedure is applicable to both the lift and drag planes when the normal force, N, is given the appropriate definition.

Initially, both static and dynamic calibration of the force measuring system was planned; however, the lack of suitable calibrated test equipment for applying known magnitudes of dynamic loads at specific frequencies led to the elimination of the dynamic portion of the calibration. The results of an experimental frequency determination indicate that the design goal of a high first-mode natural frequency was achieved. The experimental value for the

first natural-mode frequency was found to be between 168 and 172 hertz. This frequency was independent of the height of the water in the facility.

Static calibration revealed that design goals of system linearity and independency of the lift and drag planes were achieved. Details of the procedure used to calibrate the force measuring system and calibration results are presented in Appendix C.

CHAPTER III

FLOW VISUALIZATION SYSTEM

One of the objectives of this project was the improvement of an existing flow visualization system. This existing system used bubbles formed when compressed air was released from hypodermic needles connected to a plenum chamber. These spherical bubbles were photographed by high-speed cameras during the test runs.

The problem with this system was that no combination of needle orifice size and plenum operating pressures was found which would produce a sufficient supply of small bubbles with approximately uniform diameter. High-speed photography and this technique had been employed to obtain some motion pictures of the flow phenomena, but improvement in both the number and size of the bubbles was desired (Ref. 4).

Investigation of the hydrogen bubble technique revealed that a unique application of this procedure might produce the desired improvement. The standard hydrogen bubble technique uses electrolysis of water to produce hydrogen and oxygen bubbles (Ref. 20). A thin platinum wire is used as the cathode and the small hydrogen bubbles produced on it are swept away in the passing flow where they

are assumed to represent fluid particles in the flow downstream. The analyses of this standard technique revealed two problems associated with it when used in conjunction with the unsteady flow facility. One was the flow disturbance which would be created in front of the model by the platinum wire and the other, was the cost associated with the wire itself. A known fact is that in steady flow the location of flow separation on a circular cylinder is highly dependent on the amount of free-stream turbulence in the flow. Thus, the very presence of the wire upstream of the model might change the thing being studied; i. e., the flow field around the cylinder.

The cost of the approximately 3-foot length of aluminum wire required to span the facility was prohibitive since the wire section probably would be destroyed during each test. The estimated cost of replacing the platinum wire after each test exceeded the allotted funds for this particular aspect of the study. Therefore, if the hydrogen bubble technique was to be incorporated into the flow visualization system, the two above mentioned problems would have to be solved.

Experimentation with various kinds and diameters of wires revealed that a large number of small hydrogen bubbles could be produced using a 0.0025-inch diameter music wire as the cathode. The number and size of the bubbles produced using straight music wire was found to be dependent on the level of electrical current and

voltage used. The current and dc voltage levels at which the largest number of the most uniform appearing bubbles could be produced using the straight 0.0025-inch-diameter music wire was found to be 4.8 amperes of current and 280.0 volts of dc voltage.

The problem of the turbulence created by the wire as the flow passed was solved by moving the music wire below the model. In this application, the voltage was applied before flow initiation. As the hydrogen bubbles were generated, they rose from the wire until a sheet of bubbles extended from the wire to the surface of the water. The water was thus seeded with hydrogen bubbles before the flow started. When the flow was initiated, the bubbles were trapped in the flow where they were assumed to represent fluid particles. This eliminated one source of turbulence found in the standard hydrogen bubble technique.

The two items explained in the preceding paragraphs produced most of the desired improvement in the flow visualization system. Additional improvement was obtained through the use of a second bank of four 500-watt photo lights, and the lining of the test section with 4-foot lengths of household aluminum foil held in place with plastic tape. These four items produced a substantial improvement in the quality of data obtained using the flow visualization system at a very low cost. Figure III-1 shows a schematic diagram of the

improved flow visualization system just before the flow is started.

Results obtained from the use of this system are presented in

Chapter V.

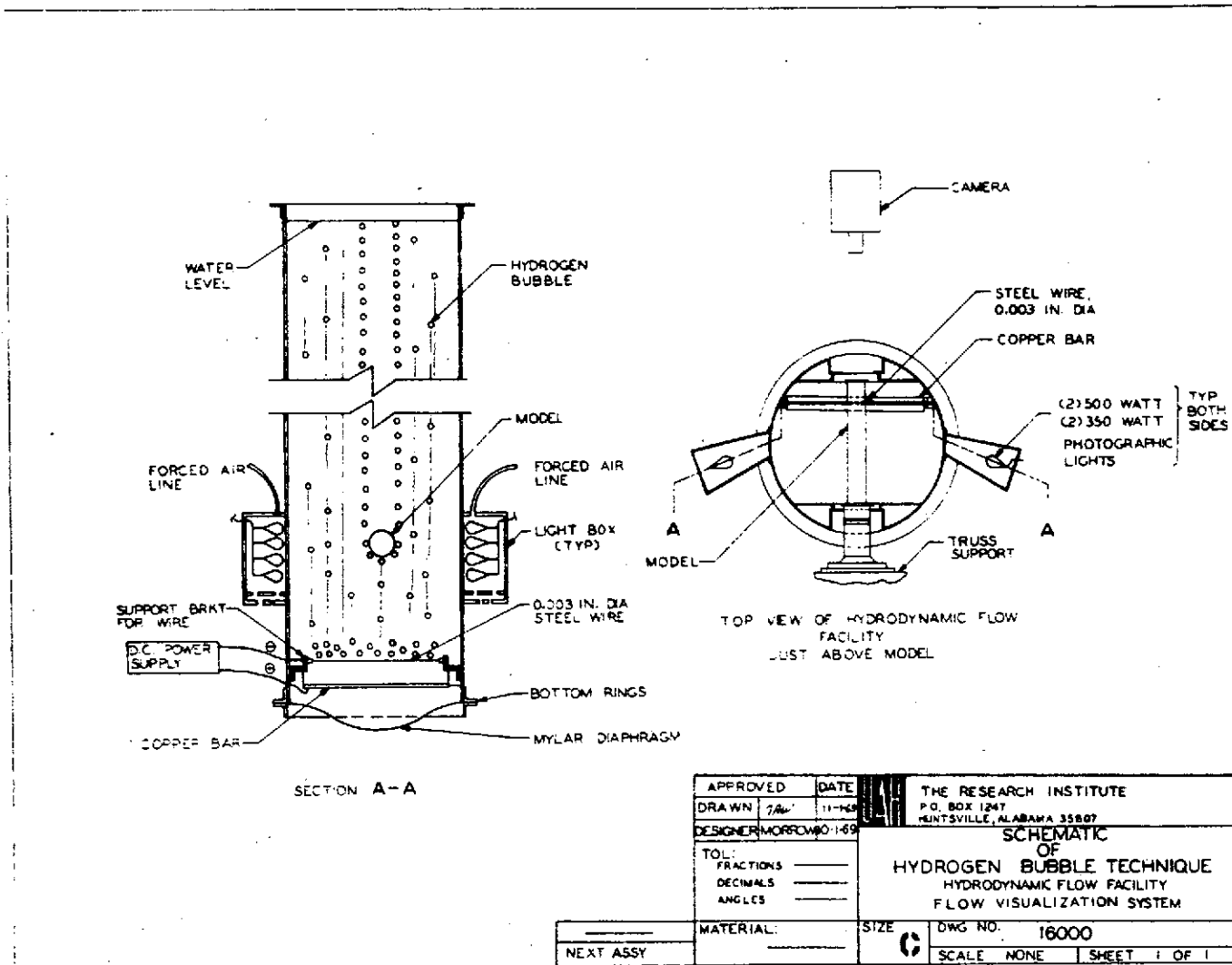


FIGURE III-1. SCHEMATIC DIAGRAM OF IMPROVED FLOW VISUALIZATION SYSTEM

CHAPTER IV

DATA REDUCTION SYSTEM

A secondary objective of this study was to establish a data reduction system which would minimize the problems associated with the analyses of the large amount of data obtained for each test run. The data reduction system also had to provide a means of reproducing the test data so that simultaneous analyses of data from numerous test runs could be accomplished. Prior experience with other force measuring systems convinced the author that recording and retaining the data in analog signal form on magnetic tape represented the most flexible way of storing and reproducing the test data. The fact that data is stored electrically rather than graphically permits automatic reduction, allows repetitive recreating of test data, and permits time-base expansion or contraction for optimum analysis.

A. System Components

An investigation of the recording equipment at the UAH Research Institute located the instrumentation necessary not only to establish an analog recording system, but also to interface with the UNIVAC 1108 digital computing system. The major problem

associated with this equipment was that the analog-to-digital conversion module was limited to basically static data since the maximum sampling rate was 15 samples per second. However, the use of one of the advantages of magnetic tape recording, time-base expansion, permitted the circumvention of this problem. After careful study, a digital data reduction system was established using the following instrumentation:

- (1) Honeywell Medium Band Tape Recorder, Model 7610
- (2) Hewlett-Packard Data Acquisition System, Model 20128
- (3) Honeywell Accudata III Wide Band Amplifiers,
Model D15A-1003
- (4) System Research Corporation DC Power Supply,
Model 3560
- (5) System Research Corporation Signal Conditioning
System, Model 3600
- (6) UNIVAC Digital Computer System, Model 1108
- (7) Stromberg-Carlson Plotter, Model 4020.

Figure IV-1 shows a schematic diagram of the data flow through this system. Appendix D gives a description of each component together with an explanation of the method of time base expansion and data point-time correlation.

UNSTEADY HYDRODYNAMIC
FLOW FACILITY

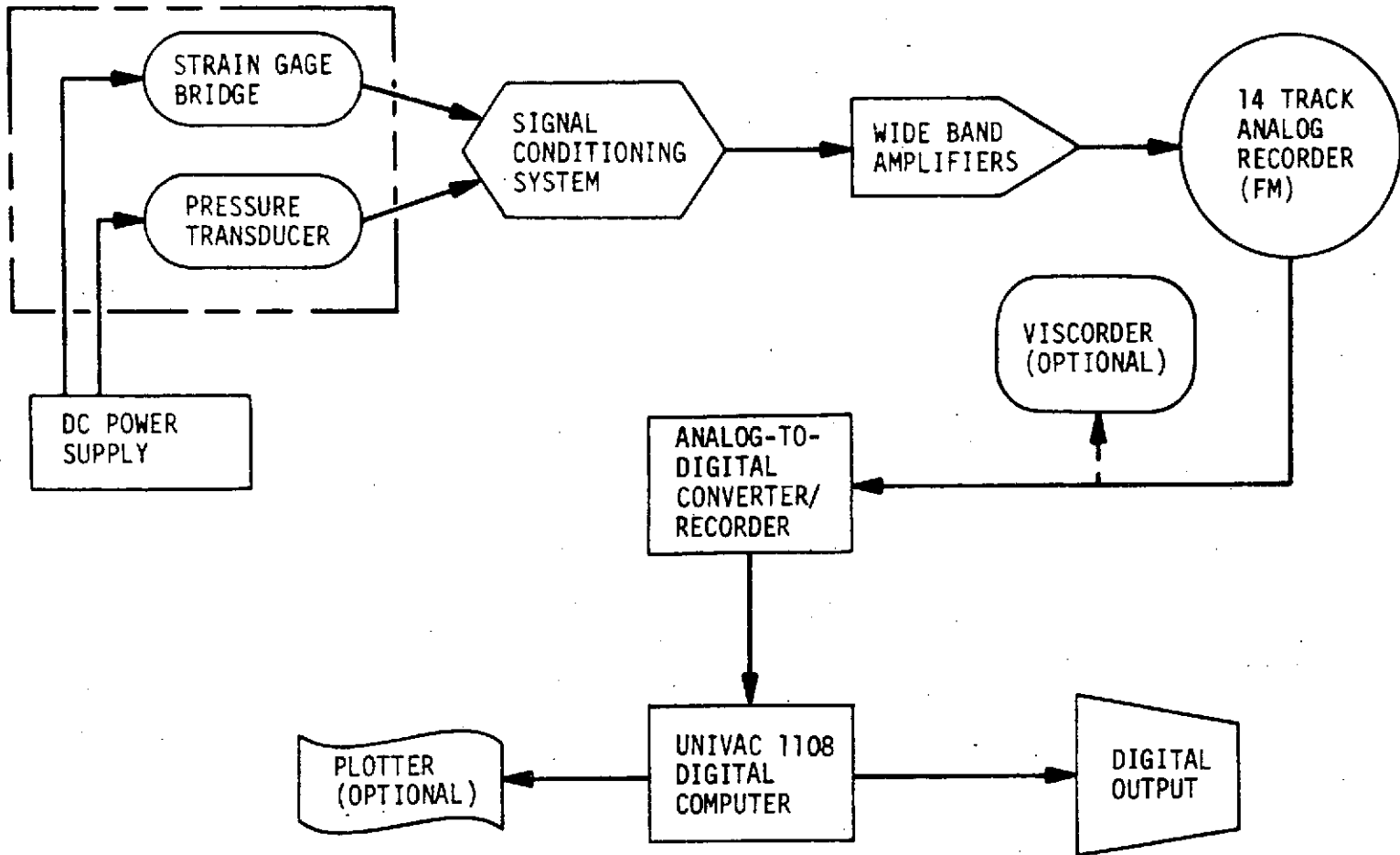


FIGURE IV-1. SCHEMATIC DIAGRAM OF DATA REDUCTION SYSTEM

B. Method of Filtering

The method of filtering selected makes use of a recent innovation in digital computation, the Fast Fourier Transform (FFT). The FFT is an algorithm which facilitates signal analysis by means of digital computers. It is a highly efficient procedure for computing the Discrete Fourier Transform (DFT) of a time series. The DFT has mathematical properties analogous to those of the Fourier integral transform and is particularly useful for power spectrum analysis and filter simulation on digital computers. Reference 21 provides a bibliography on the FFT while References 22 and 23 present detailed explanations of this computational tool.

The FFT digital computer program (Ref. 24) used in this analysis was strictly for filter simulation. The digital method of filtering was selected over electronic filtering for two reasons. One was the excellent roll-off characteristics of a FFT simulated filter as indicated by Figure IV-2. This figure represents the frequency response of a low pass filter with a cut-off frequency of 20 hertz. Figures IV-3 and IV-4 present typical examples of unfiltered and filtered drag and lift channel outputs. The low pass filter of Figure IV-2 was used in each example and was used throughout the entire test series except in a specific filter cut-off frequency analysis. The second reason was the man-hours associated with digitizing the test data. Electronic filtering of the same test data at different frequencies required separate digitizing for each frequency because the

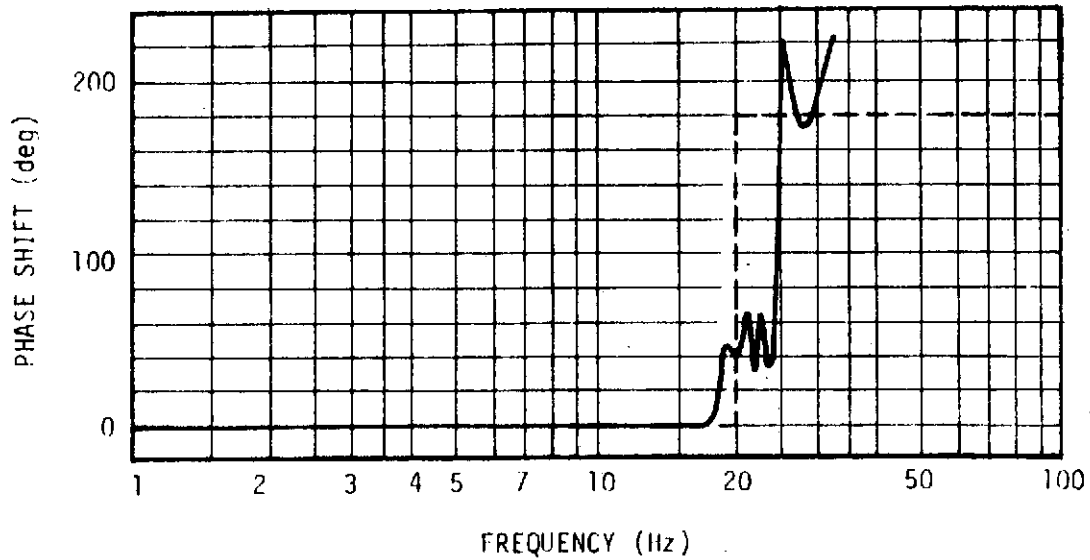
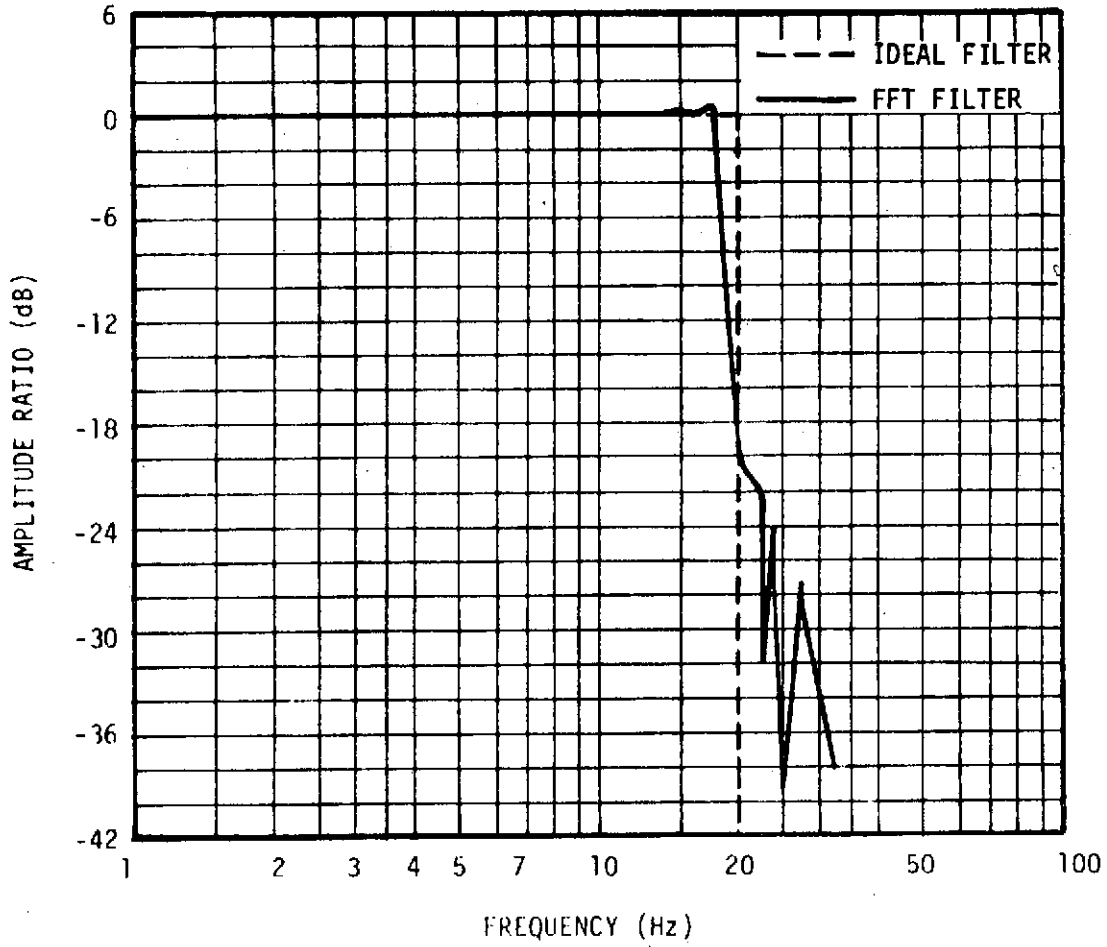


FIGURE IV-2. FREQUENCY RESPONSE OF FAST FOURIER TRANSFORM SIMULATED LOW PASS FILTER, $F_C = 20$ HERTZ

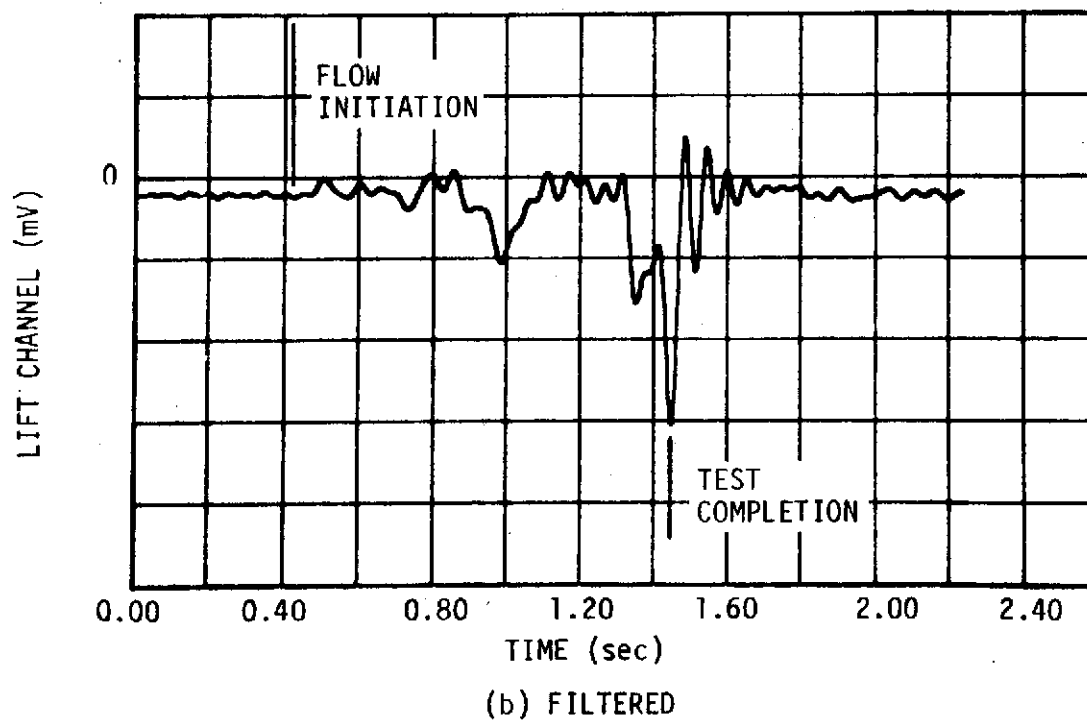
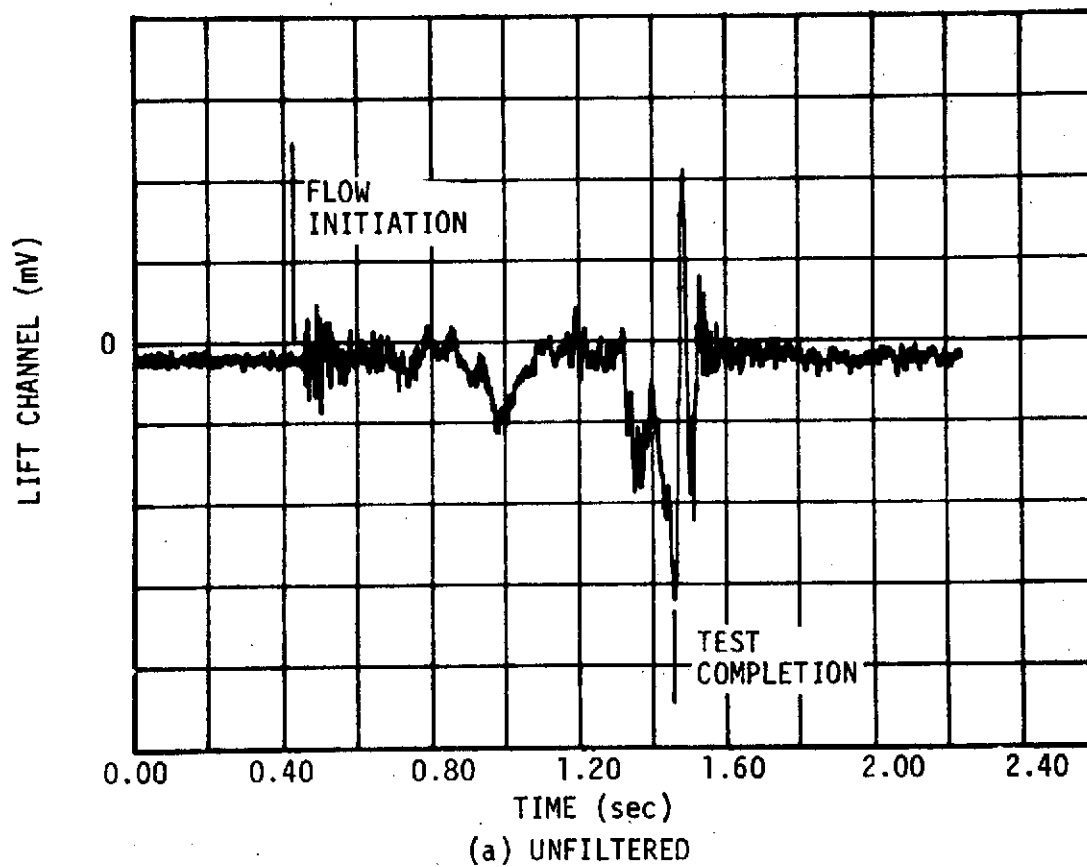
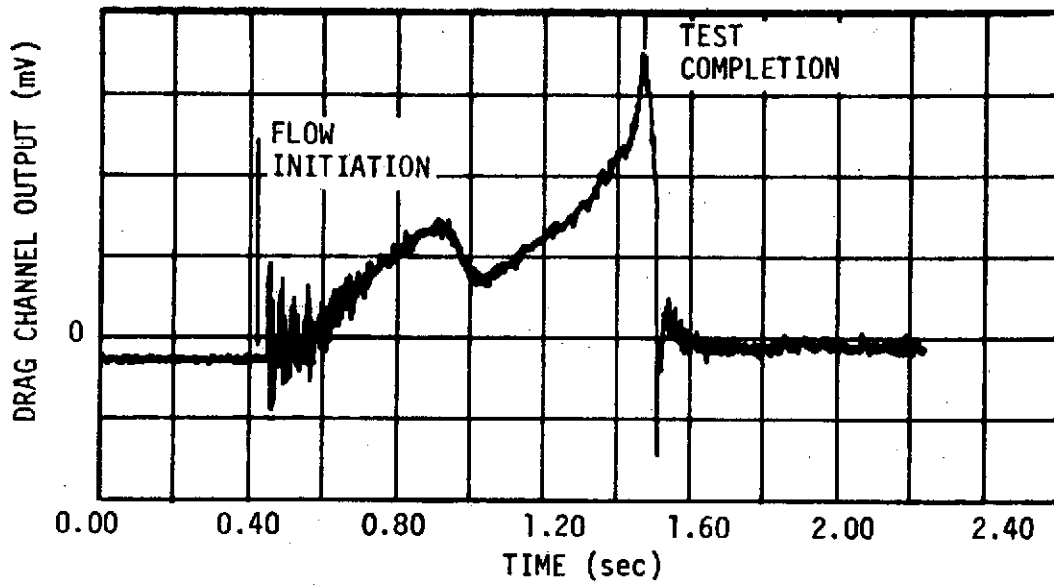
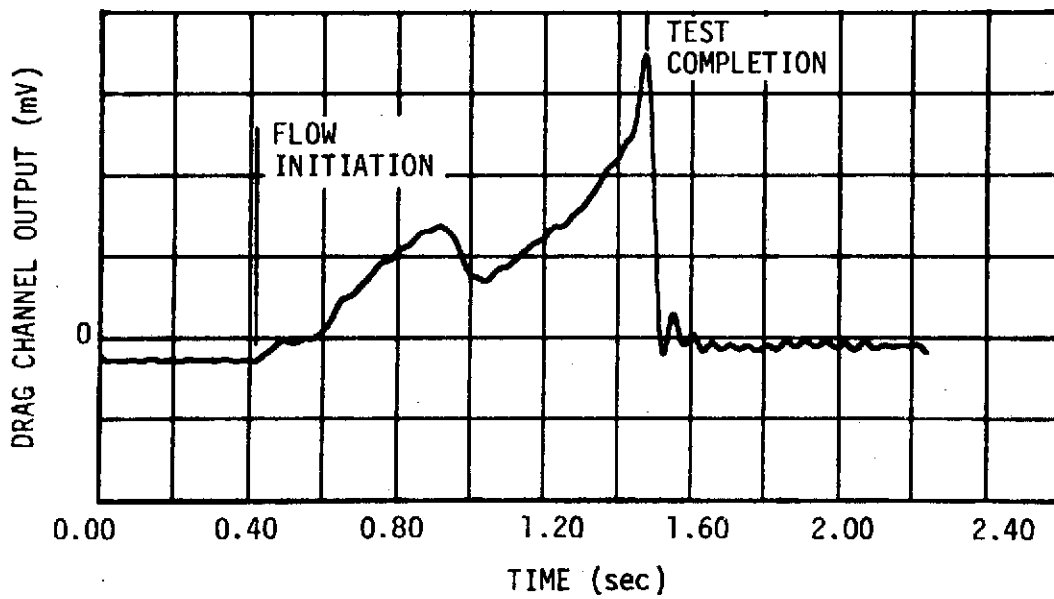


FIGURE IV-3. UNFILTERED AND FILTERED LIFT CHANNEL OUTPUT



(a) UNFILTERED



(b) FILTERED

FIGURE IV-4. UNFILTERED AND FILTERED DRAG CHANNEL OUTPUT

filtering had to be accomplished with the data in analog form. Each test run at one frequency required approximately 4 man-hours to digitize; thus, electronic filtering represented a highly efficient operation since digital filtering required only 2 minutes of digital computing time.

CHAPTER V

EXPERIMENTAL RESULTS

These experimental results were obtained using the systems discussed in the preceding chapters. Measurements of the integrated forces imposed on a 3-inch-diameter, right-circular cylinder submerged in time-dependent flows were accomplished for two area ratios¹, 1.0 and 1.4. Originally, the test plan called for force measurements in fluid flows established by two additional area ratios, 4.0 and 8.35. However, efforts to obtain force measurements in these flows were unsuccessful because of the small magnitude of the fluid accelerations and velocities produced by these area ratios. Several attempts were made to obtain force data for these area ratios, especially $A_1/A_2 = 4.0$, but the force levels obtained were below the resolution sensitivity² of the force measuring system. Force data obtained for the two area ratios are presented in the

¹ Area ratio, A_1/A_2 , is defined as the ratio of total test section cross-sectional area, no model installed, to exit cross-sectional area.

² Resolution sensitivity is defined as the minimum change in the measured variable which produces an effective response in the instrument.

following sections in both force magnitude and coefficient forms. Flow parameters used in nondimensionalizing the force data are also presented. A comparison of the measured drag coefficient data with steady flow drag coefficient data also is shown with selected photographs taken from 16-millimeter film used to illustrate the complex flow fields surrounding a circular cylinder immersed in a time-dependent flow. Finally, the facility-related and model configuration-related parameters which might influence the force data are discussed.

A. Flow Parameters

Fluid accelerations were computed using static pressures measured by flush mounted transducers located at different heights in the facility wall. The procedure used in computing fluid accelerations from differential static pressure measurements is explained by Schutzenhofer (Ref. 4). The equation used in this procedure is

$$A = g - \frac{\Delta P}{\rho_0 \Delta H} \quad (V-1)$$

where

- A - fluid acceleration
- g - acceleration of gravity

ΔP - pressure difference between adjacent wall-mounted transducers

ρ_0 - fluid density

ΔH - height between the particular pressure transducers.

Before the fluid accelerations were calculated, the pressure measurements were filtered using the low pass digital filter shown in Figure IV-3.

Fluid velocities, V , and fluid displacements, S , were computed by numerically integrating a segmented, third-order curve obtained by "curve fitting" the fluid accelerations. Four different segments were required because of the necessity of using data from different pairs of transducers as the fluid height decreased. The fourth segment of the curve was obtained by extrapolating the fluid accelerations obtained for the previous segments. For the area ratio 1.0 test runs, this extrapolation became necessary after 0.7 seconds. The fluid acceleration level computed for all area ratio 1.0 tests did not exceed a 0.5-percent variation from a 1-g acceleration during the first three segments; consequently, it is believed that the use of a constant 1-g acceleration for the fourth segment does not significantly influence the area ratio 1.0 coefficient data.

The primary nondimensionalizing factor used in this study was that developed by Schutzenhofer (Ref. 4) which includes the

fluid acceleration as well as the square of the fluid velocity. This method of nondimensionalizing was shown to be appropriate for both steady and time-dependent flows. Equation V-2 shows this method of nondimensionalizing as it applies to force data using the drag force as an example:

$$C_d = \frac{\text{Drag Force}}{(0.5 \rho_o V^2 + D A \rho_o) \cdot L \cdot D} \quad (\text{V-2})$$

where

C_d - sectional drag coefficient

ρ_o - fluid density

A - fluid acceleration

V - fluid velocity

D - model diameter

L - model length.

Typical flow parameters computed for area ratio 1.0 tests are presented in Figure V-1. The instantaneous Reynolds number, $R(t)$, was calculated as a function of time using the flow velocities, V , the cylinder diameter, D , the fluid density, ρ_o , and the fluid viscosity, μ .

Figure V-2 presents the fluid acceleration and velocity obtained for a typical area ratio 1.4 test. The fluid acceleration can be seen to start at a 1-g level, decreasing to zero at approximately 0.78 seconds. This flow data was obtained using the same

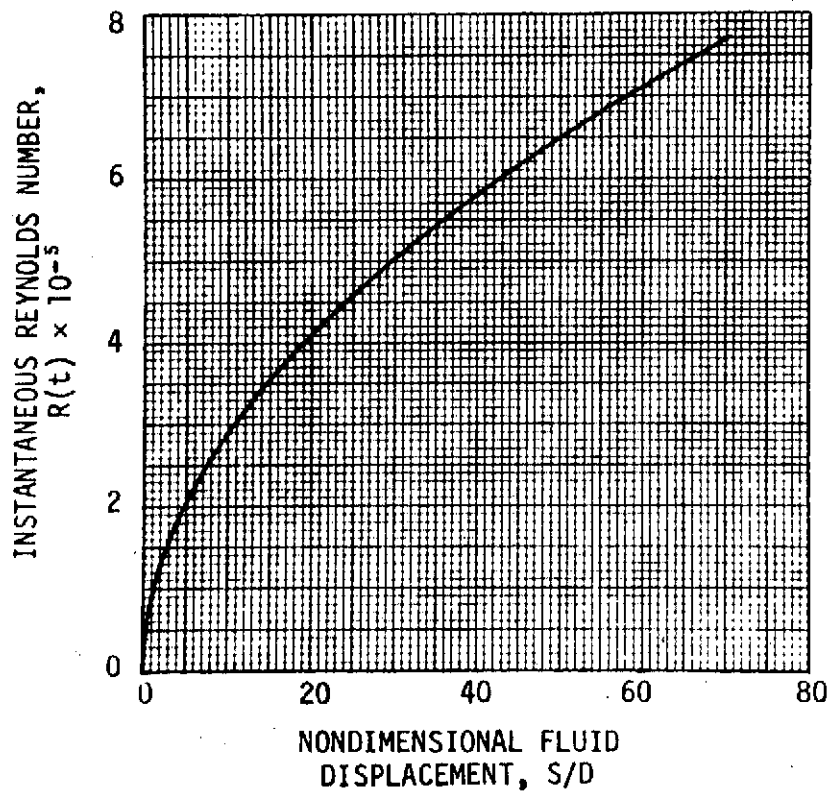
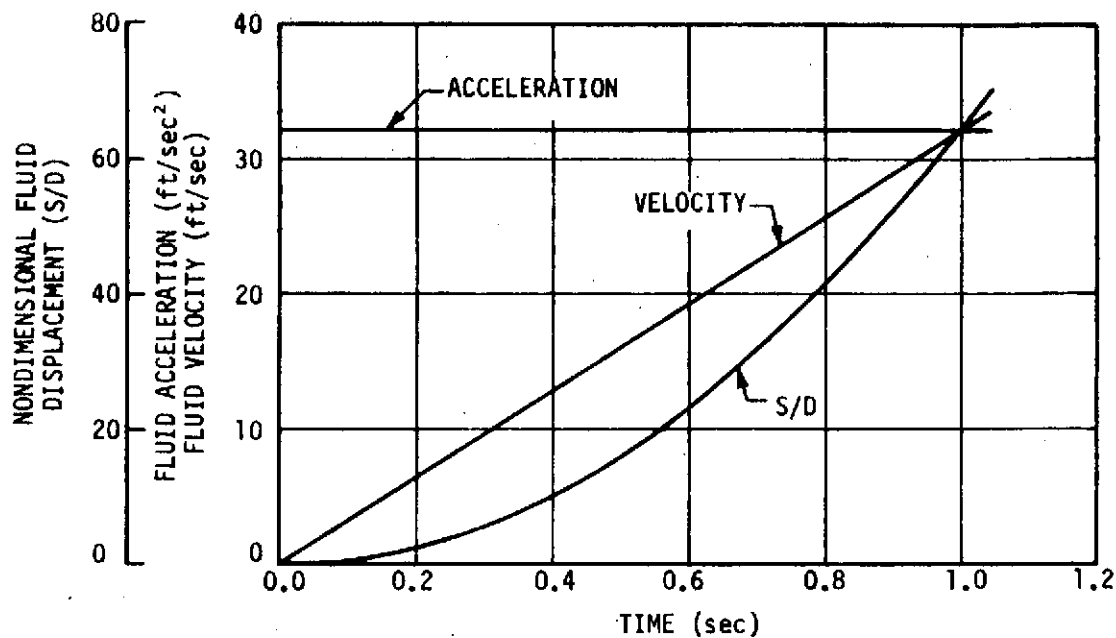


FIGURE V-1. TYPICAL FLOW PARAMETERS FOR AN AREA RATIO 1.0 TEST

CD

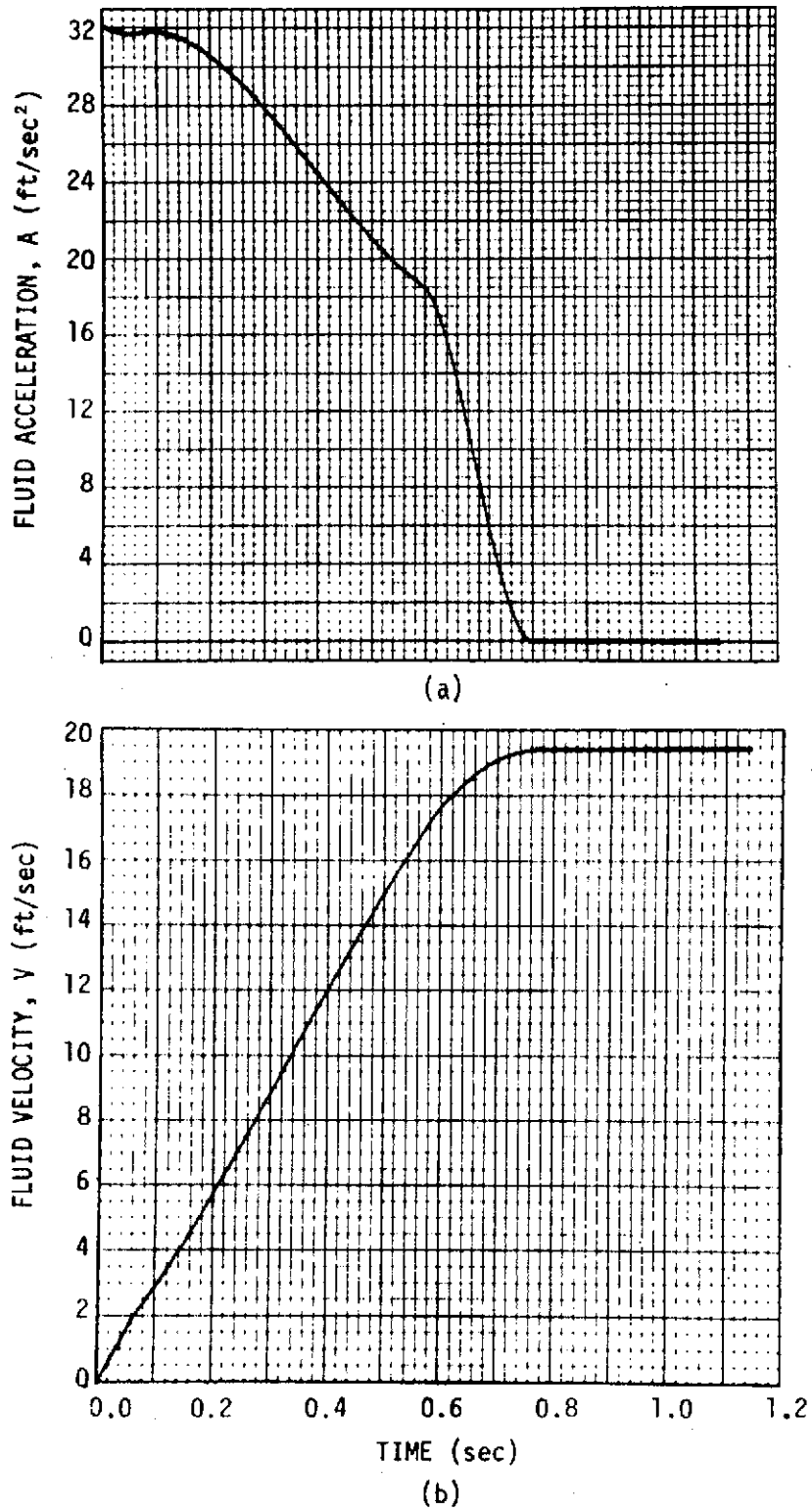


FIGURE V-2. FLUID ACCELERATION AND FLUID VELOCITY AS A FUNCTION OF TIME FOR A TYPICAL AREA RATIO 1.4 TEST

procedure as the area ratio 1.0 data. The extrapolation segment of the fluid acceleration curve was the zero acceleration period.

The nondimensional fluid displacement, S/D , and the instantaneous Reynolds number calculated for this typical area ratio 1.4 test are presented in Figure V-3.

B. Force Data

The total lift force measured by the force measurement system during a typical area ratio 1.0 test is presented in Figure V-4 as a function of nondimensional fluid displacement, S/D .

Sarpkaya and Garrison (Ref. 25) have shown that the nondimensional fluid displacement is a useful parameter for correlating the effects of various magnitudes of time-dependent flows. The sign given to the lift force is arbitrary. The large negative lift force indicated at an S/D of approximately 66 is a result of the fluid free surface nearing the model location.

Figure V-5 presents a typical drag force measurement for an area ratio of 1.0. The sudden decrease in drag force corresponding to the beginning of the critical Reynolds number regime is apparent at an S/D of approximately 14. The sudden increase in drag force at an S/D of approximately 66 is also the result of the fluid free surface nearing the model.

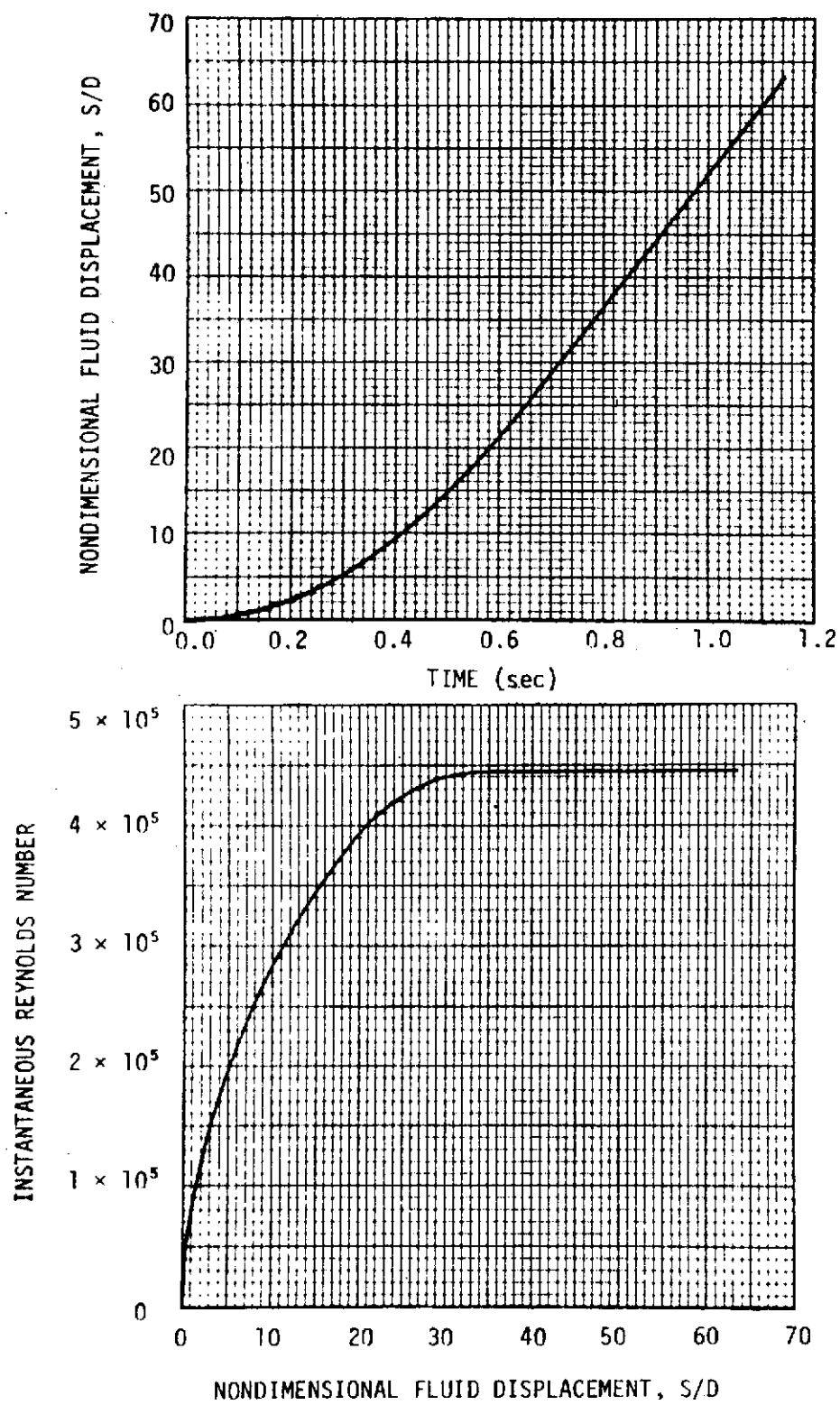


FIGURE V-3. FLOW PARAMETERS FOR A TYPICAL AREA RATIO 1.4 TEST

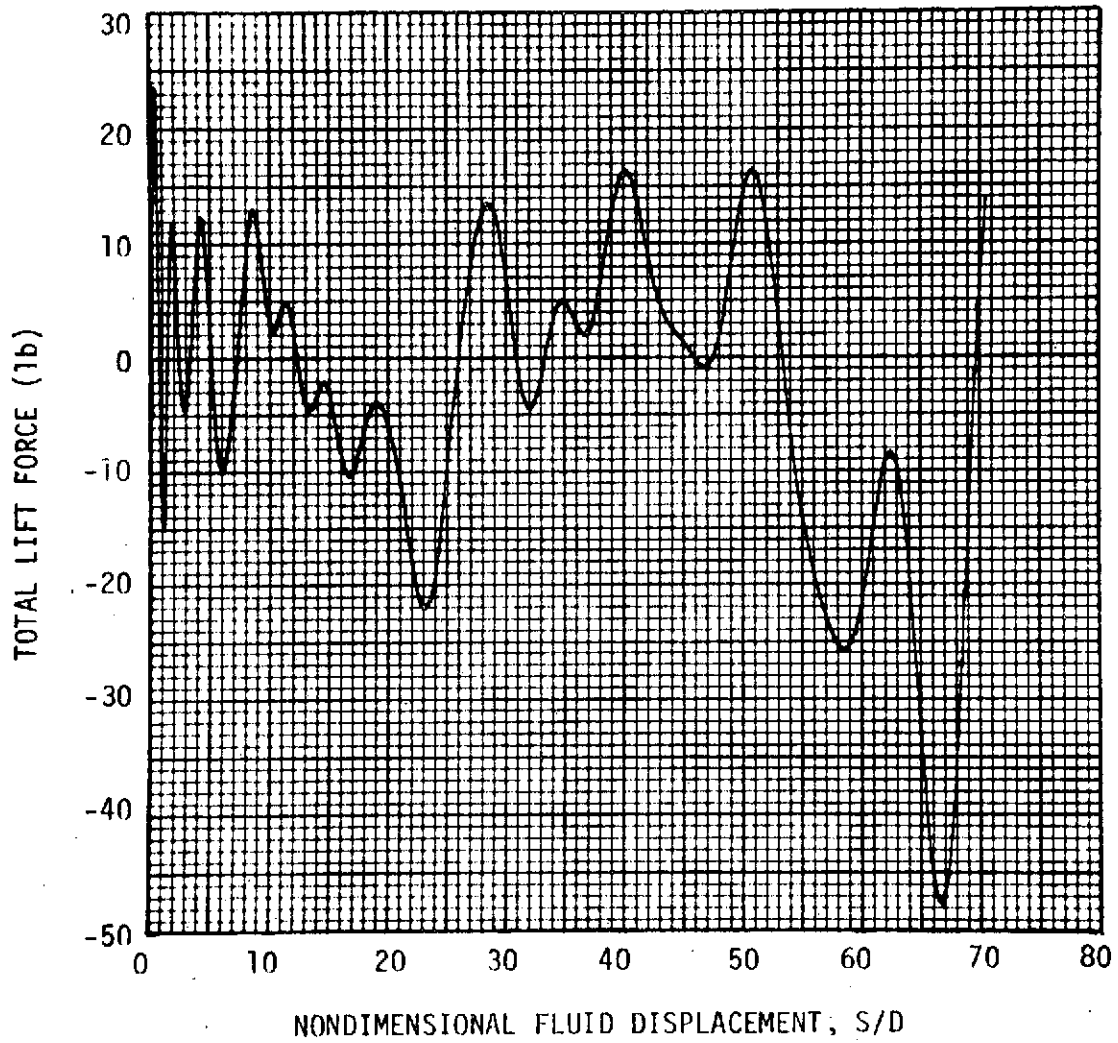


FIGURE V-4. TOTAL LIFT FORCE AS A FUNCTION OF NONDIMENSIONAL FLUID DISPLACEMENT, S/D, FOR A TYPICAL AREA RATIO 1.0 TEST

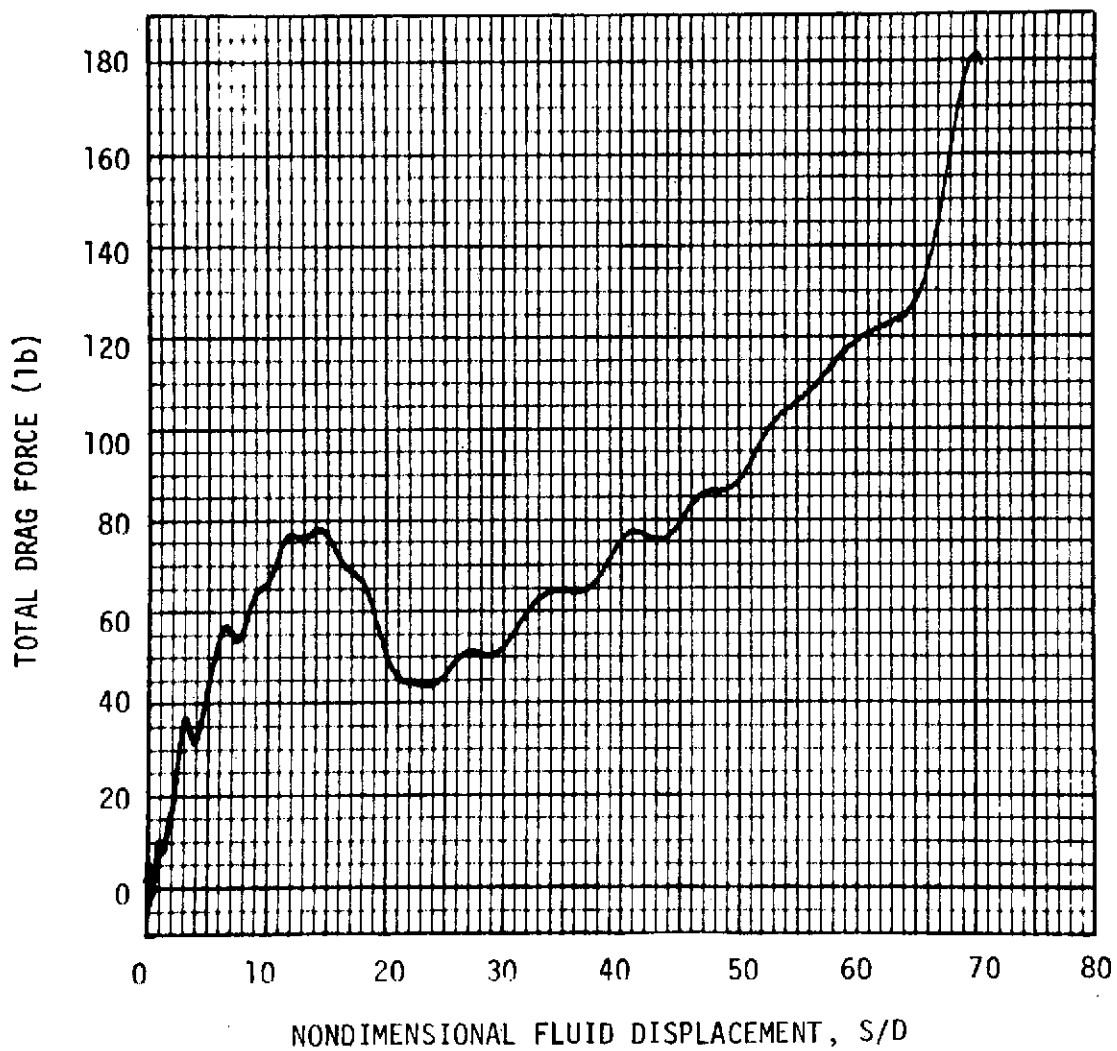


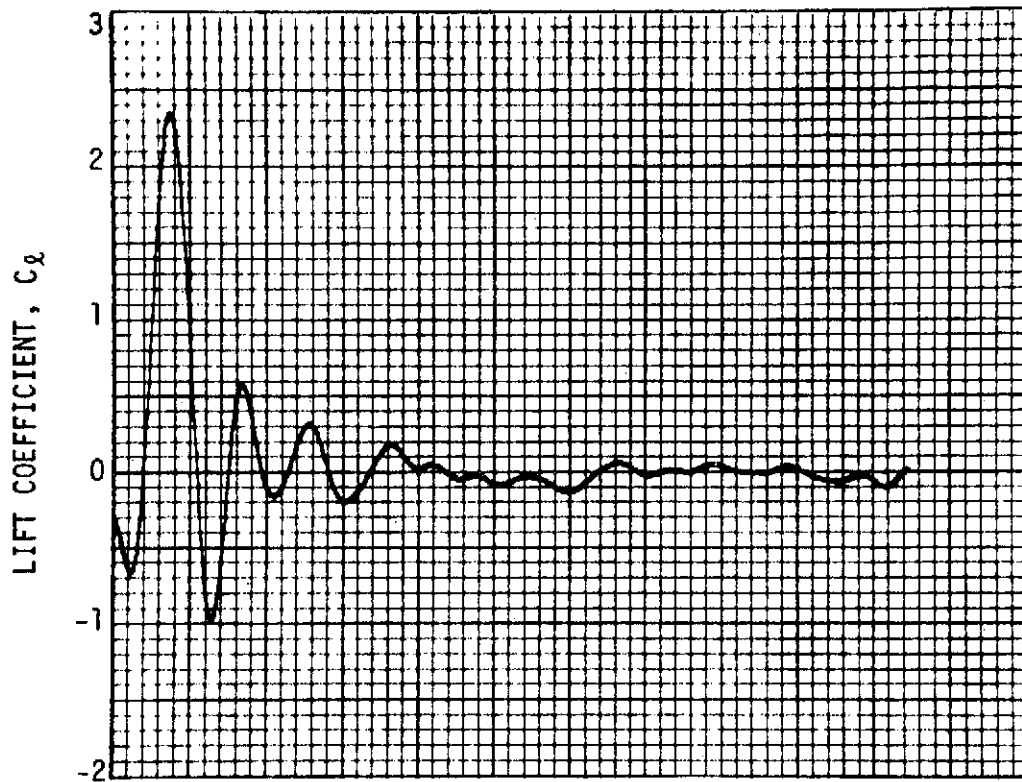
FIGURE V-5. TOTAL DRAG FORCE AS A FUNCTION OF NONDIMENSIONAL FLUID DISPLACEMENT, S/D, FOR A TYPICAL AREA RATIO 1.0 TEST

Figures V-6 and V-7 present sectional lift (C_l) and drag (C_d) coefficients³ calculated using the forces presented in Figures V-4 and V-5. Figure V-6 shows the coefficient variations with time while Figure V-7 shows the coefficient variations with non-dimensional fluid displacement, S/D .

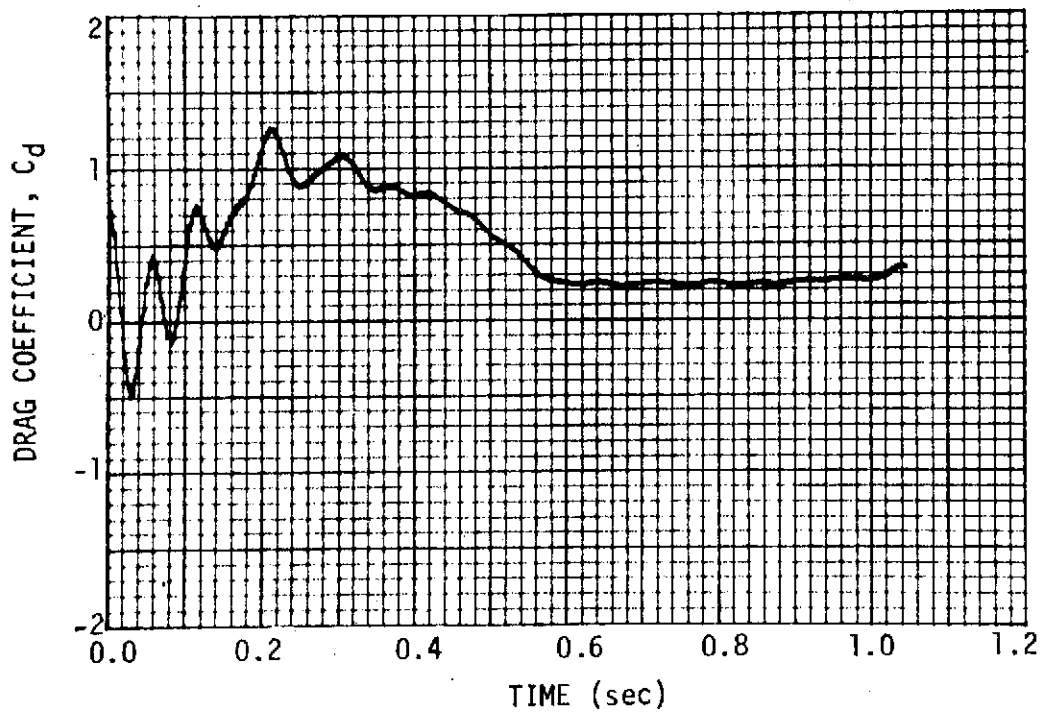
Figure V-8 shows plots of the lift and drag coefficients obtained for area ratio 1.0 tests as a function of the instantaneous Reynolds number. The data in Figure V-8 begin at an instantaneous Reynolds number of 1×10^5 because of the transient dynamics of the model-balance combination created at the initiation of the test run. Figure V-8a shows the randomness of the lift coefficients obtained for all test runs of area ratio 1.0 when plotted as a function of the instantaneous Reynolds number.

A plot of the drag coefficients obtained for the accelerating flows produced by the area ratio 1.0 tests is shown on Figure V-8b. Although some data scatter is shown below the instantaneous Reynolds number of 3×10^5 , good agreement is shown in the general trend and magnitude of drag coefficient. The variation in minimum drag coefficient determined for the area ratio 1.0 flows was from 0.184 to 0.230 at instantaneous Reynolds numbers of approximately 5.5×10^5 . This is a variation of 20 percent.

³Hereafter referred to as lift and drag coefficients.

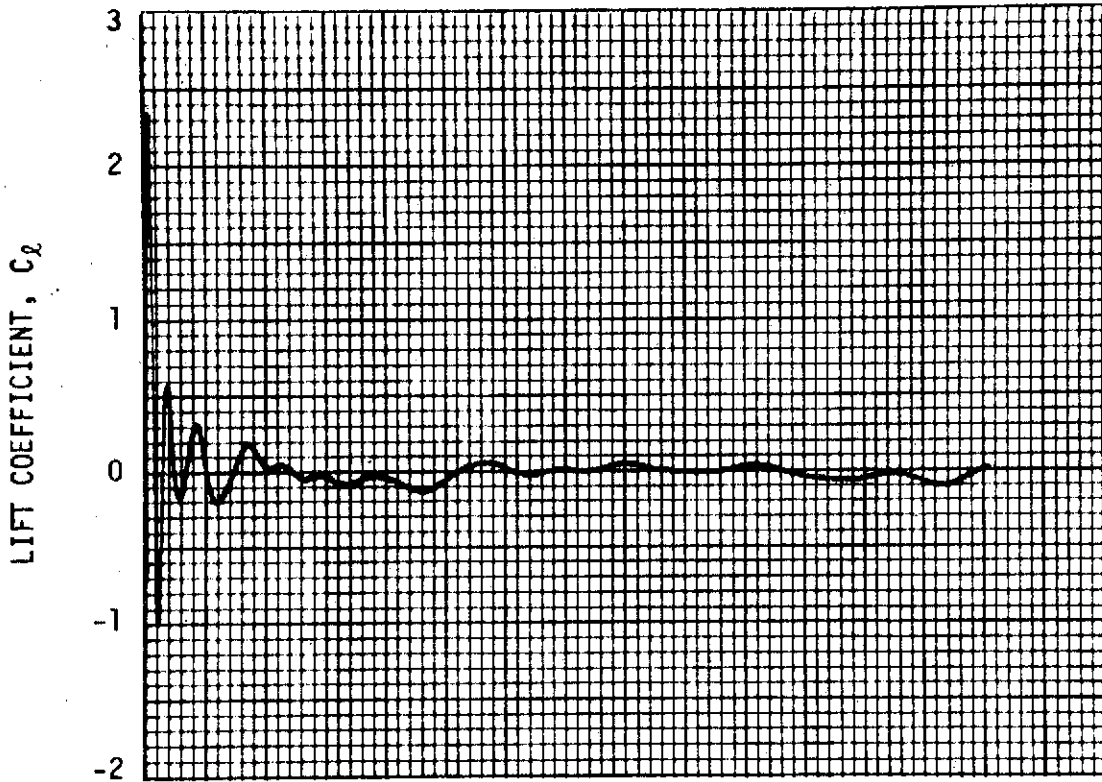


(a)



(b)

FIGURE V-6. LIFT AND DRAG COEFFICIENTS AS A FUNCTION OF TIME FOR A TYPICAL AREA RATIO 1.0 TEST



(a)

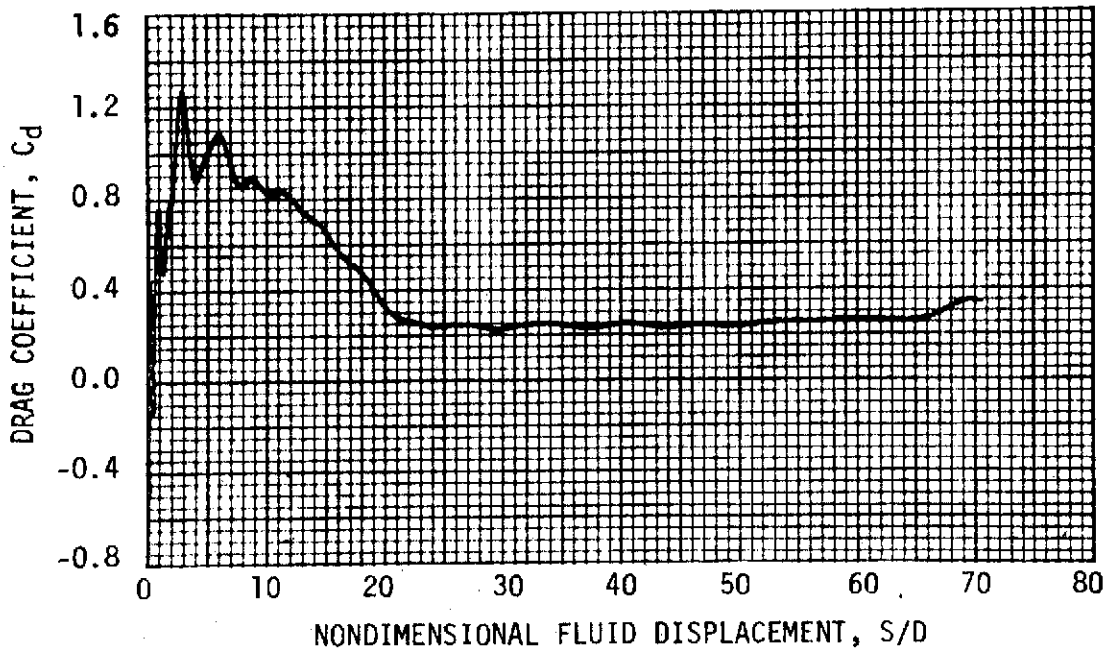
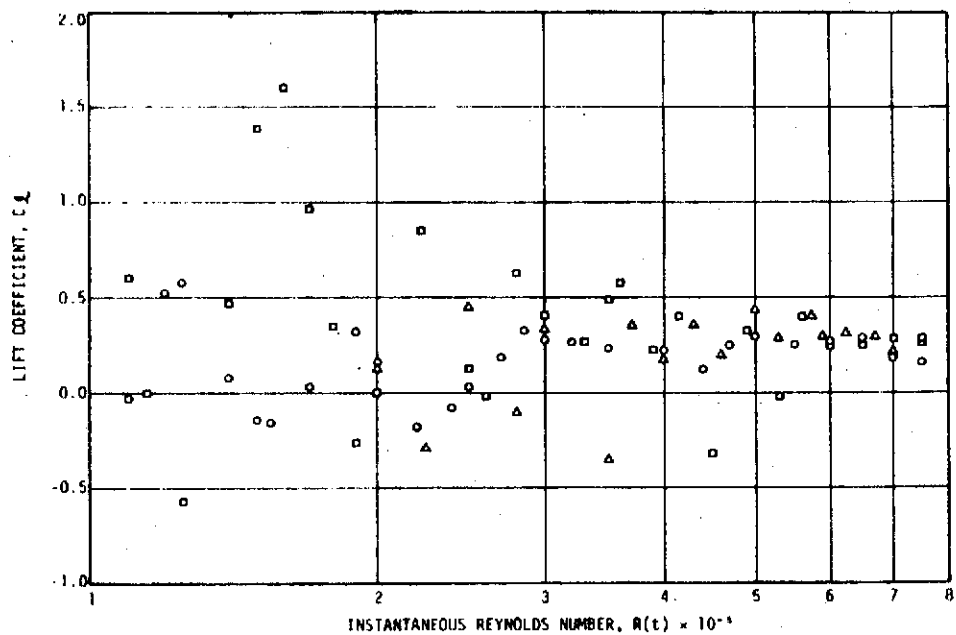
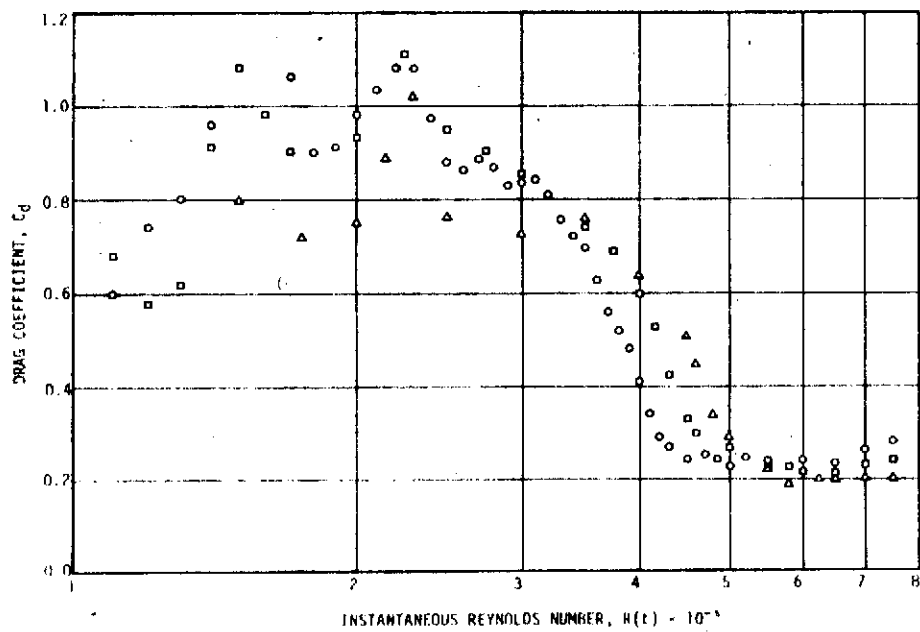


FIGURE V-7. LIFT AND DRAG COEFFICIENTS AS A FUNCTION OF NON-DIMENSIONAL FLUID DISPLACEMENT, S/D , FOR A TYPICAL AREA RATIO 1.0 TEST



(A) LIFT COEFFICIENT



(b) DRAG COEFFICIENT

FIGURE V-8. PLOT OF LIFT AND DRAG COEFFICIENTS AS A FUNCTION OF INSTANTANEOUS REYNOLDS NUMBER FOR TYPICAL AREA RATIO 1.0 TESTS

The integrated lift force imposed on the circular cylinder during a typical area ratio 1.4 test is presented in Figure V-9. The bias indicated by the data of Figure V-9 is typical of all lift data obtained for area ratio 1.4 tests. No explanation of this bias is determined.

Figure V-10 shows the total drag force determined for the typical area ratio 1.4 test. The initial portion, $S/D \leq 20$, of this curve is similar to that obtained for an area ratio 1.0 test, although delayed somewhat because of the smaller fluid acceleration and, consequently, the fluid velocity. The constant velocity assumption for the area ratio 1.4 tests shows up in that the drag force stays at a level consistent with a steady velocity in the critical Reynolds number regime after an S/D of approximately 36.

Plots of the lift and drag coefficients obtained for the area ratio 1.4 tests are shown in Figure V-11. The bias in lift force and the randomness of the lift data are clearly shown in Figure V-11a while the constant velocity or constant Reynolds number effect is apparent in the drag data presented in Figure V-11b.

The effect of the low pass filter cut-off frequency on the drag coefficient data obtained for a typical area ratio 1.0 test is shown in Figure V-12. Although the initial portion (time < 0.3 second) of these data does indicate a more oscillatory pattern as the filter cut-off frequency is increased, that portion of the data

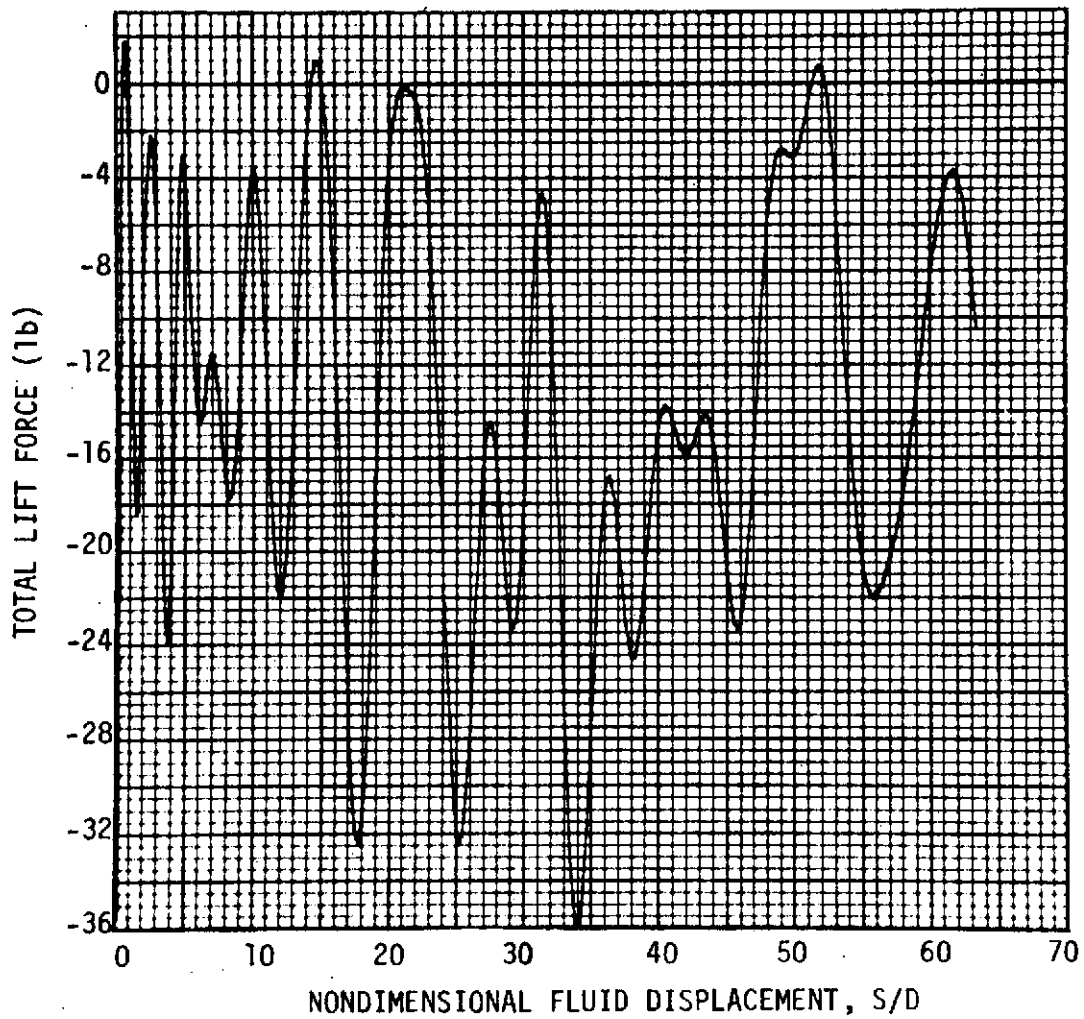


FIGURE V-9. TOTAL LIFT FORCE AS A FUNCTION OF NONDIMENSIONAL FLUID DISPLACEMENT, S/D, FOR A TYPICAL AREA RATIO 1.4 TEST

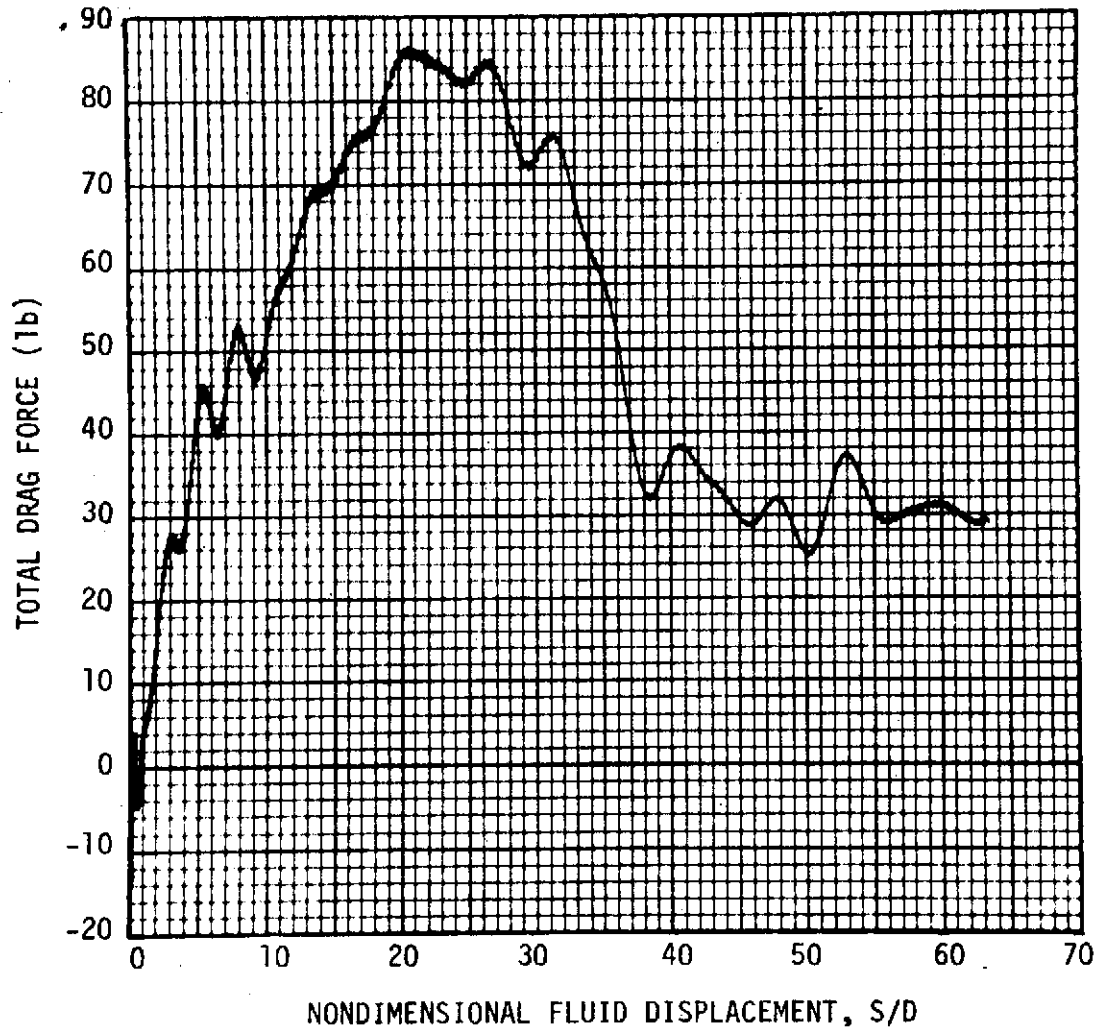
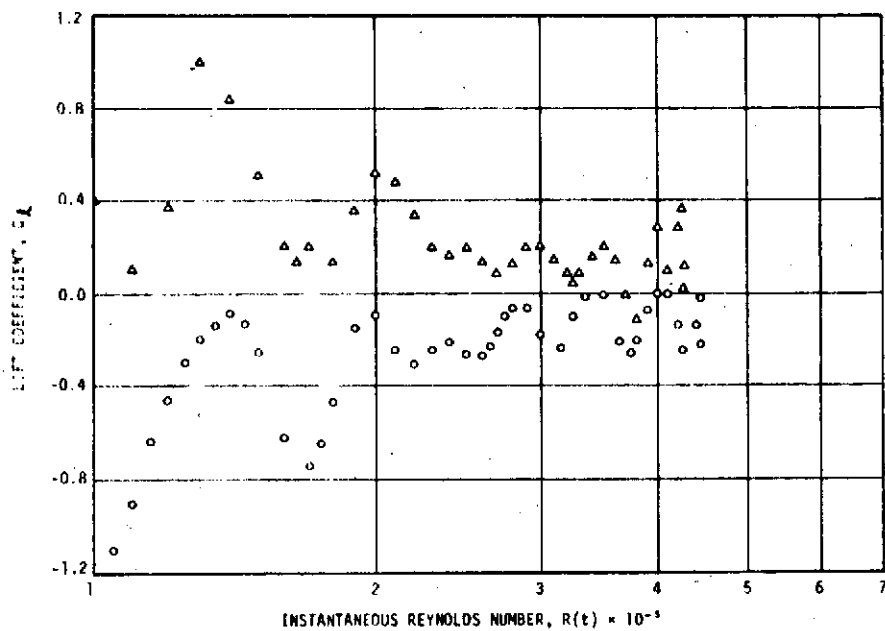
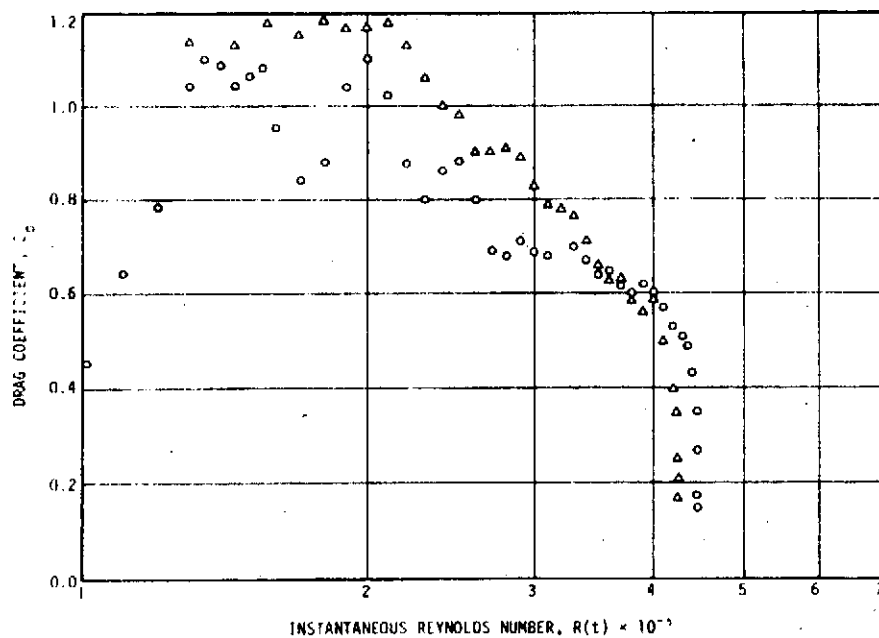


FIGURE V-10. TOTAL DRAG FORCE AS A FUNCTION OF NONDIMENSIONAL FLUID DISPLACEMENT, S/D, FOR AN AREA RATIO 1.4 TEST



(a) LIFT COEFFICIENT



(b) DRAG COEFFICIENT

FIGURE V-11. PLOT OF LIFT AND DRAG COEFFICIENTS AS A FUNCTION OF INSTANTANEOUS REYNOLDS NUMBER FOR AREA RATIO 1.4 TESTS

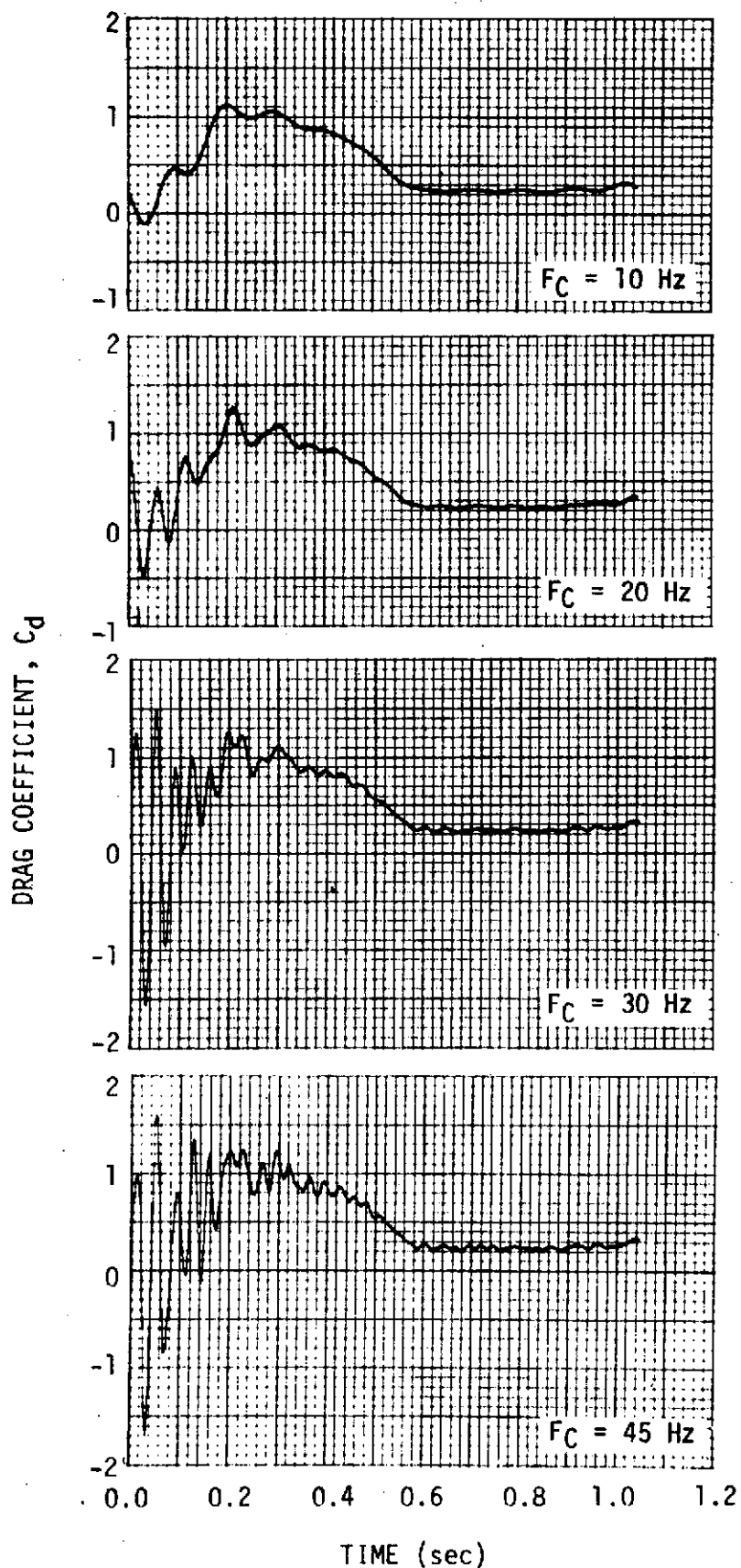


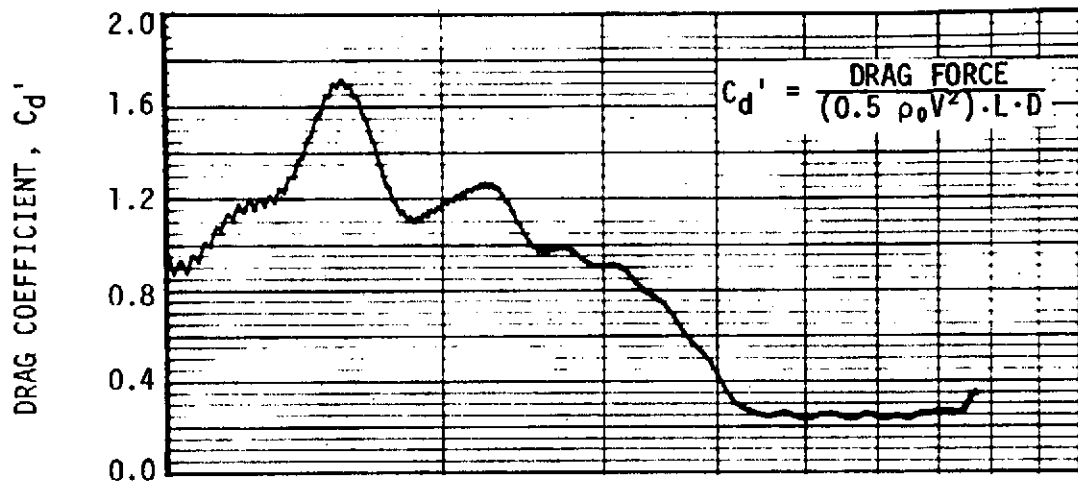
FIGURE V-12. EFFECTS OF LOW PASS FILTER CUTOFF FREQUENCY ON DRAG COEFFICIENT FOR AN AREA 1.0 TEST

in the critical Reynolds number regime (time ≥ 0.6 second) is essentially the same for all cut-off frequencies, 10 hertz through 45 hertz. The magnitude of the minimum drag coefficient has a variation of 10 percent over this filter cut-off frequency range.

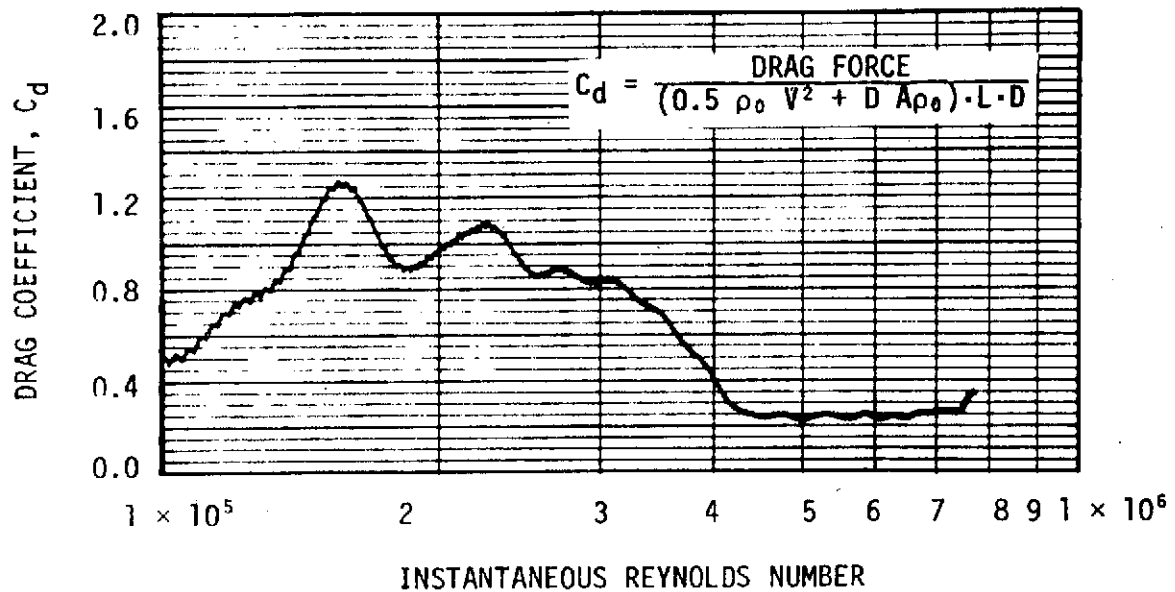
The effects of not including the acceleration term in nondimensionalizing the drag force obtained for an area ratio 1.0 test is shown by the data of Figure V-13. These data indicate that the acceleration term is important only during the initial portion of the test (time < 0.30 second). However, for unsteady flows with a low velocity, the inclusion of the acceleration term might provide a more meaningful method of nondimensionalizing test data.

C. Comparison with Steady Flow Data

A comparison of the drag coefficients measured during this investigation of the forces imposed by unsteady flows with those measured by other investigators in steady flows is presented on Figure V-14. The conventional practice of nondimensionalizing using only the flow velocity ($0.5 \rho_0 V^2$) was used in this comparison. These data agree quite well with those measured by Delaney and Sorensen (Ref. 26) on a 4-inch-diameter cylinder. In addition, the minimum drag coefficients obtained during this study lie within the envelope formed by the minimum drag coefficients determined by Delaney and Sorensen and other investigators such as Jones (Ref. 7) and Schmidt (Ref. 27).



(a) CONVENTIONAL NONDIMENSIONALIZING



(b) NONDIMENSIONALIZING USING BOTH ACCELERATION AND VELOCITY

FIGURE V-13. COMPARISON OF THE EFFECTS OF NONDIMENSIONALIZING FACTORS ON DRAG COEFFICIENT FOR AN AREA 1.0 TEST

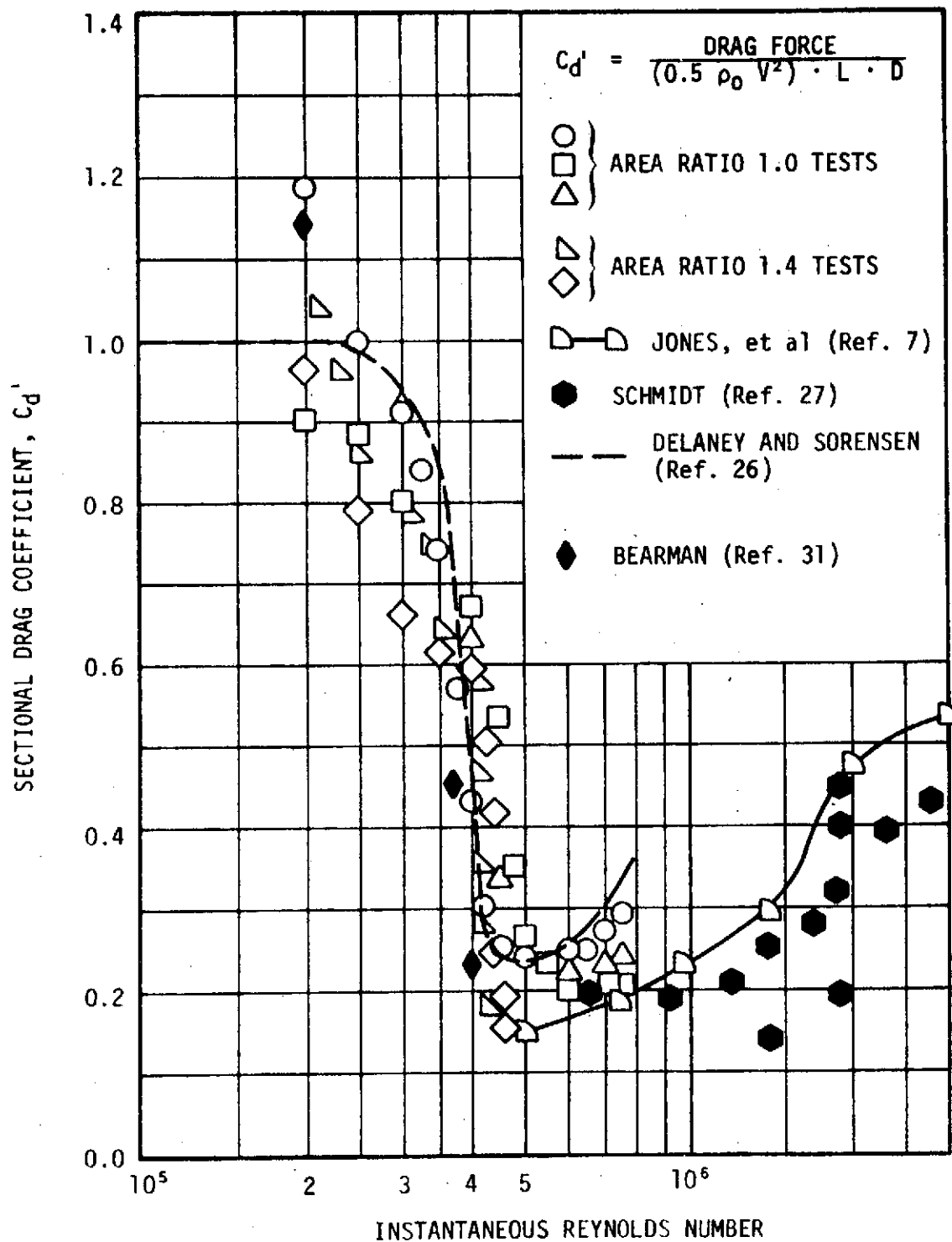


FIGURE V-14. COMPARISON OF SECTIONAL DRAG COEFFICIENTS OBTAINED FOR TIME-DEPENDENT AND STEADY FLOWS

D. Flow Visualization Data

A series of six photographs taken from a 16-millimeter movie film shot at a rate of 400 frames per second during an area ratio 1.0 test is presented in Figure V-15. The photographs shown were taken from a movie film (Ref. 28) of all the various area ratio tests previously discussed. The photographs of Figure V-15, in which the flow is from left to right as viewed, show the flow fields surrounding the right-circular cylinder at instantaneous Reynolds numbers ranging from 1.30×10^5 to 6.95×10^5 . The instantaneous Reynolds number shown for each photograph was obtained by correlating the number of frames from flow initiation with the instantaneous Reynolds numbers calculated for the constant acceleration (1 g) flow produced by the area ratio 1.0 tests.

Flow fields surrounding the right-circular cylinder in a flow produced by an area ratio 8.35 test are shown in the seven photographs of Figure V-16. These photographs were taken from a film shot at a rate of 200 frames per second. The interesting feature of these flow fields is the "line" of hydrogen bubbles which appears in photographs b through d. This "line" appears in all movie films taken of tests at this area ratio in approximately the same manner. The "line" briefly appears in some movies of area ratio 4.0 tests; however, it is not nearly as pronounced as in the



(a)

$$R(t) = 1.30 \times 10^5$$

$$t = 0.176 \text{ SECOND}$$



(b)

$$R(t) = 2.35 \times 10^5$$

$$t = 0.318 \text{ SECOND}$$



(c)

$$R(t) = 2.60 \times 10^5$$

$$t = 0.353 \text{ SECOND}$$



(d)

$$R(t) = 4.80 \times 10^5$$

$$t = 0.650 \text{ SECOND}$$



(e)

$$R(t) = 5.75 \times 10^5$$

$$t = 0.780 \text{ SECOND}$$



(f)

$$R(t) = 6.95 \times 10^5$$

$$t = 0.942 \text{ SECOND}$$

FIGURE V-15. PHOTOGRAPHS OF FLOW FIELDS SURROUNDING A RIGHT-CIRCULAR CYLINDER SUBMERGED IN A 1-g ACCELERATING FLOW

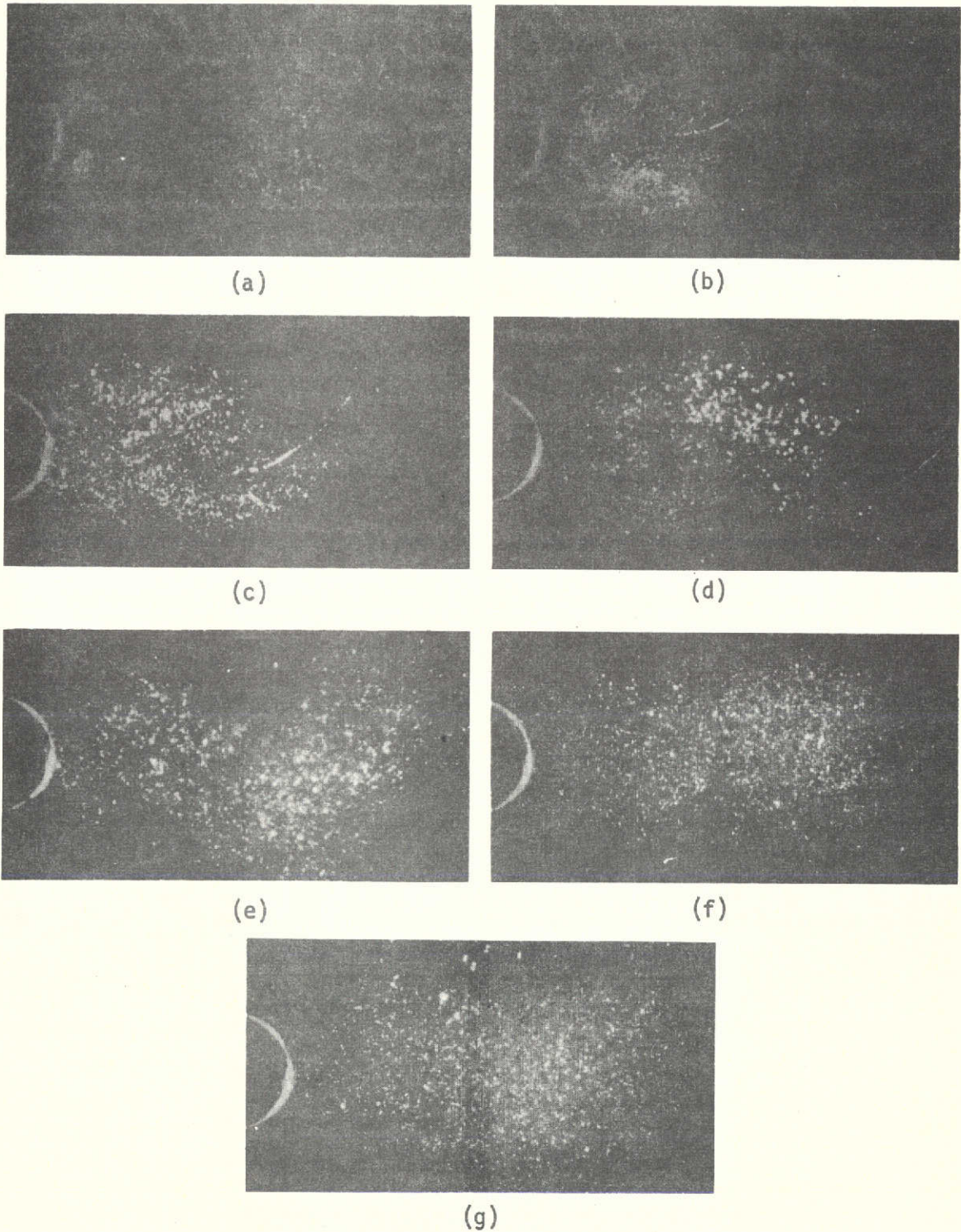


FIGURE V-16. PHOTOGRAPHS OF FLOW FIELDS SURROUNDING A RIGHT-CIRCULAR CYLINDER DURING A TYPICAL AREA RATIO 8.35 TEST RUN

area ratio 8.35 tests. No evidence of this "line" is found in the area ratio 1.0 films. No explanation of the "line" has been determined.

E. Discussion of Results

This investigation has produced drag coefficient data which varies similarly as the well-established steady flow drag coefficient variation with Reynolds number in the critical Reynolds number range. This similarity is shown in Figure V-14 where the results of this investigation and selected steady flow results are plotted as a function of instantaneous Reynolds number. The coefficient data obtained for these tests lie within the envelope of the steady flow data; however, the coefficient data presented herein does exhibit a 20-percent variation in magnitude. Besides the usual factors which cause experimental force data scatter (i. e., balance accuracy and repeatability), the data presented herein are subject to influences which have been shown to especially affect steady flow experimental results in the critical Reynolds number range. To the author's knowledge, no investigation has proven that these influences should not affect time-dependent flow force data in an analogous manner. A listing of some of the more prominent influences and a brief discussion of their possible effects is given below. These influences are:

- (1) Freestream turbulence
- (2) Cylinder surface roughness
- (3) Model end configurations
- (4) Flow three-dimensionality.

Freestream turbulence has been shown by many investigators to be an important factor in defining the drag coefficient variation with Reynolds number in steady flow. For example, Surry (Ref. 29) recently conducted an extensive investigation. Although these tests were conducted in the same facility under supposedly identical conditions, evidence of different levels of freestream turbulence was obtained from close scrutiny of the available movie films. These different turbulence levels possibly resulted from the slightly different bottom opening sequences or the exit diameters which occurred during these tests. The different bottom opening sequences and exit diameters result from the inability to exactly duplicate the rupturing of the mylar diaphragm from test to test. Different opening sequences and exit diameters also would have produced the variations in acceleration levels measured. Because of the randomness of the freestream turbulence, its effects on the force data presented herein are difficult to determine and are unknown at this time.

Cylinder surface roughness has been shown by Achenback (Ref. 30) to locally affect the flow around a cylinder submerged in steady flow. Foreign matter on the surface of the cylinder was

controlled during this study by cleaning the smooth model (surface finish 16 by 10^{-6} inches, peak to peak) before each test with Methyl-Ethyl-Ketone (MEK) and a soft cloth. However, this cleaning did not remove surface roughness effects from the force data presented. The magnitude of these effects is unknown at this time.

Model end configurations have been shown by Bearman (Ref. 31) to locally affect the distribution of base pressure coefficients along the span of a circular cylinder submerged in steady flow. Bearman notes that local disturbances in the base pressure distribution resulted from the different span-wise flow levels which were determined to be a function of the model end configuration. Identical end conditions were used throughout this study so that all data presented should include the same end effects unless other flow parameters coupled with the model end configuration to vary the end effects.

Flow three-dimensionality was a subject of much interest during the recent 17th European Mechanics Colloquim as reported by Mair and Maull (Ref. 32). One of the Colloquim's major findings was that for a stationary model in steady flow, vortex shedding is not really two-dimensional, but varies along the span of the model, with changes in phase and possibly amplitude of the shed vortices. However, the effects of flow three-dimensionality on the data presented

herein are unknown at this time since the force measurement system was designed to measure the integrated forces along the entire model length.

The facility-related factors affecting experimental data can be shown to constitute sufficient error sources to cause a significant portion of the previously mentioned 20-percent data variation even if the effects of wall interference and model blockage on the force data are neglected. Because the investigation of model blockage and wall interference effects would have required the construction of additional specialized force measurement systems, these items were not investigated. Therefore, their contribution to the experimental data variation is unknown. An estimate of the error sources attributable to the other facility-related factors is given below.

The flow velocity used in obtaining the coefficient data shown is estimated to be accurate to within ± 3 percent. Since the square of the flow velocity is used in nondimensionalizing the force data, any error in flow velocity is magnified in the coefficient data presented in Figure V-14. This magnification means that a variation of approximately 6 percent in coefficient data is possible through errors in the velocity determination.

Accuracy of the force measurement system was not sufficiently high enough so that some errors were not developed in the

coefficient data presented. The small magnitude of the measured forces produced errors which were estimated at approximately 3 percent based on the results of static calibration. This error does not multiply the other error caused by velocity determination, but could continue to produce an overall error of approximately 9 percent. Thus 9 percent out of the 20-percent coefficient variation can be attributed to the method of velocity determination and the accuracy of the force measurement system.

The previous discussions of the parameters and error sources affecting the coefficient data presented herein do not invalidate its correlation with the steady flow drag coefficient, but rather serve to possibly explain the scatter in the unsteady flow drag coefficients. The general trend of the drag data appears to be very similar to the steady flow variation in this regime of the Reynolds number, 2×10^5 through 7.5×10^5 . This trend would not change should all error sources combine to give the maximum deviation. In this Reynolds number range, the overall velocity effects were found to dominate the acceleration effects for the model and facility used in this study. Based on the data presented herein, it may be deduced that a relationship may exist between the drag coefficients for circular cylinders in time-dependent and steady flows. This relationship may be obtained if the instantaneous Reynolds number is used in analyzing time-dependent flows. However, the Reynolds number range

investigated and the number of tests performed in this study do not provide a sufficient basis to positively establish a relationship between the drag coefficients for right-circular cylinders submerged in steady and time-dependent flows.

The previous paragraphs were concerned primarily with data obtained for the drag plane in the Reynolds number range of 2×10^5 to 7.5×10^5 . This range represented the region in which the output from the data reduction system met the author's sampling criterion. Below this range, the balance-model combination was producing high-frequency dynamic responses to the flow initiation that exceeded the force levels associated with the time-dependent flows. These dynamic responses had sufficiently damped at approximately 0.3 second to allow the data reduction system output to meet the sampling criterion. This time corresponds to a Reynolds number of approximately 2×10^5 . Figure V-12 does indicate, however, that some small effects of this dynamic response are present throughout each individual test. This can be seen by observing the increasing number of oscillatory patterns which appear in the force data of Figure V-12 as the filter cutoff frequency is increased. Because the Reynolds number range below 2×10^5 represents the region which inviscid two-dimensional theory could be expected to best predict the drag forces, no comparison of the theoretical and experimental results

were made. To accomplish such a comparison effectively, a faster rate of data sampling would have to be used and the measurement system's dynamic response effects removed from the force data.

An unsuccessful attempt was made to correlate the force data with the photographic data. The primary reason for this failure was that during the period when vortex shedding was well established, the balance dynamic response was dominating the force data. When the response had sufficiently damped to allow force determination, the wake behind the cylinder had become extremely turbulent with no definite frequency of vortex shedding recognizable.

Comparisons of the data presented herein with data obtained by other investigators were attempted. Special efforts were made to compare these experimental data with data obtained by the investigators (Refs. 4 through 9) found to be most helpful in understanding the complex flow phenomena. Most of the referenced investigations were conducted in steady flow with an oscillating model. However, in those cases where a stationary model and time-dependent flow were used, either the test Reynolds number was too low or the available reports contained insufficient information for the calculation of those parameters found important in this investigation. Table V-1 summarizes the attempts at data comparison with the primary reason for failure in each case given.

TABLE V-1. COMPARISON FAILURE SUMMARY

INVESTIGATOR	TYPE OF TEST	COMMENT
Schutzenhofer (Ref. 4)	Time-dependent flow with stationary model	No force measurement
Sarpkaya (Refs. 5. and 11)	Time-dependent flow with stationary model	Information contained in available reports insufficient for calculating parameters found important in these tests
Pearce (Ref. 6)	Time-dependent flow with stationary model	Reynolds number $< 10^4$
Jones, et al, (Ref. 7)	Steady flow with stationary and oscillating model	Partial model balance system
Bishop and Hasson (Ref. 8)	Steady flow with oscillating model	Reynolds number $< 2 \times 10^5$
Keefe (Ref. 9)	Steady flow with stationary model	Reynolds number $< 2 \times 10^5$ primarily concerned with acoustics

CHAPTER VI

CONCLUSIONS AND RECOMMENDATIONS

A. Conclusions

An experimental investigation has been conducted in which measurements were made of the unsteady forces imposed on a right-circular cylinder submerged in time-dependent flows. Conclusions reached as a result of this research effort are as follows:

- (1) The drag coefficients for a circular cylinder in time-dependent flows appear to be correlated with steady flow drag coefficients in the instantaneous Reynolds number range of 2×10^5 to 7.5×10^5 ; i.e., the useful Reynolds number range of this investigation.
- (2) Two-dimensional inviscid theory cannot be used to accurately predict the unsteady forces since a variation with instantaneous Reynolds number is indicated by these results.
- (3) A simple and inexpensive force measurement system can be constructed to measure the unsteady loads imposed by the time-dependent flows.

- (4) A means of extracting or eliminating the balance-model combination dynamic response effects from the force data must be implemented if accurate force measurements are to be made at low Reynolds numbers in impulsively started time-dependent flows.
- (5) A modified version of the hydrogen bubble technique can be used to obtain movies of the general qualitative features of the complex flow patterns surrounding the cylinder.

B. Recommendations

The following recommendations are made with regard to continuing research into the flow fields surrounding bluff bodies:

- (1) The bibliographical literature search be continued to maintain awareness of the efforts and results of other investigators.
- (2) Dynamic calibration of the balance-model combination used in this analysis be accomplished to verify the calibration constants.
- (3) Additional testing of the model configuration used in this investigation be accomplished to verify the trends of the data presented herein.

- (4) The effects of model end configurations on the unsteady forces be evaluated.
- (5) The effects of cylinder surface roughness on minimum drag coefficients be evaluated using one-piece models of aluminum machined to exact surface roughness.
- (6) Different diameters of cylinders be tested to determine if any model scale or blockage effects can be delineated.
- (7) Methods of determining the effects of tunnel wall interference be investigated.

REFERENCES

1. "Meeting on Ground Wind Loads Problems in Relation to Launch Vehicles," NASA TMX-57779, Compilation of Papers Presented at the NASA Langley Research Center, June 7-8, 1966
2. "Proceedings of Symposium on Aeroelastic and Dynamic Modeling Technology," U.S. Air Force Report No. RTD-TDR-63-4197, Office of Technical Services, U.S. Department of Commerce, Washington, D. C., 1964
3. "Proceedings of the National Symposium on Winds for Aerospace Vehicle Design," U.S. Air Force Report AFCRL-62-273(I), Office of Technical Services, U.S. Department of Commerce, Washington, D. C., March 1962
4. Schutzenhofer, L. A., "Development of an Unsteady Flow Apparatus and the Investigation of Unsteady Pressures on a Circular Cylinder in the Apparatus," M. S. Thesis, The University of Alabama, University, Alabama, 1969
5. Sarpkaya, T., "Unsteady Flow Over Bluff Bodies," Developments in Mechanics, Proc. 8th Midwestern Mechs. Conf., Pergomon Press, p. 45, 1965
6. Pearce, B. R., "An Experimental Study of the Unsteady Forces Causing Vortex-Excited Oscillations of a Circular Cylinder," M.S. Thesis, Massachusetts Institute of Technology, Cambridge, Massachusetts, 1969
7. Jones, G. W., J. J. Cincotta, and R. W. Walker, "Aerodynamic Forces on a Stationary and Oscillating Circular Cylinder at High Reynolds Numbers," NASA TR-R-300, February 1969
8. Bishop, R. E. D. and A. Y. Hassan, "The Lift and Drag Forces on a Circular Cylinder Oscillating in a Flowing Fluid," Proc. Roy. Soc., A277, p. 51, 1964

9. Keefe, R. T., "An Investigation of the Fluctuating Forces Acting on a Stationary Circular Cylinder in a Subsonic Stream and of the Associated Sound Field," University of Toronto Inst. Aero-Physics Dept. Report No. 76, 1961
10. von Karman, T. and H. Rubach, "Uber Ien Mechanismus dis Flussig Keits and Luflwiderstandes," Phys. Zs., Bd ____, Heft 2, January 1912
11. Sarpkaya, T., "Lift, Drag, and Added-Mass Coefficients for a Circular Cylinder Immersed in a Time-Dependent Flow," J. App. Mech., Trans. of ASME, March 1963
12. Phillips, O. M., "The Intensity of Aeolion Tones," J. Fluid Mech., Vol. 1, 1956
13. Gerrard, J. H., "Numerical Computation of the Magnitude and Frequency of the Lift on a Circular Cylinder," Phil. Trans. Roy. Soc., London, Series A, Vol. 261, No. 1118, 1967
14. Lott, R. A. and et al., "Analysis of Dynamic Model Test Data from Saturn Ground Winds," LMSC/HRED D/149478, Lockheed Missiles and Space Company, December 1969
15. Halfman, R. L., Dynamics, Particles, Rigid Bodies, and Systems, Addison-Wesley Pub. Co., Reading, Mass., p. 298, 1962
16. Timoshenko, S., Vibration Problems in Engineering, Third Edition, D. Van Nostrand Company, Inc., Princeton, New Jersey, 1955
17. Jones, A. T., "Vibrations of Beams Immersed in a Liquid," Experimental Mechanics, J. Soc. Exp. Stress Anal., February 1970.
18. Holt, J. F., "STL BEAM Program; Lateral Vibrations of Single Beams," AS-0308, Space Technology Laboratories, October 1959
19. "Wind Tunnel Instrumentation and Operation, Handbook of Supersonic Aerodynamics," Navord Report 1488, Vol. 6, Section 6, January 1961

20. Schraub, F. A. and et al., "Use of Hydrogen Bubbles for Quantitative Determination of Time-Dependent Velocity Fields in Low-Speed Water Flows," J. Basic Engr., Trans of ASME, p. 429, June 1965
21. Special Issue on Fast Fourier Transform, Audio and Electro-acoustics, Trans of IEEE, Vol. Au-17, No. 2, June 1969
22. Cochran, W. T. and et al., "What is the Fast Fourier Transform," Proc. of IEEE, Vol. 55, No. 10, October 1967
23. Brigham, E. O. and R. E. Morrow, "The Fast Fourier Transform," IEEE Spectrum, p. 63, December 1967
24. "Fast Fourier Transform as a Power Spectral Analysis Program," NASA Technical Brief 69-10434, September 1969
25. Sarpkaya, T. and C. J. Garrison, "Vortex Formation and Resistance in Unsteady Flow," J. Appl. Mech., Trans. of ASME, p. 16, 1963
26. Delaney, N. K. and N. E. Sorensen, "Low-Speed Drag of Cylinders of Various Shapes," NACA TN 3038, November 1953
27. Schmidt, L. V., "Measurements of Fluctuating Air Loads on a Circular Cylinder," J. Aircraft, Vol. 1, p. 49, January-February 1965
28. "Experimental Investigation of the Flow Field Surrounding a Circular Cylinder Submerged in Accelerating Flows," 16-millimeter film on file at UAH Fluid and Thermal Engineering Department, Huntsville, Alabama
29. Surry, D., "The Effect of High Intensity Turbulence on the Aerodynamics of a Rigid Circular Cylinder at Subcritical Reynolds Number," USAF Technical Report AFFDL-TR-69-88, March 1970
30. Achenback, E., "Influence on Surface Roughness on the Cross-Flow around a Circular Cylinder," J. Fluid Mech., Vol. 46, p. 321, 1971

31. Bearman, P. W., "On Vortex Shedding from a Circular Cylinder in the Critical Reynolds Number Regime," J. Fluid Mech., Vol. 37, p. 577, 1969
32. Mair, W. A. and D. J. Maull, "Bluff Bodies and Vortex Shedding"- A report on Euromech 17, J. Fluid Mech., Vol. 45, p. 209, 1971

APPENDIX A.

THEORETICAL HYDRODYNAMIC MODEL

A two-dimensional inviscial model was developed for use in predicting the test section size and model diameter effects on the acceleration-induced forces imposed on a rigid right-circular cylinder submerged in a time-dependent flow. To determine these effects, the development of two variations of the theoretical hydrodynamic model was necessary. One variation represented an accelerating infinite-length cylinder in a bounded stationary flow. The other variation represented a stationary infinite-length cylinder past which a bounded fluid was accelerated. Figure A-1(a) shows the coordinate system used for the moving cylinder case while Figure A-1(b) shows the coordinate system employed in the stationary cylinder case.

Stationary Cylinder Case

To develop the theoretical model, it was necessary to define the complex potential, Ω . The complex potential can be determined by considering an infinite series of equal-strength doublets located equidistant apart along the y axis. The complex potential for this arrangement of axes and doublets is given by

$$\Omega_1 = \frac{\mu}{2\pi} \sum_{k=-\infty}^{+\infty} \frac{1}{z - k bi} \quad (\text{A-1})$$

where

μ - moment of the doublet

b - distance between the doublets

z - complex coordinate, $x + i y$

k - a summation index.

Recalling that the partial fraction expansion

$$\cot z = \sum_{k=-\infty}^{k=+\infty} \frac{1}{z - k} \quad (\text{A-2})$$

it follows that

$$\Omega_1 = \frac{\mu}{2 bi} \cot \frac{\pi z}{bi} = \frac{\mu}{2b} \coth \frac{\pi z}{b} \quad (\text{A-3})$$

The symmetric distribution of the doublets assures that the straight lines

$$y = (2k + 1) \frac{b}{2} \quad (k = \dots -2, -1, 0, 1, 2 \dots) \quad (\text{A-4})$$

are streamlines. Streamlines have properties which allow their replacement by fixed walls (at $y = \pm kb$) without the flow being changed in any way. The symmetry of the doublets also allows the superposition of a uniform translatory flow with the complex potential,

$$\Omega_2 = Uz \quad (\text{A-5})$$

on to the flow created by the doublets. The total complex potential for the complete flow is given by

$$\Omega_T = \Omega_1 + \Omega_2 = Uz + \frac{\mu}{2b} \coth \frac{\pi z}{b} \quad (\text{A-6})$$

The complex velocity is defined as the derivative of the complex potential, Ω , taken with respect to the complex coordinate, z . Performing this operation on Equation A-6 yields, for the complex velocity,

$$\frac{d\Omega_T}{dz} = U - \frac{\pi\mu}{2b^2} \frac{1}{\sinh^2 \frac{\pi z}{b}} \quad (\text{A-7})$$

Now at the stagnation points, $\frac{d\Omega_T}{dz}$ is zero, thus from Equation A-7

$$\sinh^2 \frac{\pi z}{b} = \frac{\mu\pi}{2b^2 U} \quad (\text{A-8})$$

Two stagnation points are located on the real axis equidistant from the coordinate system origin. For these two points, the y-axis coordinate is zero, thus

$$|z| = \frac{b}{\pi} \sinh^{-1} \left(\frac{\mu\pi}{2b^2 U} \right) = a \quad (\text{A-9})$$

where a is the radius of the cylinder represented by a single doublet.

Therefore, for the condition described,

$$\sinh^2 \frac{\pi a}{b} = \frac{\mu\pi}{2b^2 U} \quad (\text{A-10})$$

which yields for the magnitude of the moment of the doublets,

$$\mu = \frac{2b^2 U}{\pi} \sinh^2 \frac{\pi a}{b} \quad (A-11)$$

Hence, the equation for the complex potential becomes

$$\Omega_T = Uz + \frac{bU}{\pi} \sinh^2 \frac{\pi a}{b} \coth \frac{\pi z}{b} \quad (A-12)$$

Recalling that

$$\Omega_T = \phi + i\psi \quad (A-13)$$

where

ϕ - velocity potential

ψ - stream function.

Equation A-12 can be solved for the velocity potential by expanding $\coth \pi z/b$ through the use of the following:

$$\coth \frac{\pi z}{b} = \coth \frac{\pi r e^{i\theta}}{b} \quad (A-14)$$

and

$$\coth \frac{\pi r e^{i\theta}}{b} = \frac{b e^{-i\theta}}{r \pi} + \frac{r \pi e^{i\theta}}{3b} + \sum_3^{\infty} C_n' e^{i(2n-3)\theta} \quad (A-15)$$

where the coefficients C_n' are functions of $\left(\frac{\pi r}{b}\right)^{2n-3}$, $n=3, 4, 5 \dots$

Substituting Equation A-15 into Equation A-12 yields

$$\Omega_T = Uz + \frac{bU}{\pi} \sinh^2 \left(\frac{\pi a}{b} \right) \left[\frac{b \cos \theta}{a \pi} + \frac{a \pi}{3b} e^{i\theta} \right. \\ \left. + \sum_3^{\infty} C_n' e^{i(2n-3)\theta} \right] \quad (A-16)$$

where θ is the angle definition in Figure 4-1. Now using De Moivre's theorem and taking the velocity potential, ϕ , as the real part of the expansion of Equation A-16 gives

$$\phi = UX + \frac{bU}{\pi} \sinh^2 \left(\frac{\pi a}{b} \right) \left[\frac{b \cos \theta}{a \pi} + \frac{a \pi}{3b} e^{i\theta} \right. \\ \left. + \sum_3^{\infty} C_n' \cos (2n-3) \theta \right] \quad (A-17)$$

Now following Robertson¹, the force on the cylinder can be obtained using the unsteady Bernoulli relationship in terms of an axes system moving with a velocity, U . This relationship is given by

$$\int \frac{dp}{\rho} + \frac{q^2}{2} + gh + \frac{\partial \phi}{\partial t} - \frac{V^2}{2} = \Pi(t) \quad (A-18)$$

where

dp - pressure differential

ρ - fluid density

g - acceleration of gravity

¹Robertson, James M., "Hydrodynamics in Theory and Application", Prentice-Hall, Inc., Englewood Cliffs, New Jersey, pp. 156-158, 1965

- h - height above some datum
 q - local flow velocity
 ϕ - velocity potential in a fixed frame
 V - velocity of a point in a fixed reference frame in terms of the moving axes
 $\Pi(t)$ - an independent function of time.

For a constant density fluid where gravitational effects are negligible and the body is not rotating, Equation A-18 becomes

$$\frac{P}{\rho} + \frac{\partial \phi}{\partial t} = \frac{P_0}{\rho} \quad (\text{A-19})$$

since at large distances, the fluid is moving at a steady velocity with a pressure P_0 .

Now, letting P_s represent the steady portion of the pressure and P_u the unsteady pressure (i. e., that associated with $\frac{\partial U}{\partial t} = \frac{dU}{dt}$), Equation A-19 becomes

$$P_u = P - P_s = \rho \frac{\partial \phi}{\partial t} \quad (\text{A-20})$$

Equation A-17 yields for the time rate of change of velocity potential,

$$\frac{\partial \phi}{\partial t} = \frac{\partial U}{\partial t} \left\{ X + \frac{b}{\pi} \sinh^2 \left(\frac{\pi a}{b} \right) \left[\frac{b \cos \theta}{a \pi} + \frac{a \pi}{3b} \cos \theta + \sum_3^{\infty} C_n' \cos (2n-3) \theta \right] \right\} \quad (\text{A-21})$$

Substituting Equation A-21 into Equation B-20 yields

$$P_u = \rho \frac{\partial U}{\partial t} \left\{ X + \frac{b}{\pi} \sinh^2 \left(\frac{\pi a}{b} \right) \left[\frac{b \cos \theta}{a \pi} + \frac{a \pi}{3b} \cos \theta + \sum_3^{\infty} C_n' \cos (2n-3) \theta \right] \right\}. \quad (\text{A-22})$$

The force, F , due to unsteady motion is defined as the integral of the unsteady pressure over the surface of the cylinder or

$$F = \int_S P_u \cos \theta \, dS = \int_0^{2\pi} P_u \cos \theta \, a \, d\theta \quad (\text{A-23})$$

since

$ds = a \, d\theta$ - differential surface area of a unit length of the cylinder

θ - the angle defined in Figure A-1.

Using Equation A-23 in conjunction with Equation A-22 yields

$$F = \int_0^{2\pi} \left\{ X \cos \theta + \frac{b}{\pi} \sinh^2 \left(\frac{\pi a}{b} \right) \left[\frac{b \cos^2 \theta}{a \pi} + \frac{a \pi}{3b} \cos^2 \theta + \sum_3^{\infty} C_n' \cos (2n-3) \theta \cos \theta \right] \right\} \times \left\{ \rho a \frac{\partial U}{\partial t} \, d\theta \right\}. \quad (\text{A-24})$$

Performing the indicated integration on θ , and letting

$$\frac{dU}{dt} = \frac{\partial U}{\partial t}$$

yields for the force

$$F = \rho \frac{dU}{dt} \left\{ \pi a^2 + \frac{b^2}{\pi} \sinh^2 \left(\frac{\pi a}{b} \right) \left[1 + \frac{a^2 \pi}{3b^2} \right] \right\} \quad (\text{A-25})$$

since

$$\int_0^{2\pi} \cos (2n-3) \theta \cos \theta \, d\theta = 0, \quad n \text{ greater than } 2. \quad (\text{A-26})$$

Thus the force on a unit length of a stationary infinite-length circular cylinder is given by

$$F = \rho \pi a^2 \left[1 + \left(\frac{1}{3\pi} + \frac{b^2}{a^2 \pi^2} \right) \sinh^2 \left(\frac{\pi a}{b} \right) \right] \frac{dU}{dt} . \quad (\text{A-27})$$

Equation A-27 can be used to determine the force on the stationary cylinder provided the fluid velocity's time rate of change and the geometric characteristics of the model and test section are known.

Moving Cylinder Case

The complex potential for this variation of the theoretical hydrodynamic model can be obtained by the methods explained in the stationary cylinder case (Equation A-6) with the superposition of the uniform flow being omitted. This yields

$$\Omega_T = \frac{\mu}{2b} \coth \frac{\pi z}{b} . \quad (\text{A-28})$$

Following the stationary cylinder case procedure, the velocity potential is obtained as

$$\phi = \frac{bU}{\pi} \sinh^2 \left(\frac{\pi a}{b} \right) \left[\frac{b \cos \theta}{a\pi} + \frac{a\pi}{3b} \cos \theta + \sum_3^{\infty} C_n' \cos(2n-3)\theta \right] \quad (\text{A-29})$$

Again the unsteady pressure's contribution to the force on the cylinder can be obtained by using

$$P_u = P - P_s = \rho \frac{\partial \phi}{\partial t} \quad (\text{A-30})$$

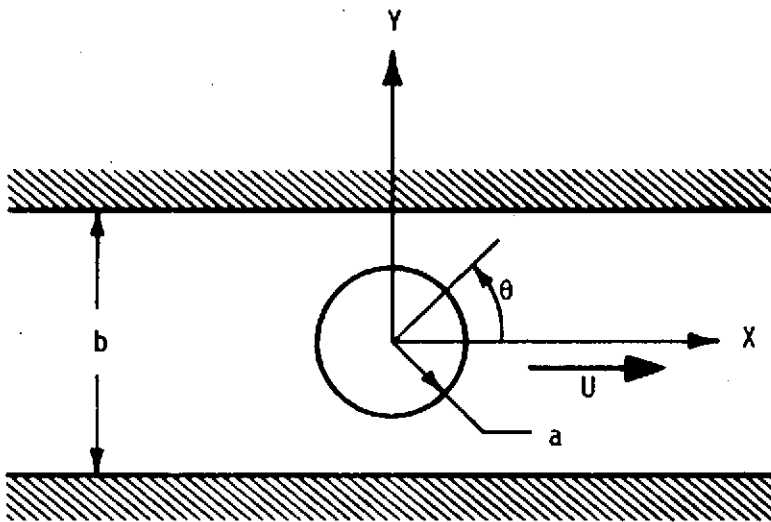
The use of the velocity potential of Equation A-29 in conjunction with Equation A-30 yields

$$P_u = \rho \left\{ \frac{b}{\pi} \sinh^2 \left(\frac{\pi a}{b} \right) \left[\left(\frac{b}{a\pi} + \frac{a\pi}{3b} \right) \cos \theta + \sum_3^{\infty} C_n' \cos(2n-3)\theta \right] \right\} \quad (\text{A-31})$$

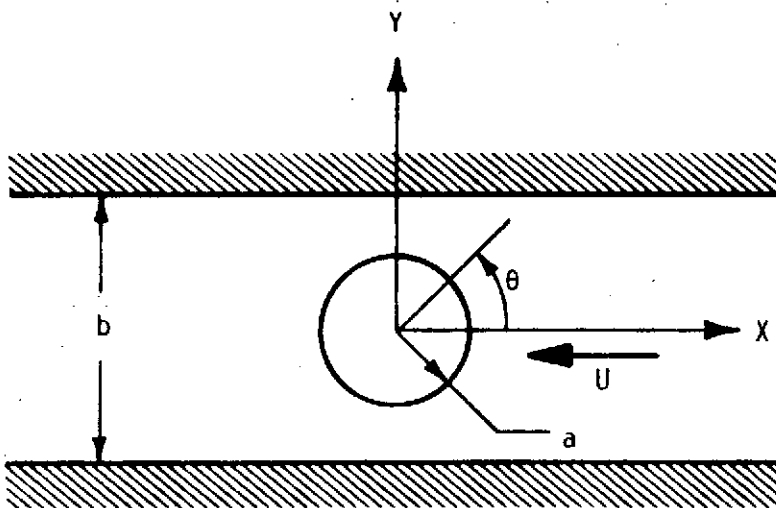
Substituting Equation A-31 into Equation A-23 yields the following when the indicated integration is performed

$$F = \rho \pi a^2 \left[\left(\frac{1}{3\pi} + \frac{b^2}{a^2 \pi^2} \right) \sinh^2 \left(\frac{\pi a}{b} \right) \right] \frac{dU}{dt} \quad (\text{A-32})$$

Examination of Equations A-32 and A-27 shows a difference of $\rho \pi a^2 \frac{dU}{dt}$ in the indicated force levels. This represents the magnitude of the fluid displaced by the cylinder multiplied by the time rate of change of fluid velocity.



(a) MOVING CYLINDER CASE



(b) STATIONARY CYLINDER CASE

FIGURE A-1. COORDINATE SYSTEMS FOR THEORETICAL HYDRODYNAMIC MODEL

APPENDIX B

**ENGINEERING DRAWINGS OF MODEL,
BALANCE, AND MODEL ASSEMBLY**

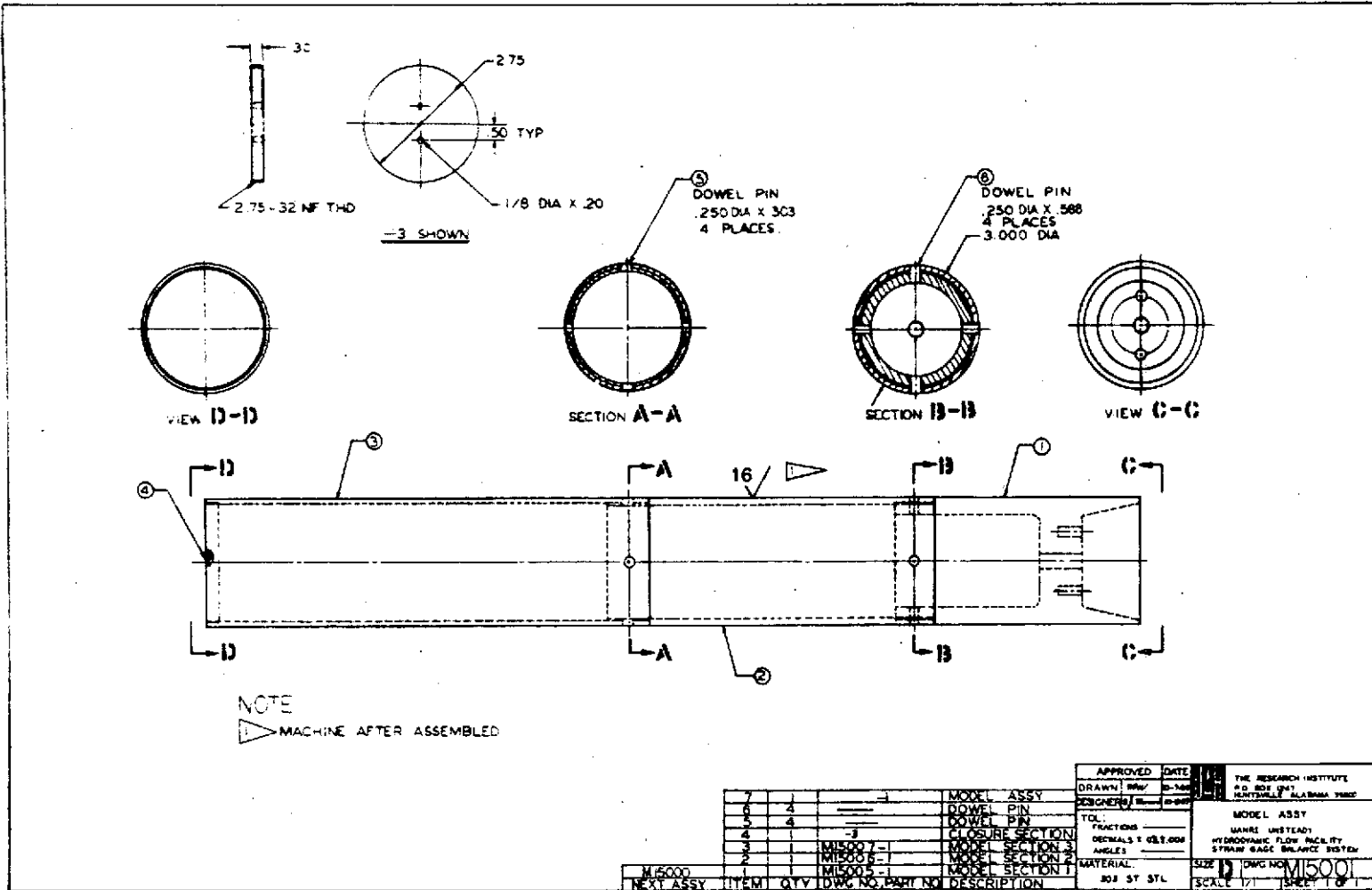


FIGURE B-1. ENGINEERING DRAWING OF MODEL ASSEMBLY.

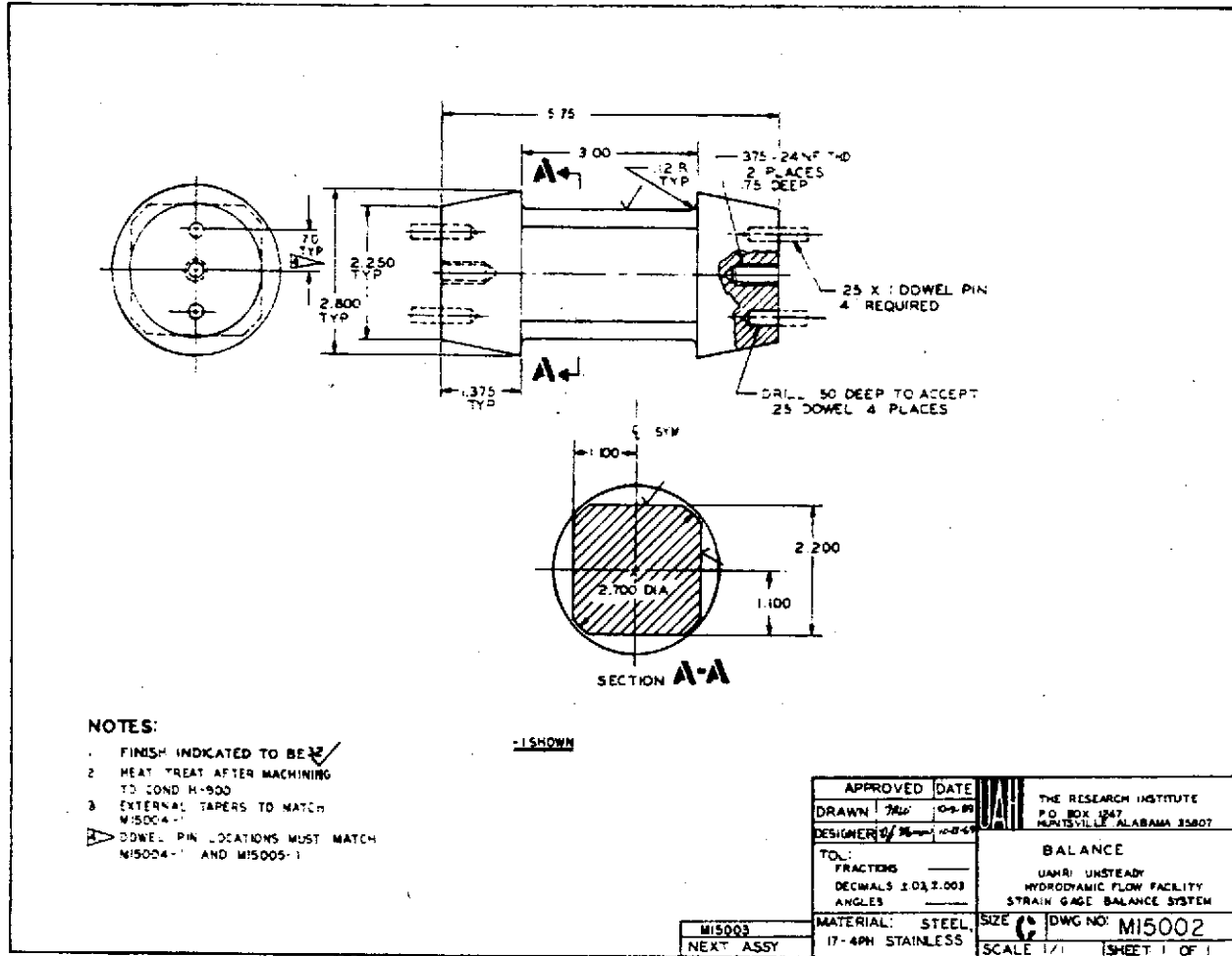


FIGURE B-2. ENGINEERING DRAWING OF BALANCE SECTION

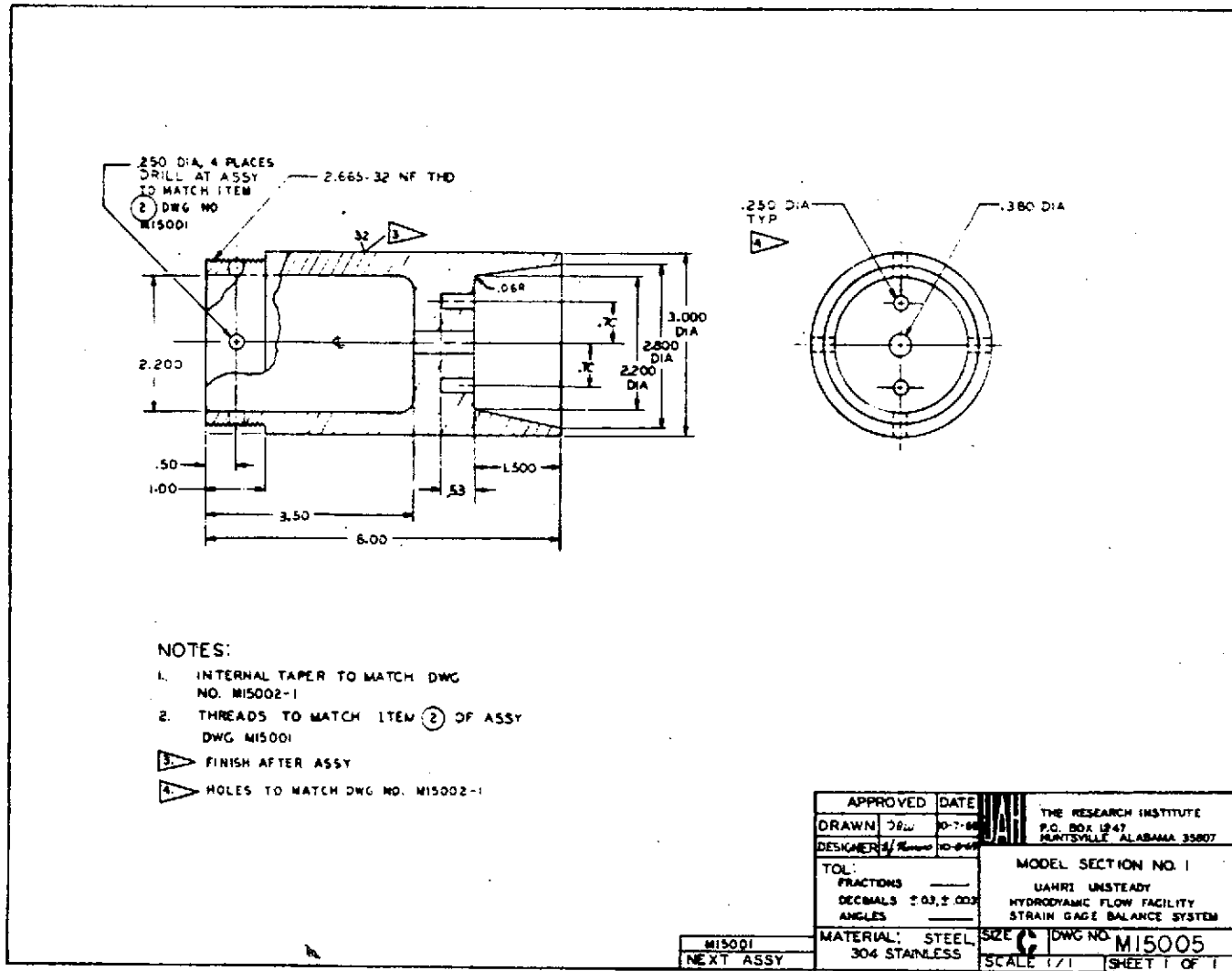


FIGURE B-3. ENGINEERING DRAWING OF MODEL SECTION NUMBER ONE

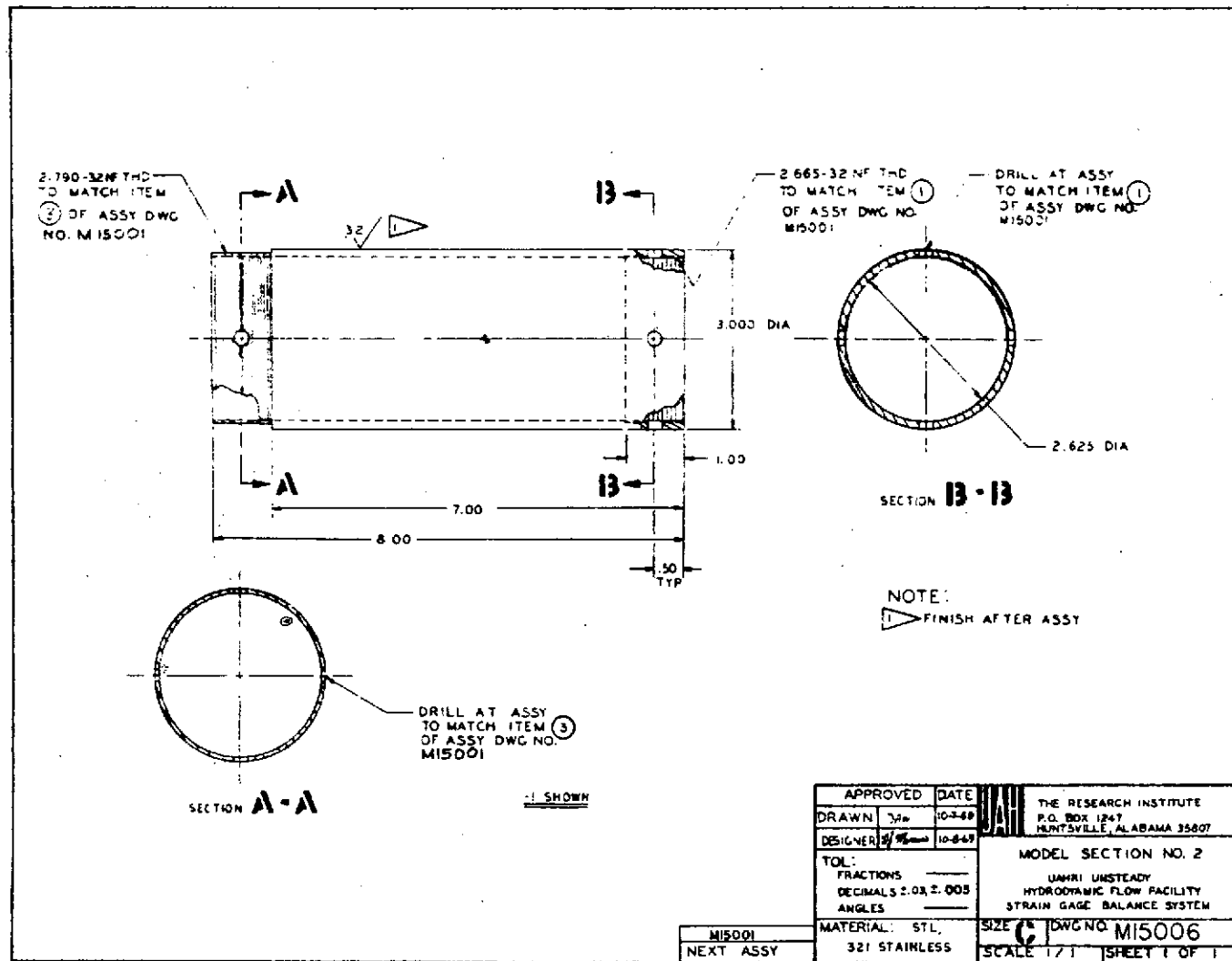


FIGURE B-4. ENGINEERING DRAWING OF MODEL SECTION NUMBER TWO

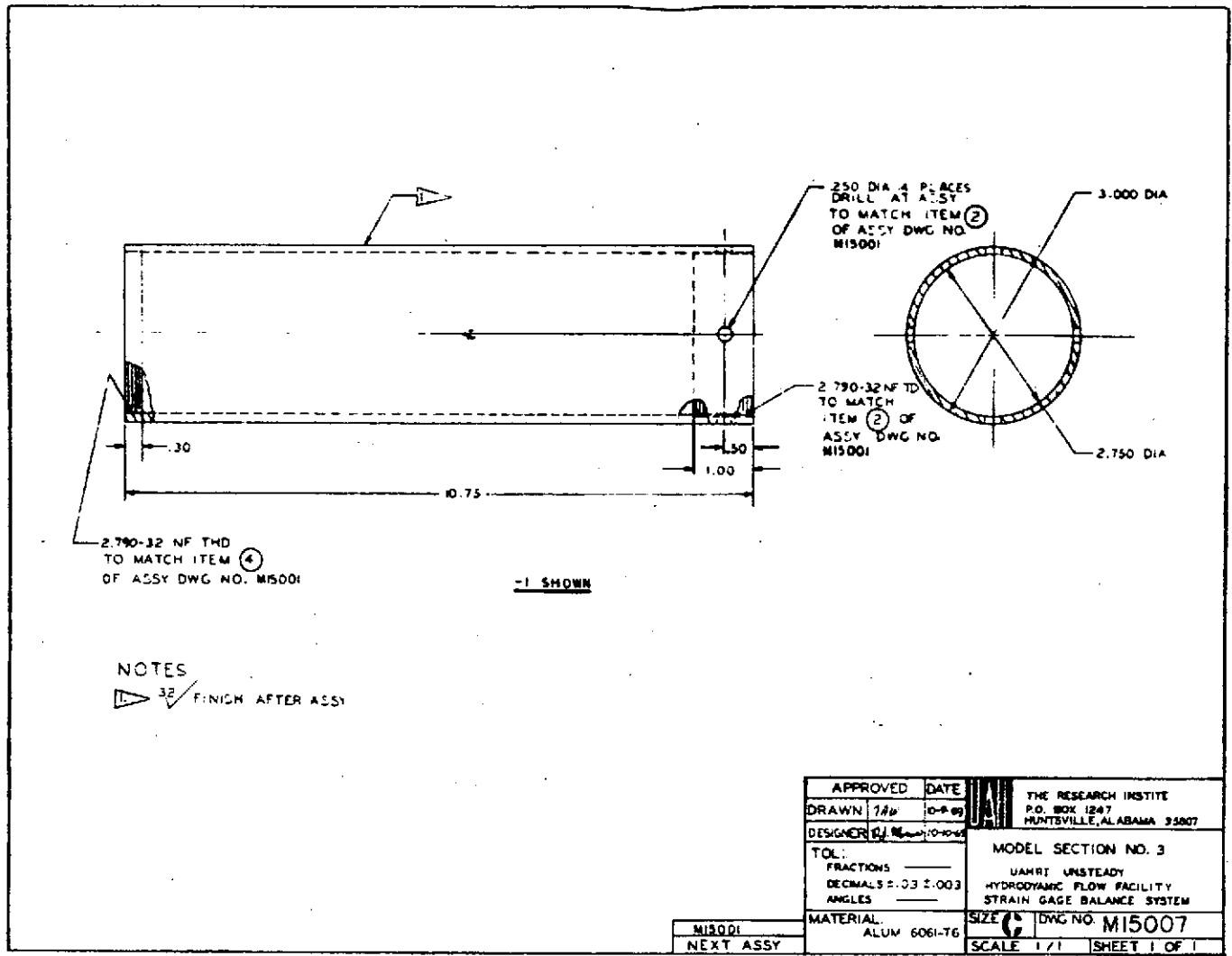


FIGURE B-5. ENGINEERING DRAWING OF MODEL SECTION NUMBER THREE

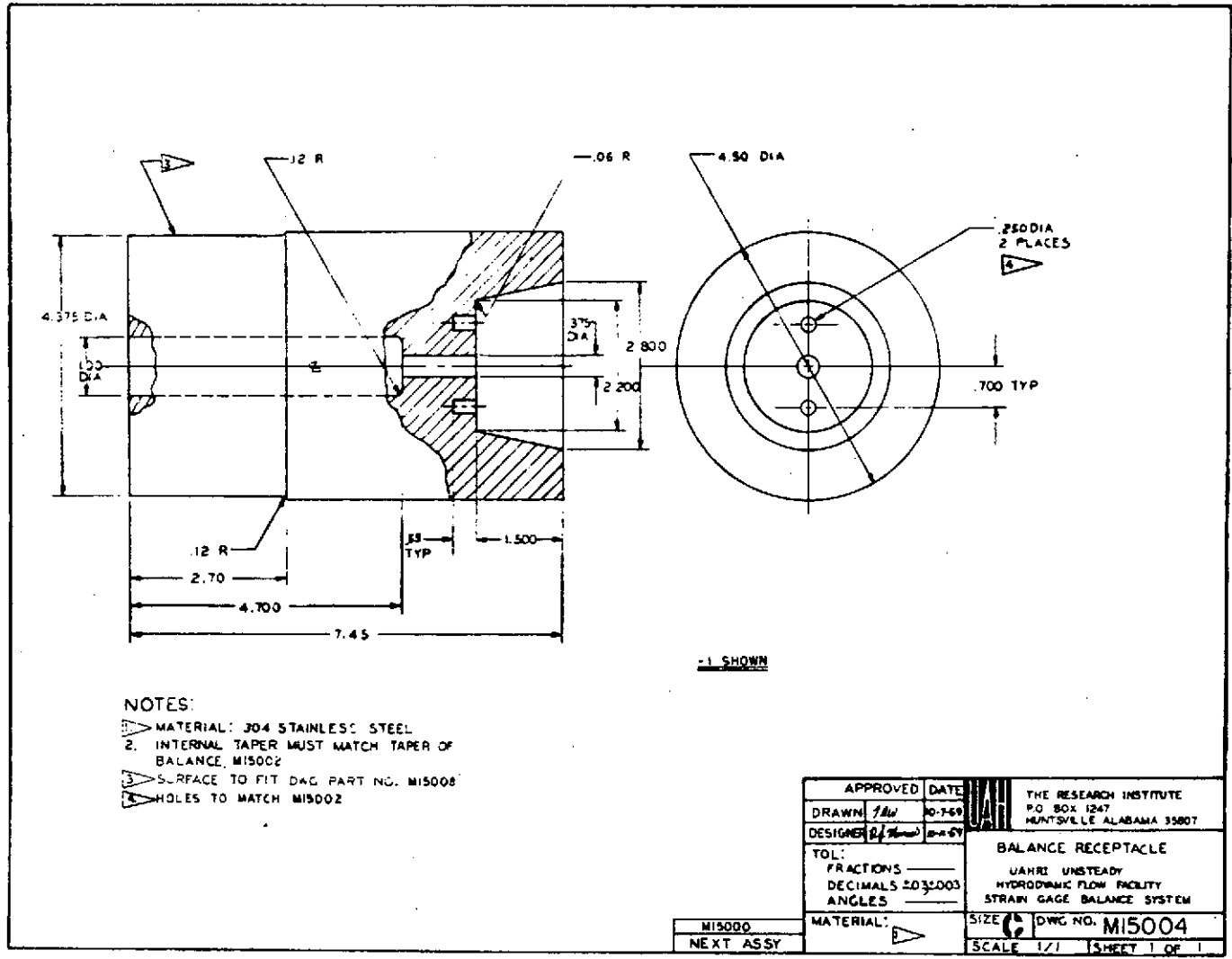


FIGURE B-6. ENGINEERING DRAWING OF SUPPORT BALANCE RECEPTACLE

APPENDIX C

CALIBRATION PROCEDURE AND RESULTS

The employment of Wheatstone Bridges in conjunction with the two-moment method of force determination in a force measurement system requires calibration to accurately determine force levels. This calibration is necessary to determine the proper factors to convert the force measurement system's output from volts to pounds of force at the model's midpoint. The static calibration procedure used in determining the force measuring system conversion factors is similar to that used in several wind tunnels to calibrate balances used for sting-mounted model applications. The particular procedure used assumes that only first-order interaction effects will be accounted for. First-order interaction effects result from such items as gage-factor variations, variations in gage locations, and balance cross-sectional area nonuniformity. Nonlinear interaction effects (higher order) result from such items as large deflections and mechanical interference.

Equations C-1 through C-4 are first-order interaction equations used to determine the bending moments at the four gage locations (two lift, two drag) shown in Figure C-1.

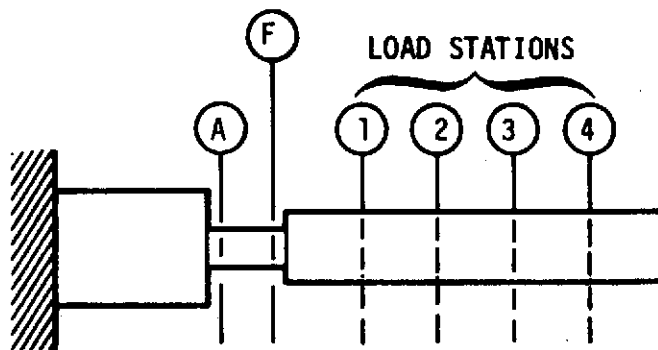


FIGURE C-1. CANTILEVERED BEAM WITH TWO STRAIN GAGE BRIDGES (A AND F)

$$M_1 = K_1 X_1 + \frac{\partial M_1}{\partial M_2} M_2 + \frac{\partial M_1}{\partial M_3} M_3 + \frac{\partial M_1}{\partial M_4} M_4 \quad (C-1)$$

$$M_2 = \frac{\partial M_2}{\partial M_1} M_1 + K_2 X_2 + \frac{\partial M_2}{\partial M_3} M_3 + \frac{\partial M_2}{\partial M_4} M_4 \quad (C-2)$$

$$M_3 = \frac{\partial M_3}{\partial M_1} M_1 + \frac{\partial M_3}{\partial M_2} M_2 + K_3 X_3 + \frac{\partial M_3}{\partial M_4} M_4 \quad (C-3)$$

$$M_4 = \frac{\partial M_4}{\partial M_1} M_1 + \frac{\partial M_4}{\partial M_2} M_2 + \frac{\partial M_4}{\partial M_3} M_3 + K_4 X_4 \quad (C-4)$$

where

M_1 - bending moment at aft drag station (A), in-lb

M_2 - bending moment at forward drag station (F), in-lb

M_3 - bending moment at aft lift station (A), in-lb

M_4 - bending moment at forward lift station (F), in-lb

K_1 - drag bridge conversion factor, aft drag station, $\frac{\text{in-lb}}{V}$

K_2 - drag bridge conversion factor, forward drag station, $\frac{\text{in-lb}}{V}$

K_3 - lift bridge conversion factor, aft lift station, $\frac{\text{in-lb}}{V}$

K_4 - lift bridge conversion factor, forward lift station,
 $\frac{\text{in-lb}}{V}$

X_1 - aft drag bridge output, V

X_2 - forward drag bridge output, V

X_3 - aft lift bridge output, V

X_4 - forward lift bridge output, V

$\frac{\partial M_{1,2,3, \text{ or } 4}}{\partial M_{1,2,3, \text{ or } 4}}$ interaction coefficient, where
1, 2, 3, or 4 indicates either lift
or drag plane

Cursory examination of Equations C-1 through C-4 indicates an iterative procedure would be necessary to determine solutions if the conversion factors were known. Fortunately, two terms in each equation are repetitive in this particular application and can be set to zero. This results from all gage locations being on a single sensing element; therefore, whatever affects one gage affects all gages, but in different magnitudes. This is different from conventional balances which usually have separate elements for sensing perpendicular applied force systems. Equations C-5 through C-8 result from this simplification.

$$M_1 = K_1 X_1 + \frac{\partial M_1}{\partial M_4} M_4 \quad (\text{C-5})$$

$$M_2 = K_2 X_2 + \frac{\partial M_2}{\partial M_4} M_4 \quad (\text{C-6})$$

$$M_3 = K_3 X_3 + \frac{\partial M_3}{\partial M_1} M_1 \quad (C-7)$$

$$M_4 = K_4 X_4 + \frac{\partial M_4}{\partial M_2} M_2 \quad (C-8)$$

An iterative procedure still is necessary to solve these equations; however, the magnitude of the iteration has been drastically reduced.

The procedure for determining the remaining conversion factors is as follows:

A series of known "dead" weights is placed in ascending and descending order on the model at several known locations and the resulting system outputs are recorded. Plots of system output¹ versus applied force can then be constructed for all gage locations as shown in Figure C-2.

"Best fit" curves can be drawn through the points for each load station and their slope, in terms of system output per pound of applied force, can be determined. Plots using these slopes and the known load stations can then be constructed as shown in Figure C-3. From these plots the primary conversion factors, K_1 through K_4 , can be obtained since they are the reciprocals of the "best fit" curves shown in Figure C-3. The interaction conversion factors also can be

¹System output magnitudes will be different between the loaded plane and the plane normal to it since the normal plane output represents only interaction effects.

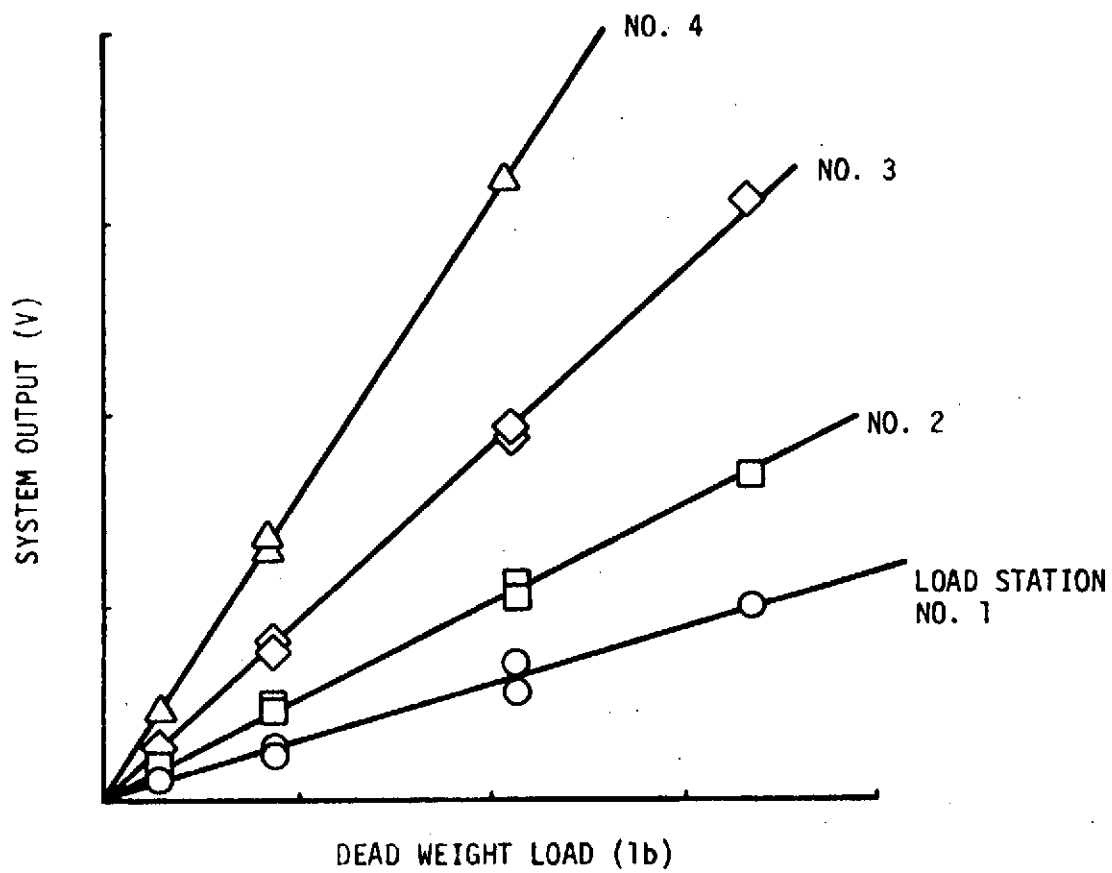


FIGURE C-2. SYSTEM OUTPUT AS A FUNCTION OF DEAD WEIGHT LOAD

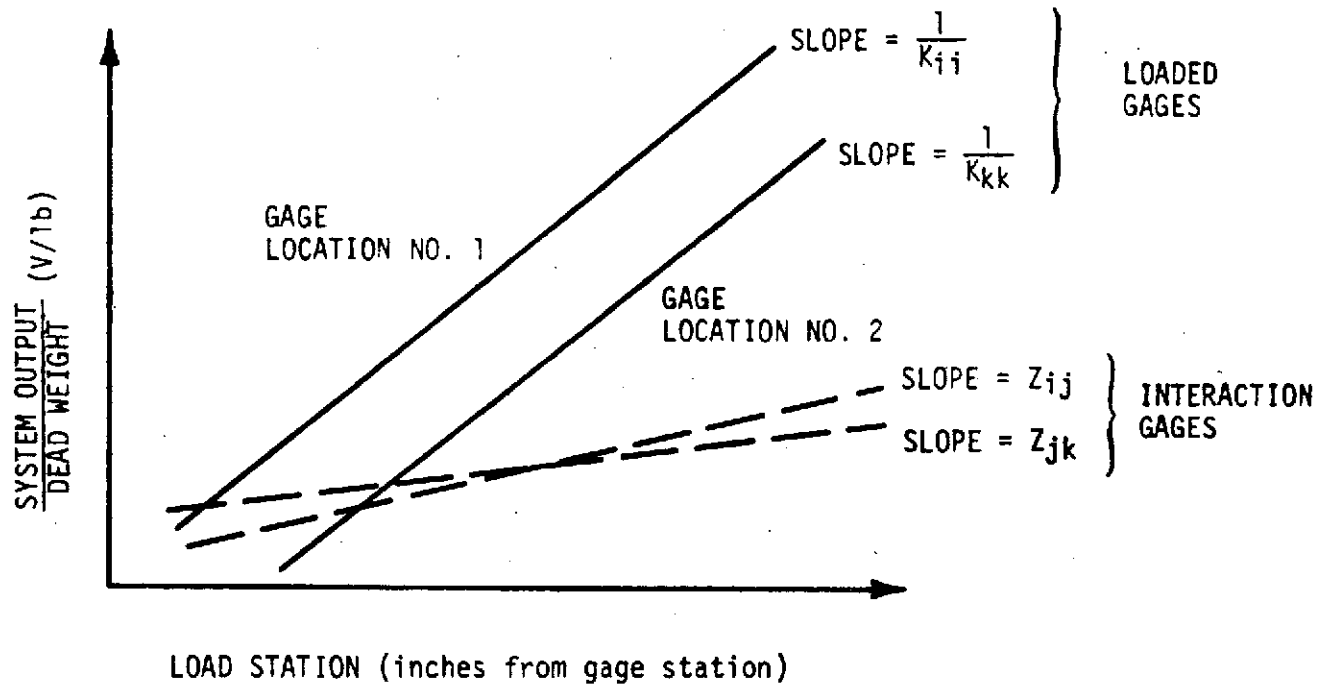


FIGURE C-3. UNIT SYSTEM OUTPUT AS A FUNCTION OF LOAD STATION

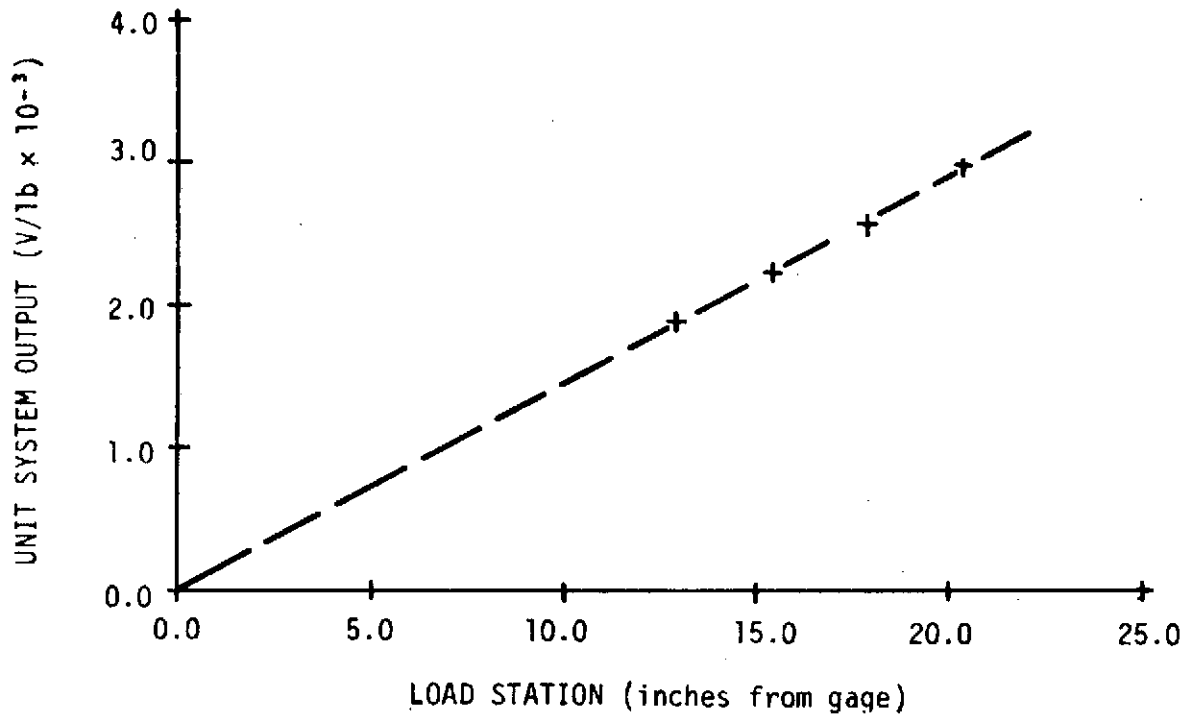
determined from these plots since they are defined as

$$\frac{\partial M_i}{\partial M_j} = K_{ik} \times Z_{jk}$$

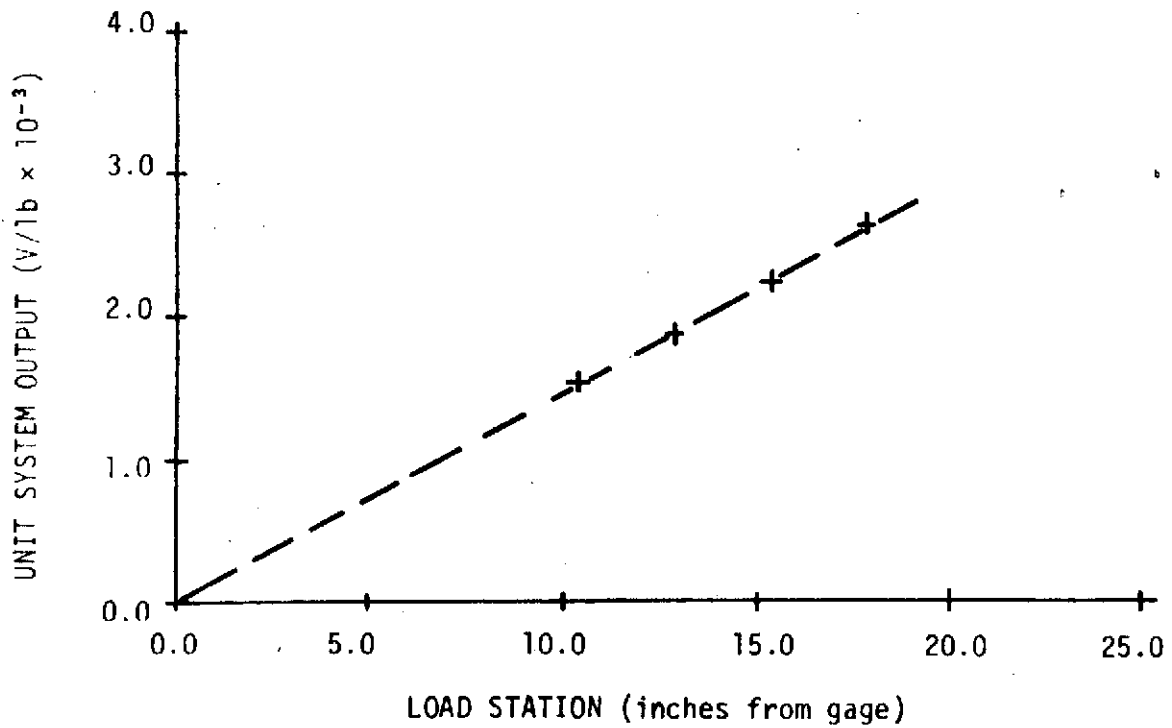
where i and j represent perpendicular planes at the same gage location, k . These nondimensional factors are similar to Poisson's ratio in that they relate transverse and longitudinal bending moments whereas Poisson's ratio relates transverse and longitudinal strains.

Figures C-4 through C-8 present the results of carrying out the above procedure for the designed force measuring system. The final numerical results are presented in Table C-1. These results were obtained using the complete data reduction system, including filtering, as explained in Chapter IV. Fifty readings were taken at each "dead weight" load value indicated in Figures C-6 through C-8. The average value of these fifty readings was then used in a "least-squares" curve fit digital computer program to obtain the slope values shown. First-, second- and third-order curves were obtained with the first-order curve showing the smallest standard deviation in all cases. The same curve-fit program was used to obtain the final slope values of the curves shown in Figures C-4 and C-5.

It should be noted that the conversion factors for the interactions are zero. Figure C-8 shows typical results obtained for all interaction effects in the first phase of the calibration. These results indicate the interaction effects are negligible when compared to the primary factors.

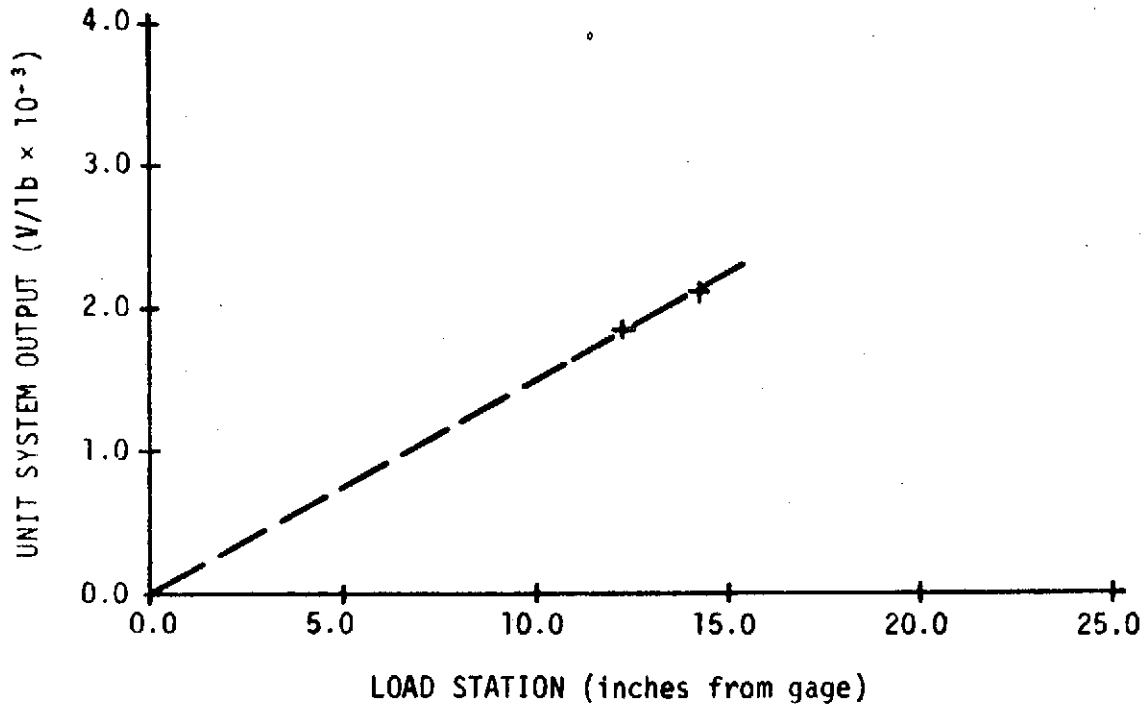


(a) AFT GAGE

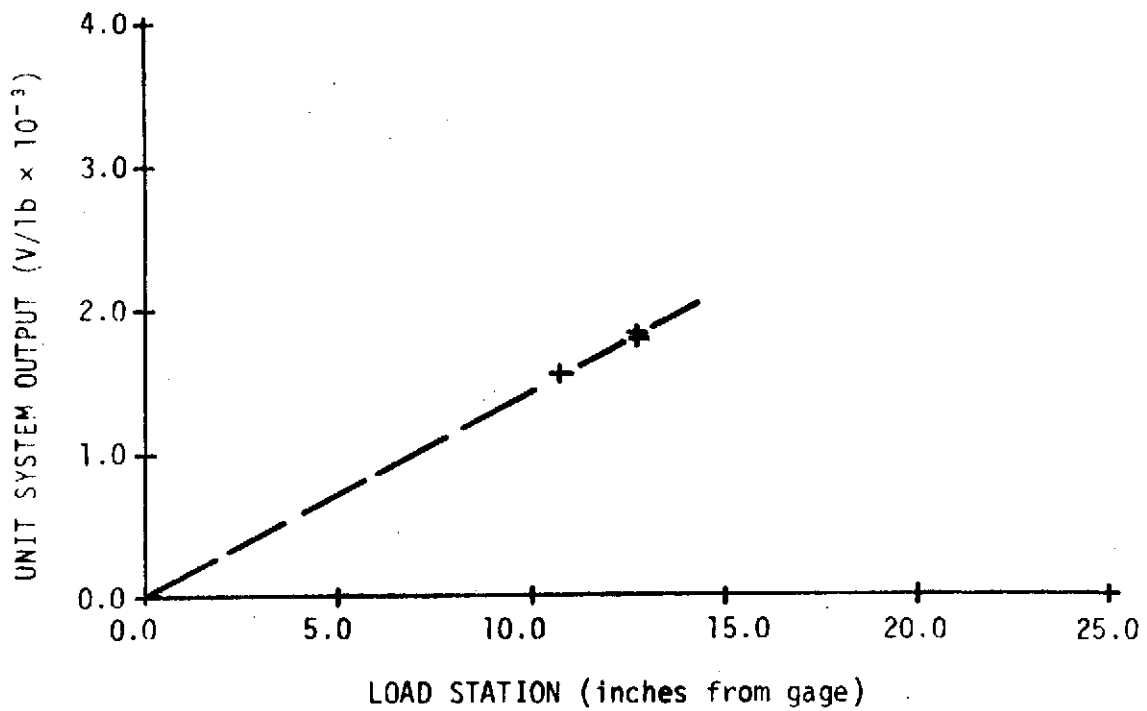


(b) FORWARD GAGE

FIGURE C-4. UNIT SYSTEM OUTPUT AS A FUNCTION OF LOAD STATION -- DRAG PLANE



(a) AFT GAGE



(b) FORWARD GAGE

FIGURE C-5. UNIT SYSTEM OUTPUT AS A FUNCTION OF LOAD STATION -- LIFT PLANE

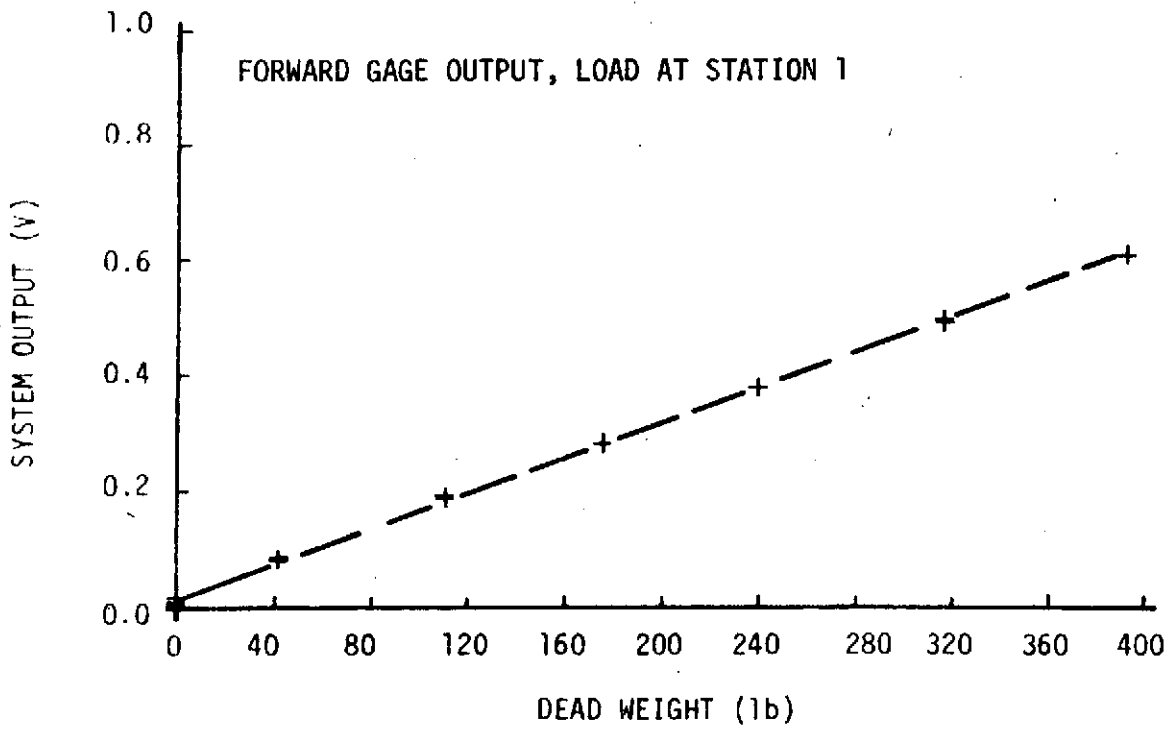
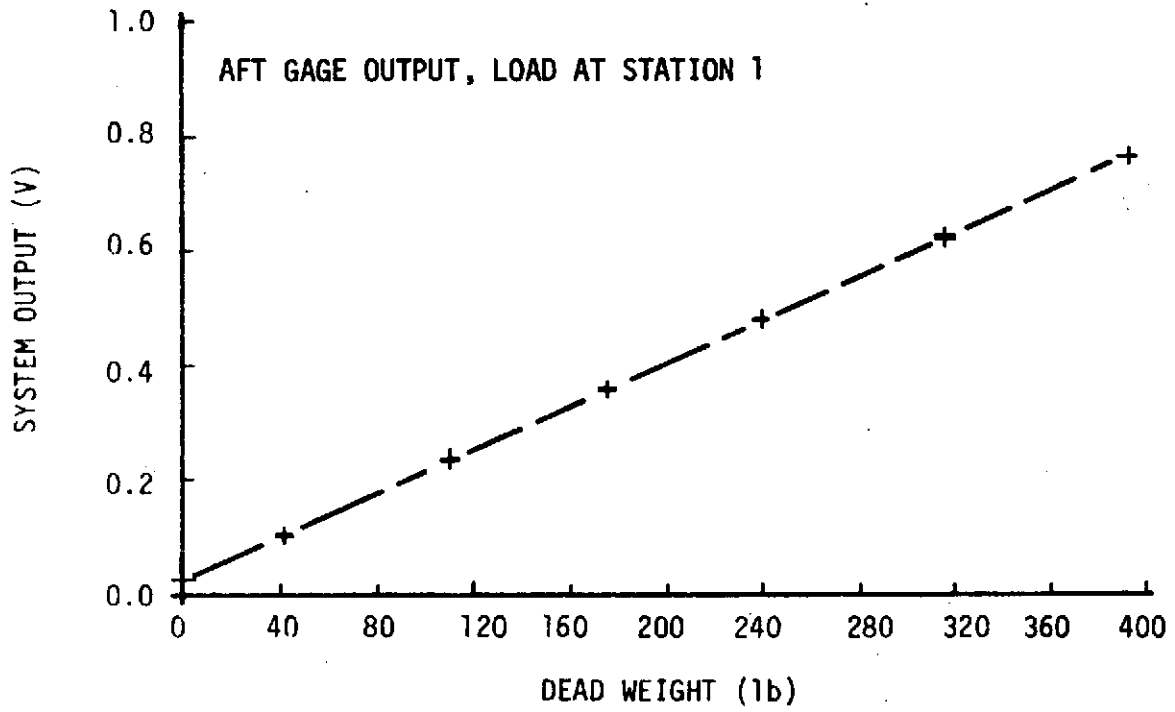


FIGURE C-6. DRAG PLANE STATIC CALIBRATION RESULTS

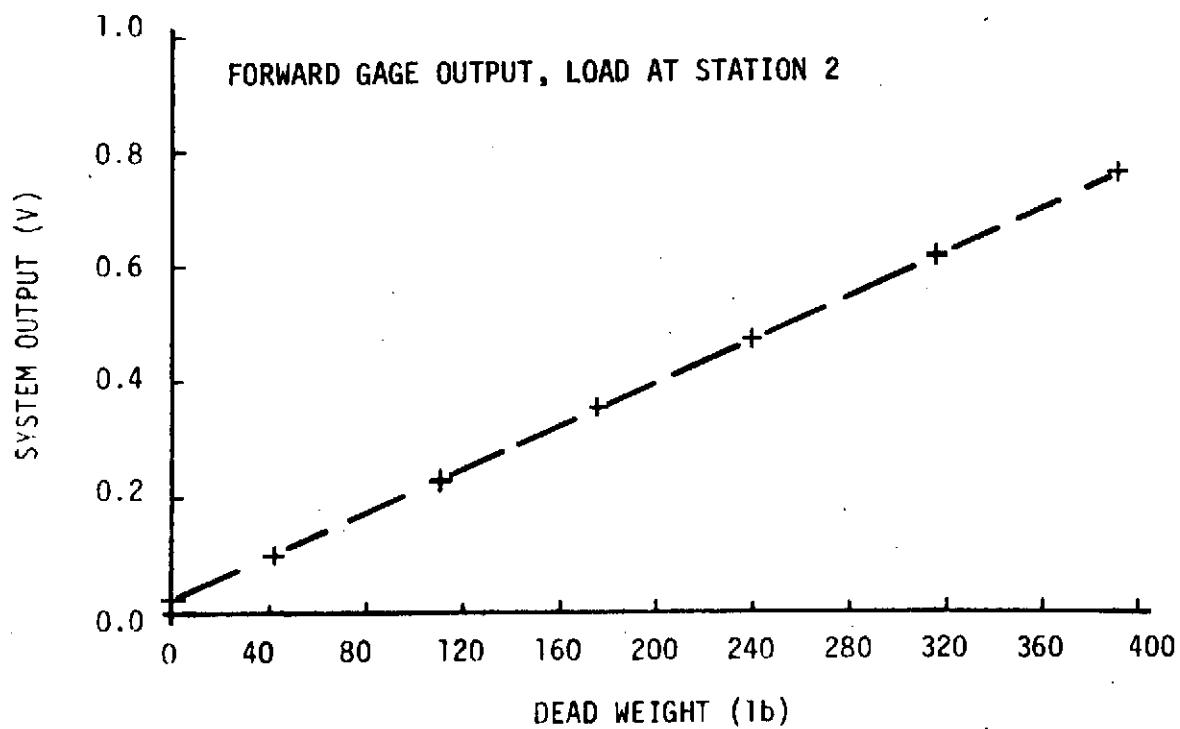
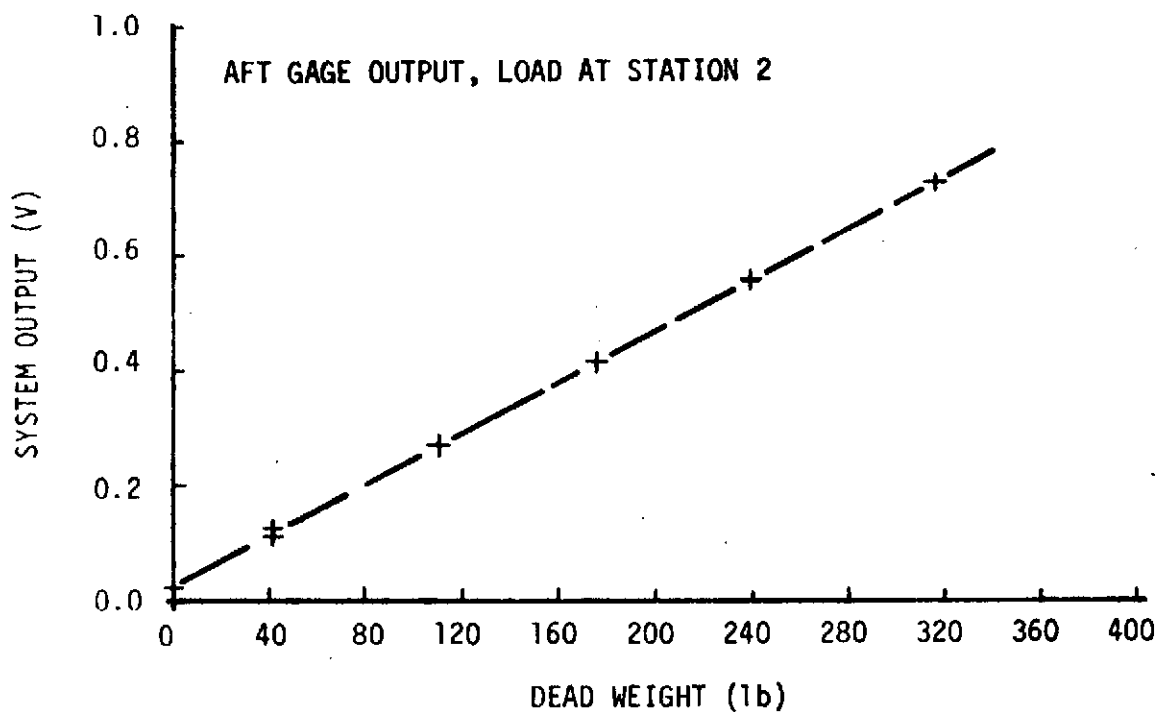


FIGURE C-6 - Continued

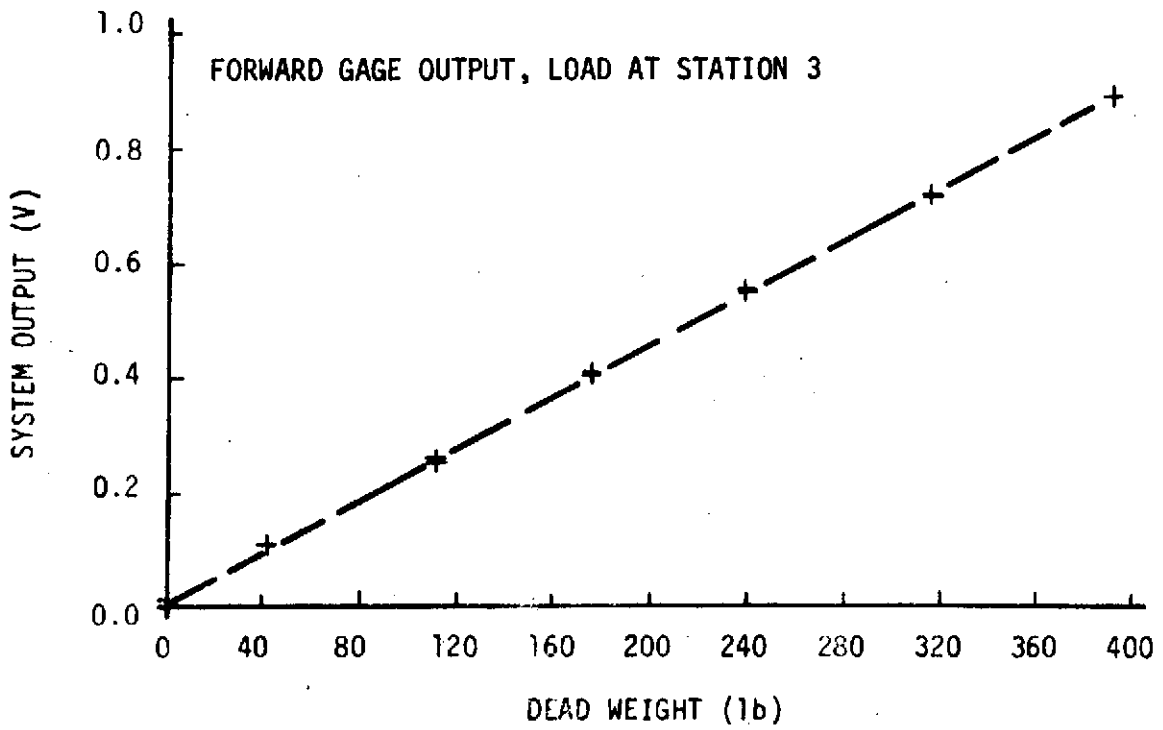
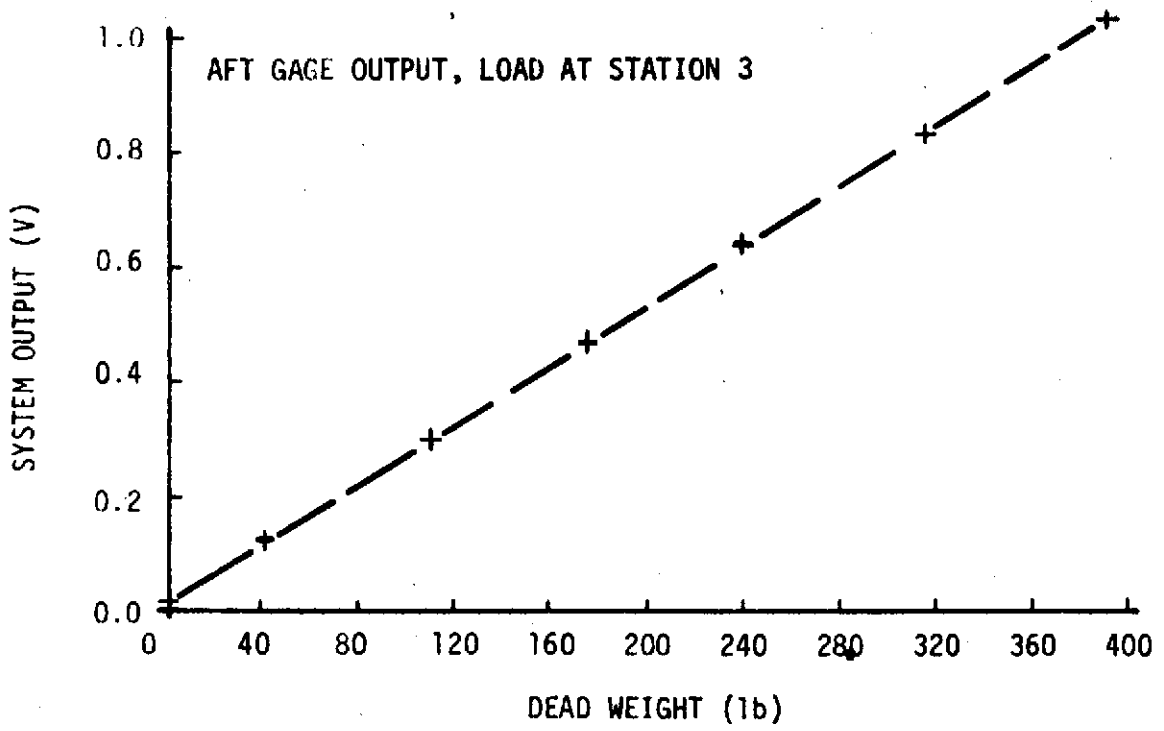


FIGURE C-6 - Continued

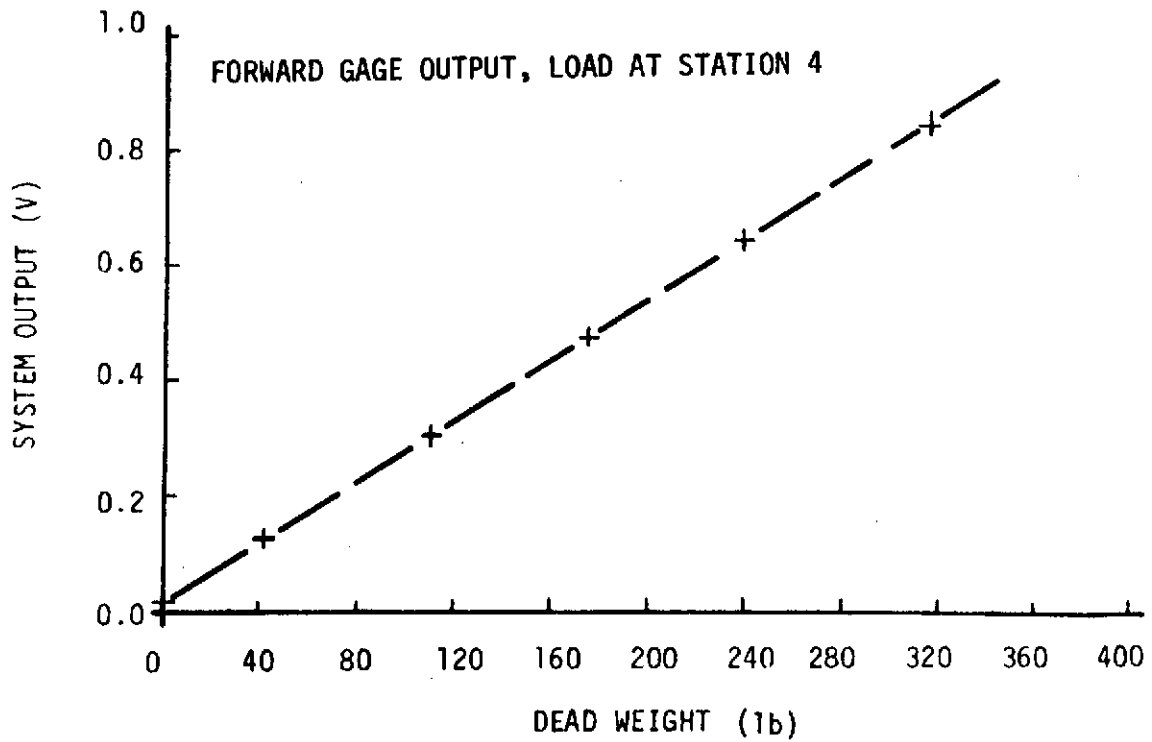
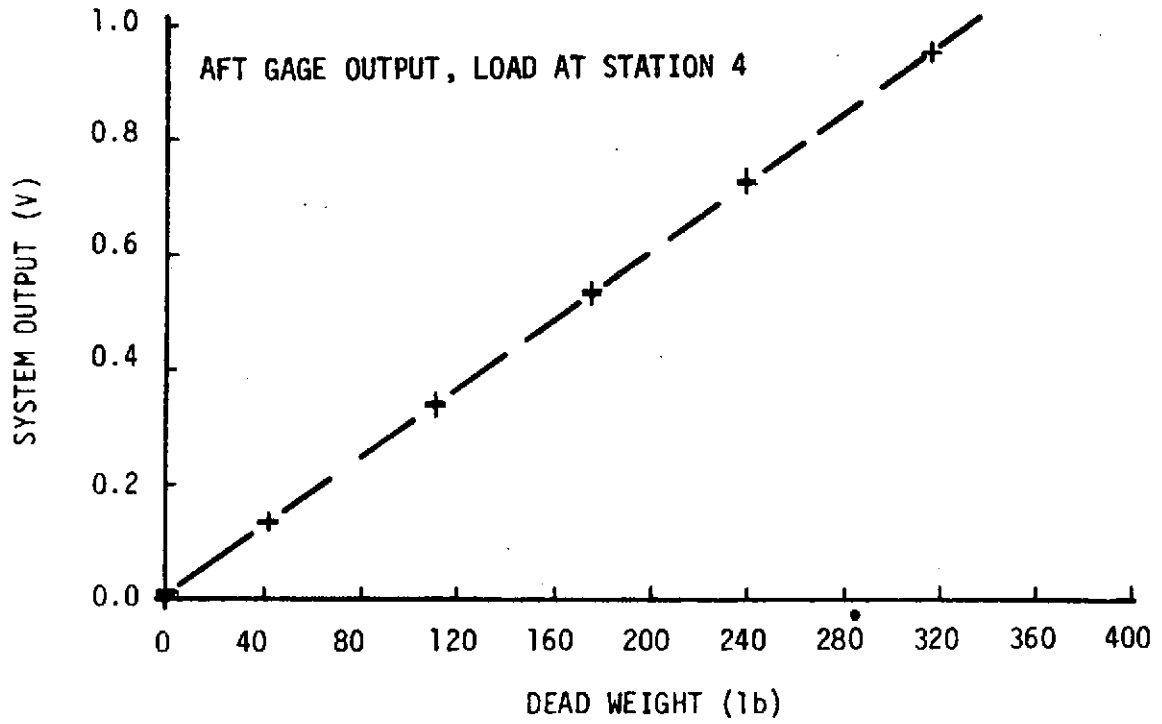


FIGURE C-6 - Concluded

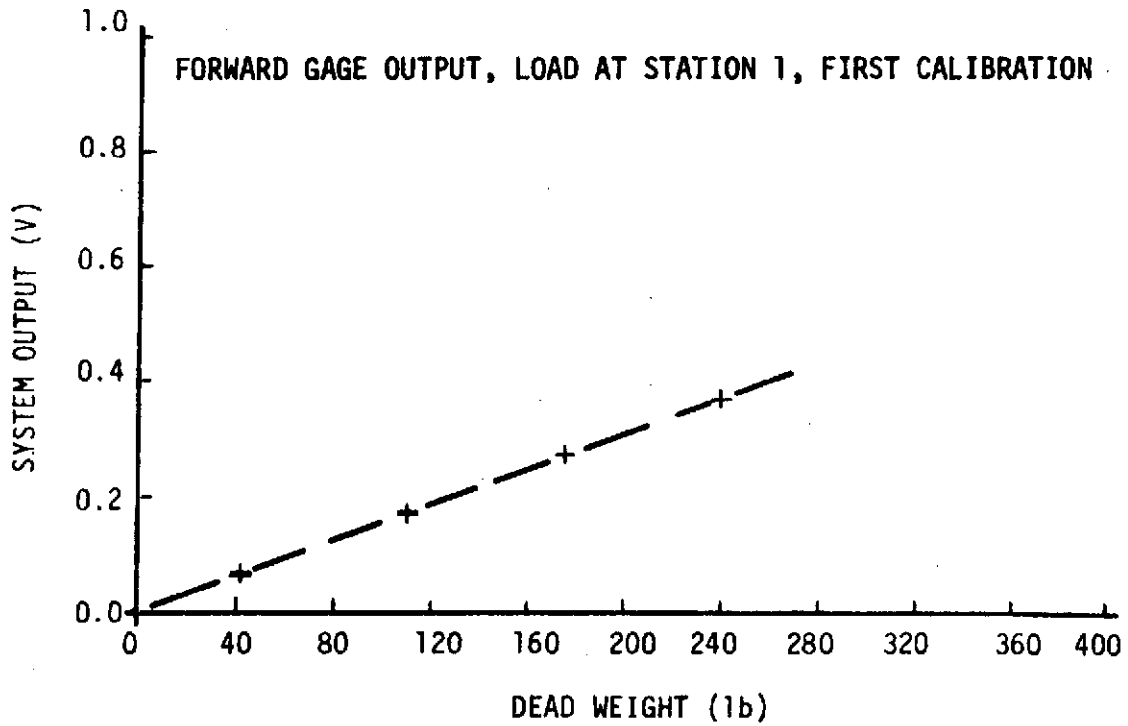
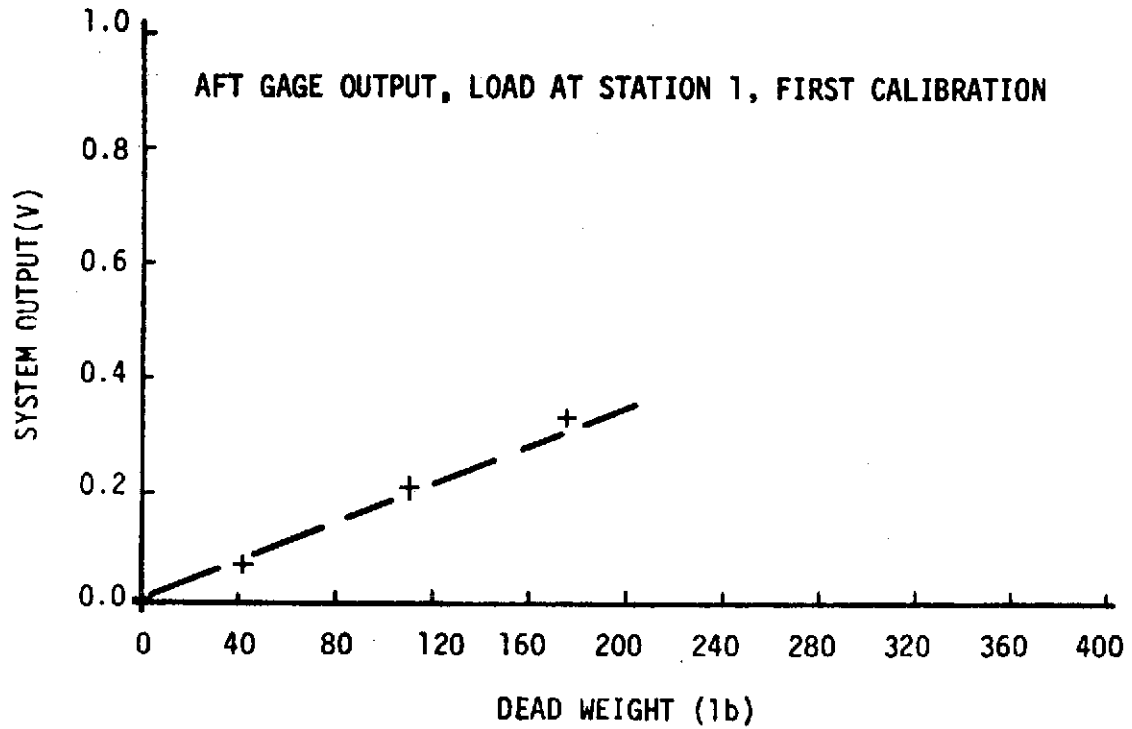


FIGURE C-7. LIFT PLANE STATIC CALIBRATION RESULTS

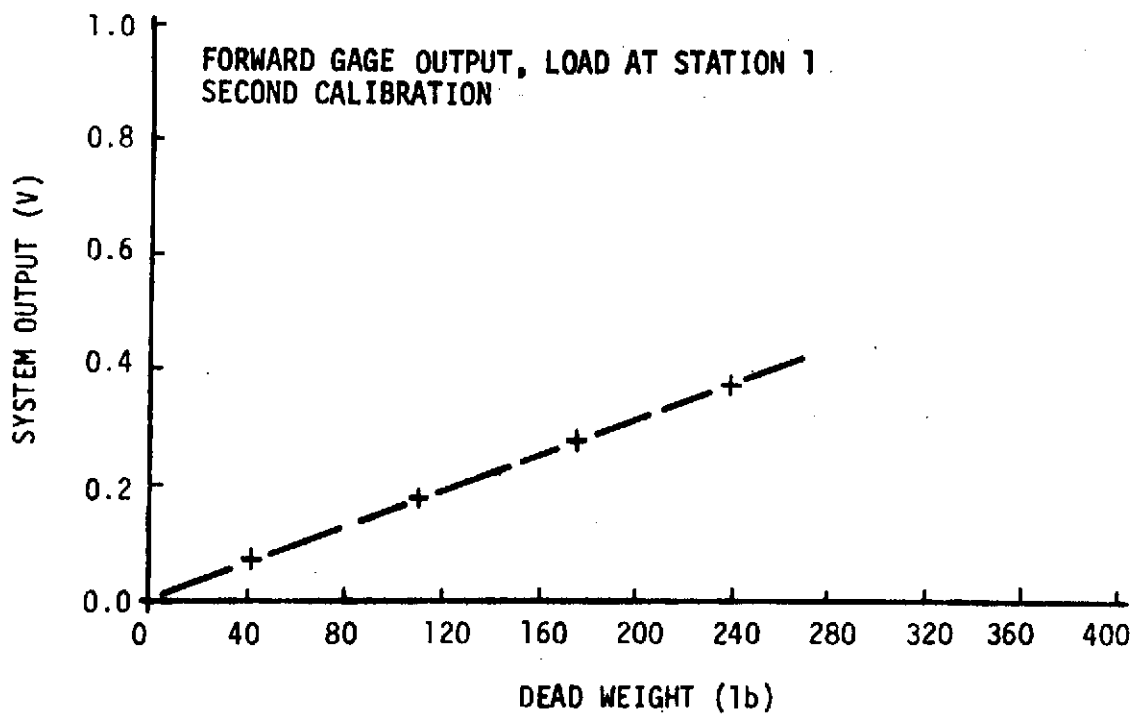
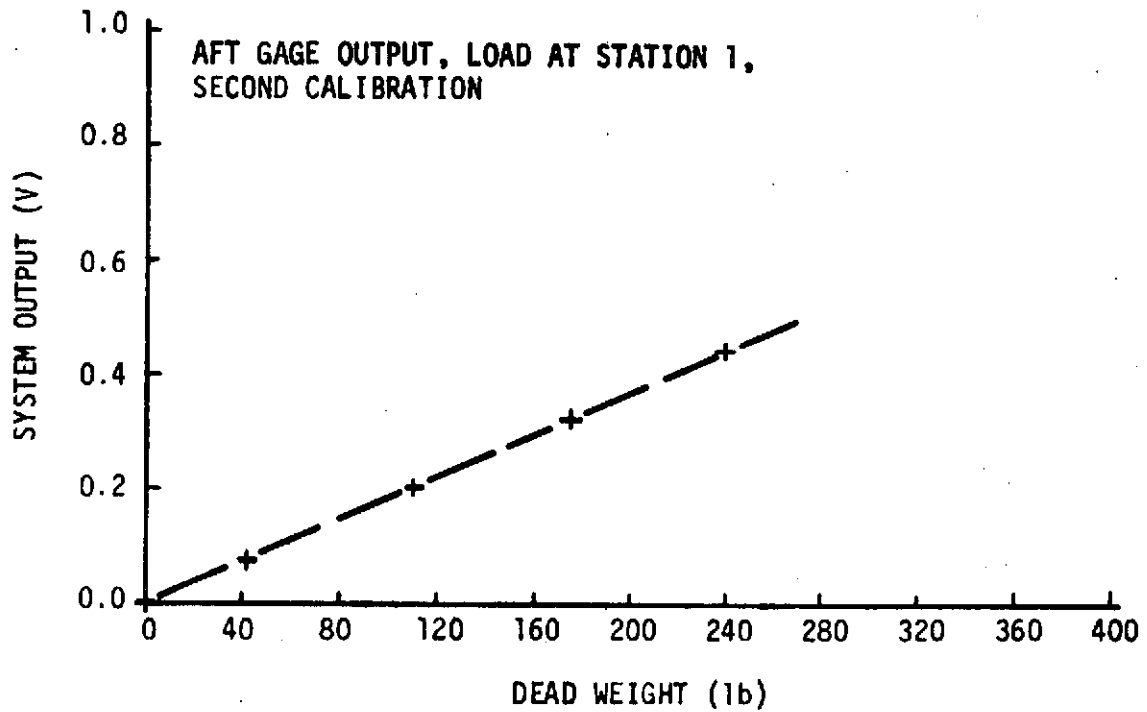


FIGURE C-7 - Continued

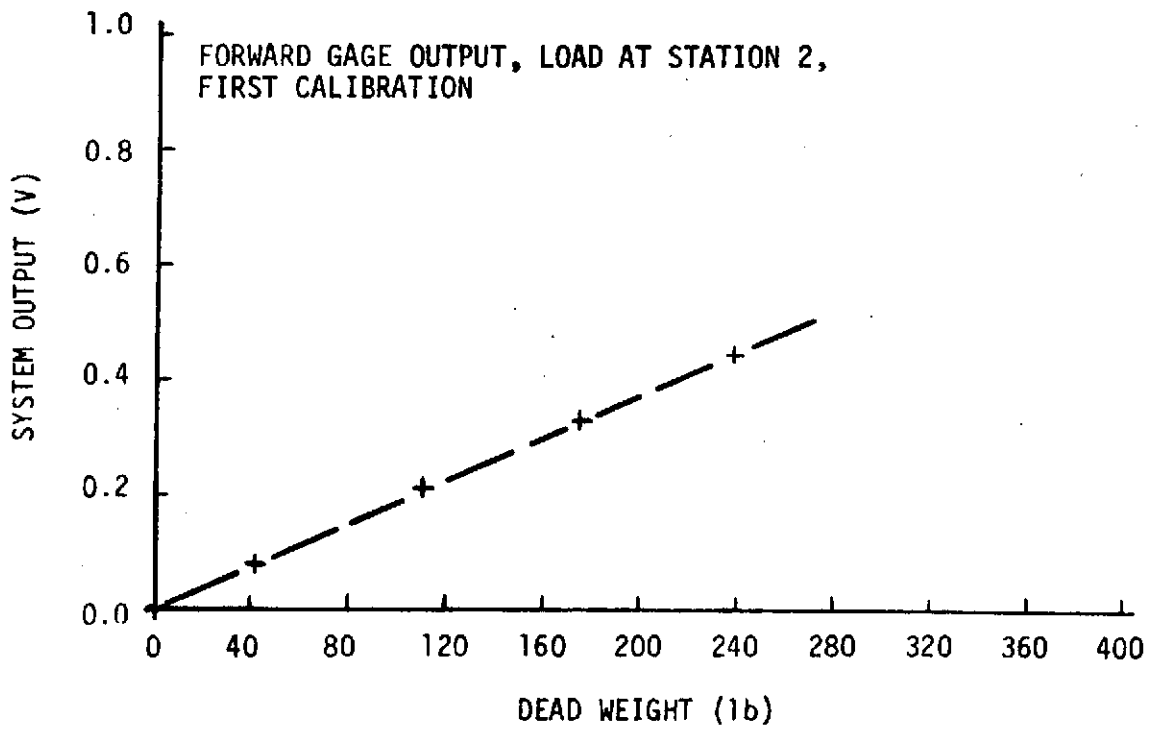
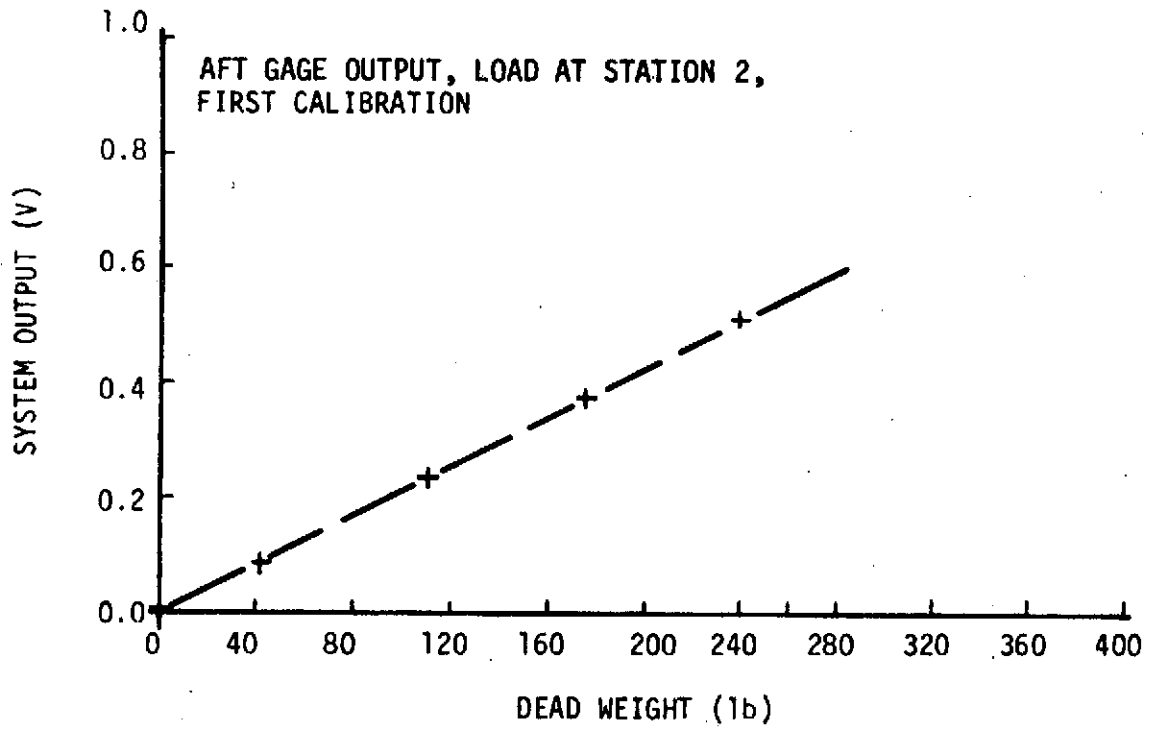


FIGURE C-7 - Continued

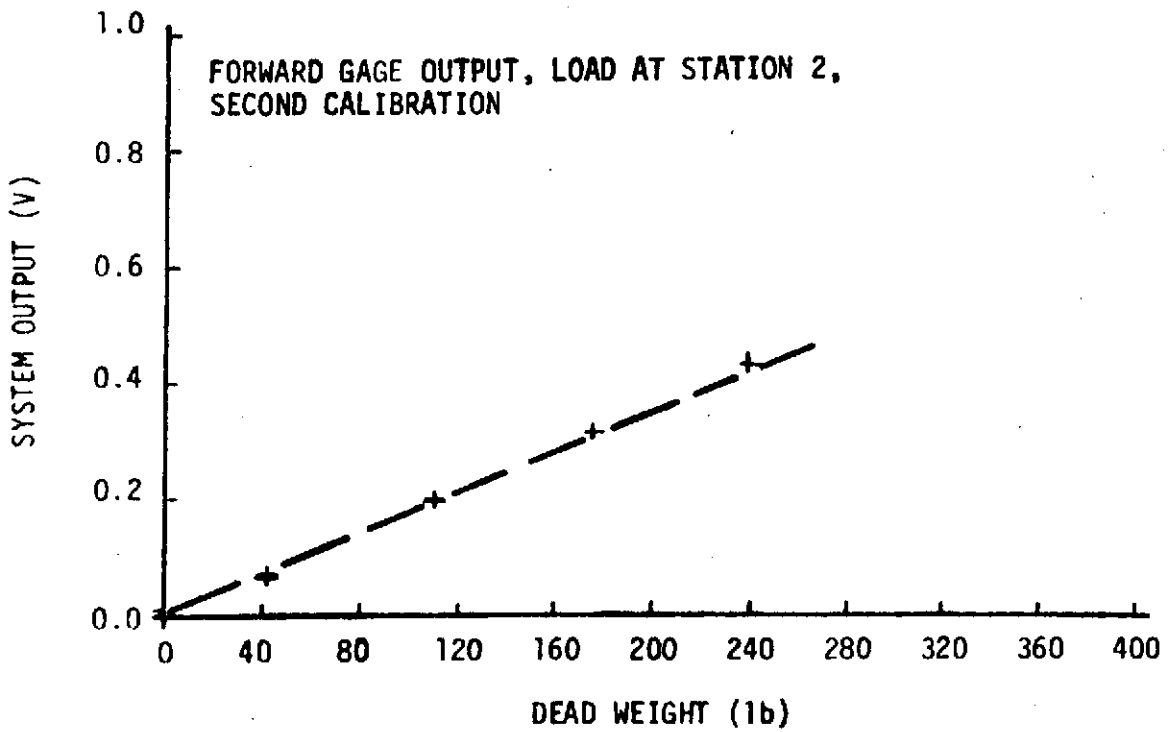
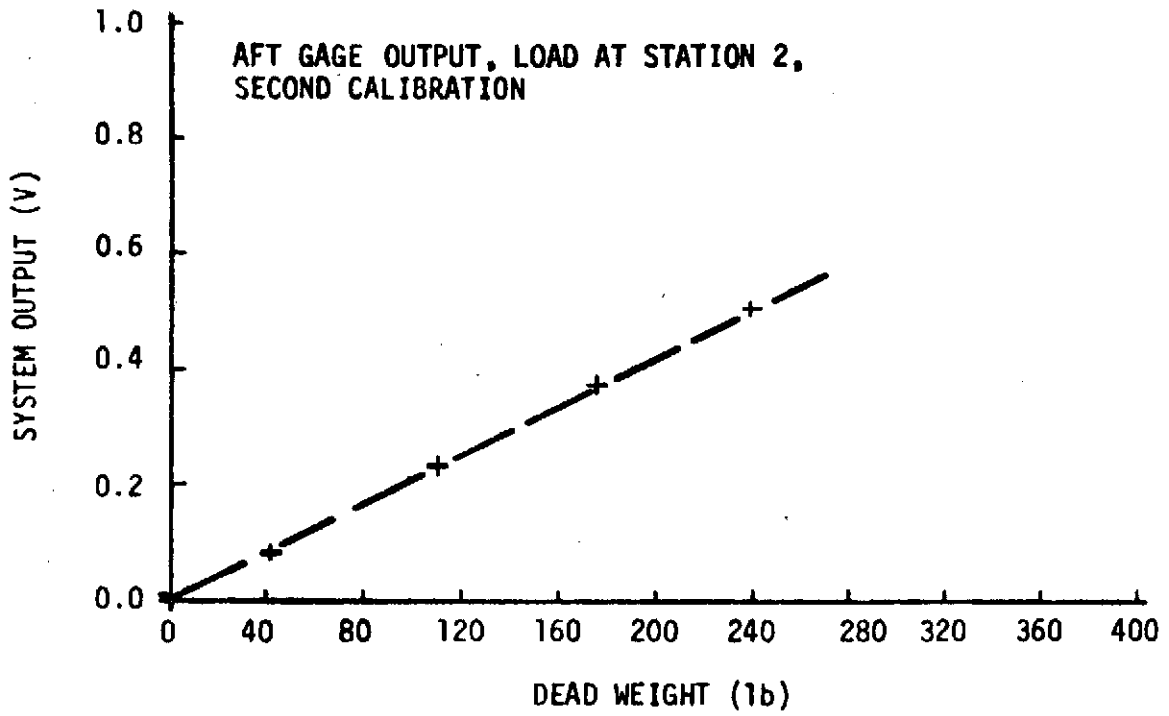


FIGURE C-7 - Continued

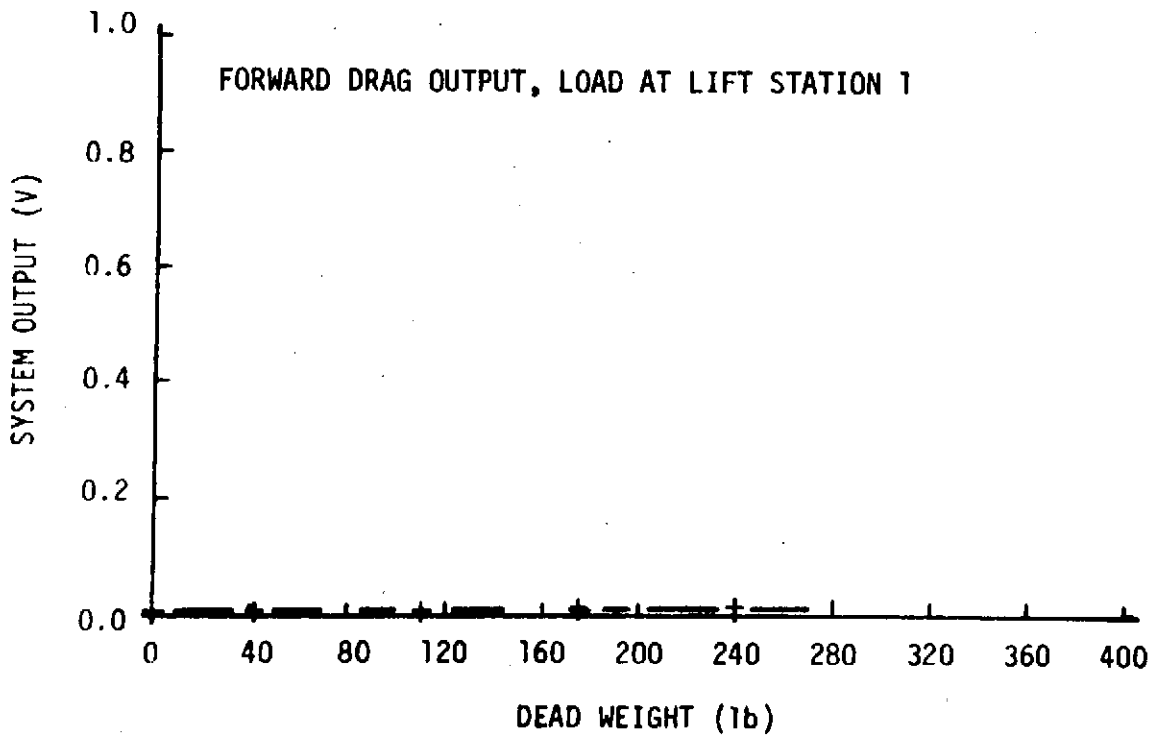
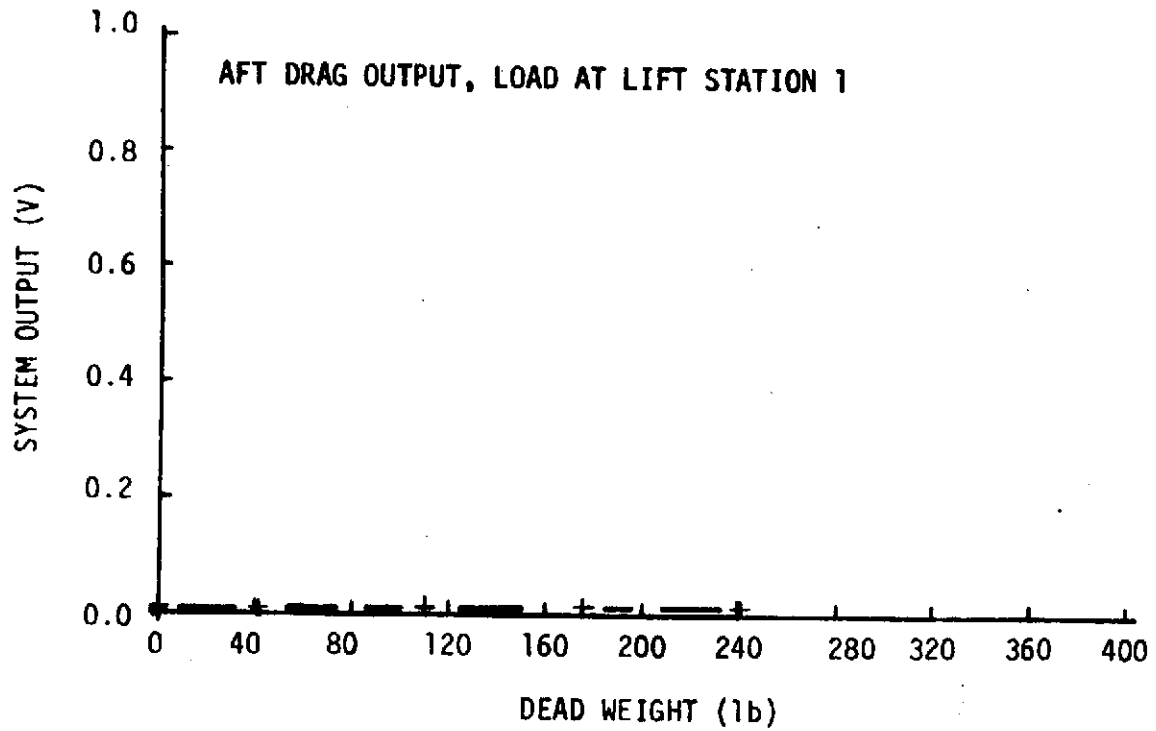


FIGURE C-8. DRAG PLANE OUTPUT FOR STATIC CALIBRATION LOADING IN THE LIFT PLANE

TABLE C-1. CONVERSION FACTORS USED IN CONVERTING SYSTEM
OUTPUT INTO BENDING MOMENTS

CHANNEL	PRIMARY CONVERSION FACTOR $\left(\frac{\text{in-lb}}{V}\right)$	INTERACTION CONVERSION FACTOR $\left(\frac{\text{in-lb}}{V}\right)$
Forward Drag	$K_1 = 6880.891$	$\frac{\partial M_1}{\partial M_3} = 0.0$
Aft Drag	$K_2 = 6800.685$	$\frac{\partial M_2}{\partial M_4} = 0.0$
Forward Lift	$K_3 = 7500.131$	$\frac{\partial M_3}{\partial M_1} = 0.0$
Aft Lift	$K_4 = 7226.530$	$\frac{\partial M_4}{\partial M_2} = 0.0$

APPENDIX D

DATA REDUCTION SYSTEM COMPONENT DESCRIPTION

The following paragraphs give a description of each of the components which make up the Data Reduction System. In addition, the methods used to obtain time-base expansion and data point time correlation are explained.

The Honeywell Medium Band Tape Recorder Model 7610 is a solid-state electronic recorder with fourteen wide band FM record/reproduce channels capable of recording at seven discrete tape speeds from 120 in/sec to 3.75 in/sec. The FM channels used in this analysis have a center frequency of 450 kilocycles (30-percent deviation) and a band width of 200 kilocycles. Tape flutter, skew, and time displacement error are maintained at low levels through the use of dual vacuum columns and independent servo control of each reel motor. Test data were recorded at a tape speed of 120 in/sec and reproduced at a tape speed of 3.76 in/sec. This provided a time-base expansion of 32. Therefore, a test run of 1 second was made to appear as being of 32-second duration.

The Hewlett-Packard Data Acquisition System Model 2012B is a modular, highly accurate system that accepts analog inputs, converts them to digital form, and provides a magnetic tape record

of the measurement results which can be input into the UNIVAC computer. The integrating digital voltmeter which is the heart of this system was used on the 1-volt scale with 1-microvolt resolution. The accuracy quoted for this voltage scale is 0.01 percent of the reading ± 30 microvolts (0.003 percent full scale). Maximum sampling rate for this system when used in the magnetic tape recording mode is given as 15 samples per second.

Modification to the data acquisition system was necessary to provide accurate means of obtaining time correlation of the test data. Since the data acquisition system could digitize only one channel at a time, several passes (eight, in most cases) through the system were necessary for each test run. Time base correlation was achieved by recording a steady-state dc voltage level (5.0 volts) during each test run. This voltage level, recorded along with the test data, was introduced just before test initiation and removed immediately after the test completion. This voltage level was fed to the data acquisition system together with each data record and was used to start and stop the digitizing/recording modules of the system. Since each channel was thus digitized and recorded from the same starting signal, data points from all channels could be referred to a single time base by use of the digital computer.

To maintain a check of this method, the triggering dc voltage also was supplied to a Beckman timer and the time interval used for

each data channel recorded. Results indicated that less than 0.001 second differential existed between the extremes of the data channel time bases. This is less than one-half the time between data points. It also was determined that the sampling rate for the modified data acquisition system was 14.25 samples per second. The sampling rate was investigated over several ranges of data field lengths and no measurable variation was determined.

The combination of the time base expansion and the indicated sampling rate produced a maximum sampling rate of 456 samples per second ($\Delta t = 0.00219$ second). The requirement initially established by the author for a digitizing system was 10 samples per cycle of dynamic data. This exceeds the criterion generally associated with digitizing dynamic data, but should not produce any questions about this aspect of the digital data reduction system. Following this criterion, the maximum frequency which could be analyzed in this test data is 45.6 hertz with all higher frequencies to be removed, either by electronic or digital filtering.

The amplifiers used in this analysis were the Honeywell Accudata III D-C Wide Band Differential Amplifier. This is a chopper-stabilized, all-transistor amplifier designed for use with strain gages and thermocouples. It has a frequency response from dc to 20 kilocycles, noise and drift less than 0.007 percent on typical

gains, a complete variable gain adjustment with gain stability, and linearity better than 99.99 percent. Because of its stable linear, low-noise output, it is suitable for driving a visicorder, multiplexer, analog-to-digital converter, or tape recorder.

The Signal Research Corporation's dc power supplies and signal conditioning system also were used. Figure D-1 shows the four-wire, calibrate both sides, circuit used to power, calibrate, monitor, and balance the strain gage bridges. After static calibration, this circuit was used to verify the power settings and balance condition before each test run. A similar circuit was also used for the three-wall mounted pressure transducers.

The UNIVAC digital computer and the Stromberg-Carlson plotter are not considered basic to the data reduction system since the software used in this analysis is applicable to numerous other computing and plotting systems.

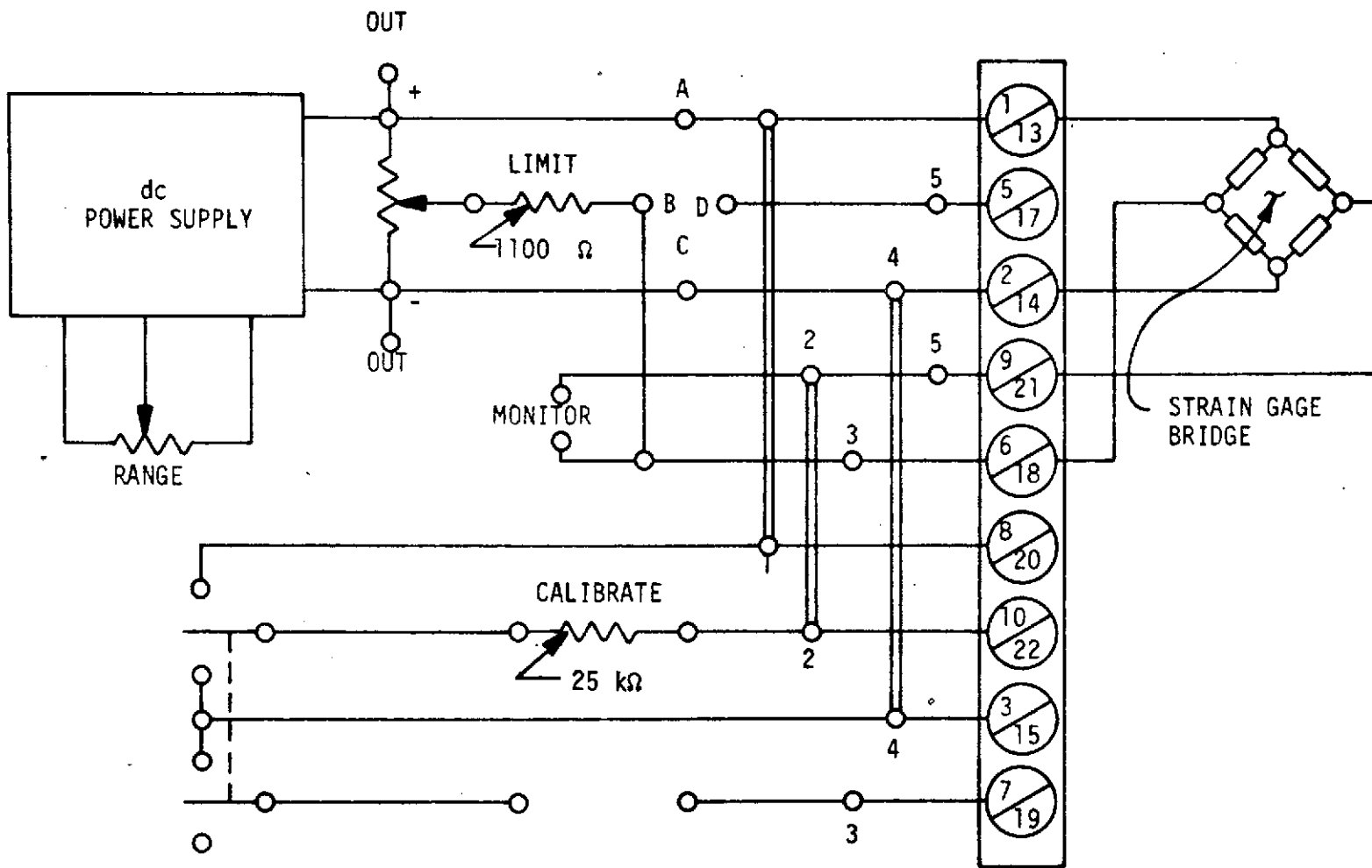


FIGURE D-1. SCHEMATIC DIAGRAM OF STRAIN GAGE BRIDGE CIRCUIT

BIBLIOGRAPHY

- Abernathy, F. H. and R. E. Kronauer, "The Formation of Vortex Streets," J. Fluid Mechanics, Vol. 13, p. 1, 1962
- Achenback, E., "Distribution of Local Pressure and Skin Friction Around a Circular Cylinder in Cross-Flow Up to $Re = 5 \times 10^6$," J. Fluid Mechanics, Vol. 34, Part 4, p. 625, 1968
- Achenback, E., "Influence of Surface Roughness on the Cross-Flow Around a Circular Cylinder," J. Fluid Mechanics, Vol. 46, p. 321, 1971
- Acrivas, A., D. D. Snowden, A. S. Grove, and E. E. Peterson, "The Steady Separated Flow Past a Circular Cylinder at Large Reynolds Numbers," J. Fluid Mechanics, Vol. 21, p. 737, 1965
- Acrouos, A., "Further Experiments on Steady Separated Flows Past Bluff Objects," J. Fluid Mechanics, Vol. 34, p. 25, 1968
- Asher, J. A. and Dosanjh, "An Experimental Investigation of the Formation and Flow Characteristics of an Impulsively Generated Vortex Street," Proc. ASME Symposium on Unsteady Flow, Paper No. 68-FE-32, 1968
- Batchelor, G. K., An Introduction to Fluid Dynamics, Cambridge University Press, London, England, 1966
- Batchelor, G. K., "Axial Flow in a Trailing Line Vortices," J. Fluid Mechanics, Vol. 20, p. 645, 1964
- Bearman, P. W., "On Vortex Shedding from a Circular Cylinder in the Critical Reynolds Number Regime," J. Fluid Mechanics, Vol. 37, p. 577, 1969

- Bearman, P. W., "Investigation of the Flow Behind a Two-Dimensional Model with a Blunt Trailing Edge and Fitted with Splitter Plates," J. Fluid Mechanics, Vol. 21, p. 241, 1965
- Bearman, P. W., "On Vortex Street Wakes," J. Fluid Mechanics, Vol. 28, p. 625, 1967
- Benjamin, T. B., "Theory of the Vortex Breakdown Phenomenon", J. Fluid Mechanics, Vol. 14, p. 593, 1963
- Berger, S. A., Y, K, Cheung, and P. Raghuranan, "The Flow About a Circular Cylinder at Low Reynolds Numbers Using the Method of Series Truncation With a Novel Coordinate System," University of California, Berkeley, Aeronautical Sciences Division Report No. AS-71-1, 1971
- Bickley, W. G., "The Influence of Vortices Upon the Resistance Experienced by Solids Moving Through a Liquid," Proc. Roy. Soc., A119, p. 146, 1928
- Birkhoff, G., "Formation of Vortex Streets," J. Applied Phy., Vol. 24, p. 98, 1953
- Bishop, R. E. D. and A. Y. Hassen, "The Lift and Drag Forces on a Circular Cylinder," Proc. Roy. Soc., A277, p. 32, 1964
- Bishop, R. E. D. and A. Y. Hassen, "The Lift and Drag Forces on a Circular Cylinder in a Flowing Fluid," Proc. Roy. Soc., A277, p. 51, 1964
- Bloor, M. S., "The Transition to Turbulence in the Wake of a Circular Cylinder," J. Fluid Mechanics, Vol. 19, p. 290, 1964
- Bloor, M. S., "The Transition to Turbulence in the Wake of a Circular Cylinder," J. Fluid Mechanics, Vol. 19, p. 290, 1964
- Bloor, M. S. and J. H. Gerrard, "Measurements on Turbulent Vortices in a Cylinder Wake," Proc. Roy. Soc., A294, p. 319, 1966
- Borges, A. R. J., "Vortex Shedding Frequencies on the Flow Through Two-Row Banks of Tubes," J. Mech. Eng. Science, Vol. 11, No. 5, p. 498, 1969

- Bryson, A. E., "Symmetric Vortex Separation on Circular Cylinders and Cones," J. Applied Mechanics, p. 643, 1959
- Buell, D. A. and G. C. Kenyson, "The Wind-Induced Loads on a Dynamically Scaled Model of a Large Missile in Launching Position," NASA TM X-109, 1959
- Buell, D. A., G. B. McCullough, and W. T. Steimetz, "A Wind Tunnel Investigation of Ground-Wind Loads on Axisymmetric Launch Vehicles," NASA TN D-1893, 1963
- Chang, P. K., Separation of Flow, Pergamon Press, Oxford, England, 1966
- Chen, C. F. and B. J. Mangione, "Vortex Shedding from Circular Cylinders in Sheared Flow," AIAA Journal, Vol. 7, No. 6, p. 1211, 1969
- Chen, C. F. and D. B. Ballengee, "Vortex Shedding from Circular Cylinders in an Oscillating Freestream," AIAA Journal, Vol. 9, No. 2, p. 340, 1971
- Coder, D. W., "Location of Separation on a Circular Cylinder in Crossflow as a Function of Reynolds Number," Naval Ship Research and Development Center, Report 3647, 1971
- Dalton, C. and F. D. Masch, "Influence of Secondary Flow on Drag Force," Proc. ASCE, Vol. 94, p. 1249, 1968
- Dennis, S. C. R. and G. Z. Chang, "Numerical Solution for Steady Flow Past a Circular Cylinder at Reynolds Numbers up to 100," J. Fluid Mechanics, Vol. 42, No. 3, p. 471, 1970
- Dolapchiev, B. and B. Sendov, "Symmetrical Flow Around a Circular Cylinder with Two Vortices Behind It. Trajectories of the Vortices and Drag of the Cylinder," Dokladi Akademia Nauk, Vol. 1928, p. 53, 1959
- el Baroudi, M. Y., "Measurement of Two-Point Correlations of Velocity Near a Circular Cylinder Shedding a Karman Vortex Sheet," UTIA, Technical Note No. 31, 1960
- Etkin, B., G. K. Korbacher, and R. T. Keefe, "Acoustic Radiation from a Stationary Cylinder in a Fluid Stream (Aeolian Tones)," Inst. of Aero-Physics, University of Toronto, Report No. 39, 1956

- Fage, A. and F. C. Johansen, "The Structure of Vortex Sheets," Phil. Mag., Vol. 5, p. 417, 1928
- Fage, A. and F. C. Johansen, "On the Flow of Air Behind an Inclined Flat Plate of Infinite Span," Proc. Roy. Soc., A1116, p. 170, 1927
- Ferguson, N. and G. V. Parkinson, "Surface and Wake Flow Phenomena of the Vortex-Excited Oscillation of a Circular Cylinder," J. of Engr. for Industry, p. 831, 1967
- Fromm, J. E. and F. H. Harlow, "Numerical Solution of the Problem of Vortex Street Development," Phys. of Flds., Vol. 6, p. 975, 1963
- Fung, Y. C., "Fluctuating Lift and Drag Acting on a Cylinder at Supercritical Reynolds Numbers," J. Aero-Space, Sciences, Vol. 27, No. 11, p. 801, 1960
- Gaster, M., "Vortex Shedding from Circular Cylinders at Low Reynolds Numbers," J. Fluid Mechanics, Vol. 46, p. 749, 1971
- Gerrard, J. H., "Measurements of Sound from Circular Cylinders in an Air Stream," Proc. Phys. Soc., B, 68, p. 453, 1955
- Gerrard, J. H., "An Experimental Investigation of the Oscillating Lift and Drag of a Circular Cylinder Shedding Turbulent Vortices," J. Fluid Mechanics, Vol. 11, p. 244, 1961
- Gerrard, J. H., "A Disturbance-Sensitive Reynolds Number Range of the Flow Past a Circular Cylinder," J. Fluid Mech., Vol. 22, p. 187, 1965
- Gerrard, J. H., "The Three Dimensional Structure of the Wake of a Circular Cylinder," J. Fluid Mech., Vol. 25, p. 143, 1966
- Gerrard, J. H., "The Mechanics of the Formation Region of Vortices Behind Bluff Bodies," J. Fluid Mech., Vol. 25, p. 401, 1966
- Gerrard, J. H., "Numerical Computation of the Magnitude and Frequency of the Lift on a Circular Cylinder," Phil. Trans. Roy. Soc., London, Series A, Vol. 261, No. 1118, p. 137, 1967

- Goldman, R., "Generation and Suppression of von Karman Vortex Forces," Martin Co. Eng. Report No. 8984, July 1957
- Görtler, H., "Verdrängungswirkung der Laminaren Grenzschicht und Druckwiderstrand," Ingenieur Archiv., Vol. 14, p. 286, 1944
- Graham, J. M. R., "The Effect of End-Plates on the Two Dimensionality of a Vortex Wake," Aeronautical Quarterly, Vol. 20, p. 237, 1969
- Griffin, O. M. and C. W. Votaw, "The Vortex Street in the Wake of a Vibrating Cylinder," J. Fluid Mechanics, Vol. 51, p. 31, 1972
- Hall, M. G., "A Theory for the Core of a Leading-Edge Vortex," J. Fluid Mech., Vol. 11, p. 209, 1961
- Hamielc, A. E. and Raal, J. D., "Numerical Studies of Viscous Flow Around Circular Cylinders," Phys. of Flds., Vol. 12, p. 11, 1969
- Hanson, F. B. and P. D. Richardson, "The Near-Wake of a Circular Cylinder in Crossflow," Proc. ASME Symposium on Unsteady Flow, Paper No. 68-FE-5, 1968
- Harlow, F. H. and J. E. Fromm, "Dynamics and Heat Transfer in the von Karman Wake of a Rectangular Cylinder," Phys. of Flds., Vol. 7, p. 1147, 1964
- Hartog, J. P. D., "Recent Technical Manifestations of von Karman's Vortex Wake," Proc. Nat. Acad. Sci., Washington, 40, p. 155, 1954
- Harvey, J. K., "Some Observations of the Vortex Breakdown Phenomenon," J. Fluid Mech., Vol. 14, p. 585, 1963
- Heinzer, A. and C. Dalton, "Wake Observations for Oscillating Cylinders," J. Basic Engr., Trans. ASME Series D, Vol. 91, p. 850, 1969
- Honji, H. and S. Taneda, "Unsteady Flow Past a Circular Cylinder," J. Phys. Soc. of Jap., Vol. 27, p. 1668
- Honji, H. and S. Taneda, "Vortex Wakes of Oscillating Circular Cylinders," Rep. Rev. for Inst. Appl. Mech., Vol. 16, p. 211, 1968

- Hooker, S. G., "On the Action of Viscosity in Increasing the Spacing Ratio of a Vortex Street," Proc. Roy. Soc., Series A, 154, p. 67, 1936
- Horlock, J. H., "Fluctuating Lift Forces on Aerofoils Moving Through Transverse and Chordwise Gusts," Proc. ASME Symposium on Unsteady Flow, Paper No. 68-FE-28, 1968
- Humphreys, J. S., "On a Circular Cylinder in a Steady Wind at Transition Reynolds Number," J. Fluid Mech., Vol. 9, p. 603, 1960
- Ingham, D. B., "Note on the Numerical Solution for Unsteady Viscous Flow Past a Circular Cylinder," J. Fluid Mech., Vol. 31, p. 815, 1968
- Inversen, H. W. and R. Balent, "A Correlating Modulus for Fluid Resistance in Accelerated Motion," J. of Appl. Phy., Vol. 22, p. 324, 1951
- Jones, G. W., J. J. Cincotta, and R. W. Walker, "Aerodynamic Forces on a Stationary and Oscillating Circular Cylinder at High Reynolds Number," NASA TR R-300, February 1969
- Jones, G. W., "Unsteady Lift Forces Generated by Vortex Shedding about a Large, Stationary, and Oscillating Cylinder at High Reynolds Numbers," Proc. ASME Symposium on Unsteady Flow, Paper No. 68-FE-36, 1968
- Kawaguti, M., "Discontinuous Flow Past a Circular Cylinder," J. of Phys. of Jap., Vol. 8, p. 403, 1953
- Kawaguti, M., "Numerical Solution of the Navier-Stokes Equations for Flow Around a Circular Cylinder at a Reynolds Number 40," J. of Phys. Soc., of Jap., Vol. 8, p. 747, 1953
- Keefe, R. T., "An Investigation of the Fluctuating Forces Acting on a Stationary Circular Cylinder in a Subsonic Stream and of the Associated Sound Field," University of Toronto Inst. Aero-Physics Department, No. 75, 1961

- Keim, S. R., Fluid Resistance to Cylinder in Accelerated Motion, "Proc. ASCE, Vol. 82, HY 6, p. 113-1, 1956
- Koopmann, G. H., "The Vortex Wakes of Vibrating Cylinders at Low Reynolds Numbers," J. Fluid Mech., Vol. 28, p. 501, 1967
- Kovasnay, L. S. G., "Hot-Wire Investigation of the Wake Behind Cylinders at Low Reynolds Numbers," Proc. Roy. Soc., A, 198, p. 174, 1949
- Krzywoblocki, M. Z., "Vortex Streets in Incompressible Media," Applied Mech. Review, Vol. 6, No. 9, p. 393, 1953
- Kuchemann, D. and J. Weber, "Vortex Motions," ZAMM, 45, p. 31, 1965
- Kuchemann, D., "Report on the I. U. T. A. M. Symposium on Concentrated Vortex Motions in Fluids," J. Fluid Mech., Vol. 21, p. 1, 1965
- Laird, A. D. K. and C. A. Johnson, "Drag Forces on an Accelerated Cylinder," J. of Petroleum Tech., Vol. 8, p. 65, 1956
- Laird, D. K., C. A. Johnson, and R. W. Walker, "Water Forces on Accelerated Cylinders," Proc. ASCE, Vol. 85, No. WW1, p. 99, 1959
- Laird, A. D. K., "Eddy Formation Behind Circular Cylinders," Proc. ASCE, Vol. 97, HY 6, p. 763, 1971
- McGregor, D. M., "An Experimental Investigation of the Oscillating Pressures on a Cylinder in a Fluid Stream," University of Toronto, Institute of Aero-Physics, Technical Note No. 14, 1957
- McNown, J., "Drag in Unsteady Flows," Proc. IX Int. Cong. Appl. Mech., Brussels, p. 124, 1957
- McNown, M. and G. H. Keulegan, "Vortex Formation and Resistance in Periodic Motion," Proc. ASCE, Vol. 85, EMI, p. 1, 1959
- Michalke, A., "Vortex Formation in a Free Boundary Layer According to Stability Theory," J. Fluid Mech., Vol. 22, p. 371, 1965

- Morkovin, M. V., "Flow Around Circular Cylinder - A Kaleidoscope of Challenging Fluid Phenomena," Proc. ASME Symposium on Fully Separated Flows, p. 102, 1964
- Pagon, W. W., "Vibration Problem in Tall Stacks Solved By Aerodynamics," Engr. News Record, July 12, 1934
- Parkinson, G. V. and T. Jandali, "A Wake Source Model for Bluff Body Potential Flow," J. Fluid Mechanics, Vol. 40, No. 3, p. 577, 1970
- Payne, R. B., "Calculations of Unsteady Viscous Flow Past a Circular Cylinder," J. Fluid Mech., Vol. 4, p. 81, 1958
- Penzien, J., "Wind Induced Vibrations of Cylindrical Structures," Proc. ASCE, Vol. 83, No. EMI, p. 1141-1, 1957
- Phillips, O. M., "The Intensity of Aeolian Tones," J. Fluid Mech., Vol. 1, p. 607, 1956
- Pierce, D., "Photographic Evidence of the Formation and Growth of Vorticity Behind Plates Accelerated from Rest in Still Air," J. Fluid Mech., Vol. 11, p. 460, 1961
- Popov, S. G., "Dependence Between the Strouhal and Reynolds Numbers in Two-Dimensional Flow Past a Circular Cylinder," NASA TT F-11, p. 763, 1968
- Prendergast, V., "Measurements of Two-Point Correlations of the Surface Pressure on a Circular Cylinder," UTIA Technical Note No. 23, 1958
- Protos, A., V. W. Goldschmidt, G. H. Toebes, "Hydroelastic Forces on Bluff Cylinders," Proc. ASME Symposium on Unsteady Flow, Paper No. 68-FE-12, 1968
- Pruppacher, H. R., B. P. LeClair, and A. E. Hamielec, "Some Relations Between Drag and Flow Pattern of Viscous Flow Past a Sphere and a Cylinder at Low and Intermediate Reynolds Numbers," J. Fluid Mechanics, Vol. 44, p. 781, 1970
- Purdy, D. M., F. J. Maher, and F. Frederick, "Model Studies of Wind Loads on Flat-Top Cylinders," ASCE, Vol. 93, No. STE, p. 5209, 1967

- Relf, E. F. and L. F. G. Simmons, "On the Frequency of Eddies Generated by the Motion of Circular Cylinder Through a Fluid," Phil. Mag., (6), 49, p. 509, 1924
- Richardson, E. G., "Aeolian Tones," Proc. Phys. Soc. Lond. 36, p. 153, 1923
- Rosenhead, L., "The Formation of Vortices from a Surface of Discontinuity," Proc. Roy. Soc., A134, p. 170, 1931
- Roshko, A., "Experiments on a Flow Past a Circular Cylinder at Very High Reynolds Number," J. Fluid Mech., Vol. 10, p. 345, 1961
- Roshko, A., "On the Drag and Shedding Frequency of Two-Dimensional Bluff Bodies," NACA TN 3169, 1954
- Roshko, A., "On the Development of Turbulent Wakes from Vortex Streets," NACA TN 1191, 1954
- Roy, D., "Resistance on a Circular Cylinder Due to a Pair of Vortices Moving Symmetrically," ZAMP, Vol. 10, p. 90, 1959
- Roy, D., "Resistance on a Circular Cylinder Due to Any Number of Vortices Lying in Two Rows," ZAMP, Vol. 10, p. 502, 1959
- Sarpkaya, T., "Lift, Drag, and Added-Mass Coefficients for a Circular Cylinder Immersed in a Time-Dependent Flow," J. Appl. Mech., p. 13, 1963
- Sarpkaya, T and C. J. Garrison, "Vortex Formation and Resistance in Unsteady Flow," J. Appl. Mech., p. 16, 1963
- Sarpkaya, T., "Unsteady Flow Over Bluff Bodies," Developments in Mechanics, Proc. 8th Midwestern Mechs. Conf., Pergamon Press, p. 45, 1965
- Sarpkaya, T., "Separated Flow about Lifting Bodies and Impulsive Flow about Cylinders," J. AIAA, Vol. 4, p. 414, 1966
- Sarpkaya, T., "Impulsive and Accelerated Flow about Cylinders," Meeting on Ground Wind Load Problems in Relation to Launch Vehicles, Compilation of Papers Presented at NASA Langley Research Center, CR 76726, June 7-8, 1966

- Sarpkaya, T., "An Analytical Study of Separated Flow about Circular Cylinders," Proc. ASME Symposium on Unsteady Flow, Paper No. 68-FE-15, 1968
- Schaefer, J. W. and S. Eshinazi, "An Analysis of the Vortex Street Generated in a Viscous Fluid," J. Fluid Mech., Vol. 6, p. 241, 1959
- Schwabe, M., "Über druckermittlung in der nichtstationären ebenen Stromung," Ingr-Arch., Bd. Vi. p. 34, 1935
- Son, J. S. and T. J. Hanratty, "Numerical Solution for the Flow Around a Cylinder at Reynolds Numbers of 40, 200, and 500," J. Fluid Mechanics, Vol. 35, p. 369, 1969
- Stelson, T. E. and Mavis, "Virtual Mass and Acceleration in Fluids," ASCE, Trans. Paper No. 2870, p. 518, 1955
- Taneda, S., "Experimental Investigations of Vortex Streets," J. Phys. Soc. Jap., Vol. 20, 1714, 1965
- Tatsuno, M. and S. Taneda, "Visualization of the Unsteady Flow Past Cylinders and Plates Decelerated from a Steady Speed," J. Phys. Soc. Jap., Vol. 31, p. 1266, 1971
- Thom, A., "The Flow Past Circular Cylinders at Low Speeds," Proc. Roy. Soc., A141, p. 651, 1933
- Thom, A., "Experiments on Cylinders Oscillating in a Stream of Water," Phil. Mag. (7), 12, p. 490, 1931
- Tritton, D. J., "Experiments on the Flow Past a Circular Cylinder at Low Reynolds Number," J. Fluid Mech., (6), p. 547, 1959
- Tritton, D. J., "A Note on Vortex Streets Behind Circular Cylinders at Low Reynolds Numbers," J. Fluid Mech., Vol. 45, p. 203, 1971
- Tyler, E., "A Hot-Wire Amplifier Method for the Measurement of the Distribution of Vortices Behind Obstacles," Phil. Mag., Vol. 9, p. 1113, 1930
- Tyler, E., "Vortex Formation Behind Obstacles of Various Sections," Proc. Roy. Soc., A141, p. 651, 1933

- Varga, J. and Gy. Sebestyen, "Determination of the Frequencies of Wakes Shedding From Circular Cylinders," Acta Technica Academiae Scientiarum Hungaricae 53, p. 91, 1966
- Vickery, B. J., "Fluctuating Lift and Drag on a Long Cylinder of Square Cross Section in a Smooth and in a Turbulent Stream," J. Fluid Mech., Vol. 25, p. 481, 1966
- von Karman, Th., "Über den Mechanismus des Widerstandes, den ein bewegter Körper in einer Flüssigkeit erfährt," Nachr. Kgl. Gesell. Wiss. z. Göttingen, p. 509, 1911, and p. 547, 1912
- von Karman, T. and H. Rubach, "Über den Mechanismus des Flüssigkeits- und Luftwiderstandes," Phys. Zs., Bd. ____, Heft 2, January 1912
- Wang, C. Y., "On High-Frequency Oscillatory Viscous Flows," J. Fluid Mechanics, Vol. 32, p. 55, 1968
- Wang, C. Y., "A Note on the Drag of an Impulsively Started Circular Cylinder," J. Math. and Phys., Vol. 47, p. 451, 1968
- Ward, E. G. and C. Dalton, "Strictly Sinusoidal Flow around a Stationary Cylinder," J. Basic Engr., Trans. ASME Series E, Vol. 91, p. 707, 1969
- Weaver, W., "Wind-Induced Vibrations in Antenna Members," Proc. ASCE, Vol. 87, No. EM1, p. 141, 1961
- Willmarth, W. W., N. E. Hawk, and R. L. Harry, "Steady and Unsteady Motions and Wakes of Freely Falling Disks," Phys. of Fluids, Vol. 7, p. 197, 1964
- Willmarth, W. W., N. E. Hawk, A. J. Calloway, and F. W. Ross, "Aero-Dynamics of Oscillating Disks and Right-Circular Cylinder," J. Fluid Mech., Vol. 27, p. 177, 1967
- Zdraukowich, M. M., "Smoke Observations of the Wake of a Group of Three Cylinders at a Low Reynolds Number," J. Fluid Mechanics, Vol. 32, p. 339, 1968